Author: Stegehuis, P.L.
Title: The use of optical techniques to guide cancer diagnosis and radical surgical resections
Issue Date: 2021-04-20

The use of optical techniques to guide cancer diagnosis and radical surgical resections

Paulien Loes Stegehuis

Layout and printed by: Optima Grafische Communicatie (www.ogc.nl)
ISBN: 978-94-6361-536-5

The use of optical techniques to guide cancer diagnosis and radical surgical resections

Proefschrift
ter verkrijging van
de graad van doctor aan de Universiteit Leiden,
op gezag van rector magnificus prof.dr.ir. H. Bijl,
volgens besluit van het college voor promoties
te verdedigen op dinsdag 20 april 2021
klokke 11:15 uur

door
Paulien Loes Stegehuis
geboren te Best
in 1987

Promotor:	Prof. dr. B.P.F. Lelieveldt
Co-promotoren:	Dr. J. Dijkstra en Dr. A.L. Vahrmeijer

Leden promotiecommissie:
Prof. Dr. B.H.W. Hendriks (Technische Universiteit Delft)
Prof. Dr. A.G.J.M. van Leeuwen (Universiteit van Amsterdam)
Prof. Dr. J.V.M.G. Bovee

CONTENTS

1

Introduction and thesis outline

Imaging plays a crucial role in cancer care; it is used to diagnose, to guide biopsies, to monitor treatment response, to plan surgical interventions, and to predict the course of the disease[1, 2]. Computed tomography, magnetic resonance imaging, X-ray, and ultrasound, are routinely used imaging modalities that mainly provide anatomical information [1]. The more recently introduced positron emission tomography and single positron emission computed tomography provide functional information [3]. Advances in all these techniques have led to more precise, faster, and less-invasive imaging [4, 5]. However, all of these image modalities come with their own limitations with respect to resolution, sensitivity, and contrast generation [3], rendering them unsuitable for certain applications [6]. Moreover, apart from X-ray and ultrasound, these techniques are costly and real-time imaging is challenging. A new range of medical imaging technologies is being developed and used to fill this gap: optical imaging techniques [2].

Optical imaging encompasses a variety of techniques that use light in the ultraviolet range (315-400 nm), the visible range (400-700 nm), the near infrared (NIR) range (700-1400 nm) and light in the short wave infrared (SWIR) range (1400-3000 nm) [7] to provide molecular, morphological, and functional information of cells or tissues. These techniques include endoscopy, NIR fluorescence imaging, optical coherence tomography (OCT), photo-acoustic imaging, confocal laser endomicroscopy, diffuse spectroscopy, and Raman spectroscopy. Although the advantages of optical techniques depend heavily on the used technique and field of application, some general advantages are: good contrast in soft tissue, high resolution (from 15 mm for photo-acoustic imaging up to the submicron range for Raman spectroscopy [8]), non-ionizing nature, cheap and relatively easy to handle equipment [3, 9, 10]. The biggest disadvantages are the limited penetration depth (ranging from several hundreds of micrometers for Raman spectroscopy to several centimeters for photo-acoustic imaging [8]) and limited field of view (from point measurements for Raman spectroscopy up to 250 mm for fluorescence guided surgery [8]).

The type of contrast that is generated by optical imaging depends on the type of interactions between light and tissue that are recorded. Light that interacts with tissue undergoes different processes: reflection, absorption, and scattering [11]. All these forms of light-tissue interaction are studied in this thesis, using different techniques: OCT, reflectance spectroscopy and fluorescence lifetime imaging. This introduction provides a short overview of these three techniques and the potential clinical applications that were studied in this thesis.

TECHNIQUES

Full field optical coherence tomography

Optical coherence tomography can be seen as the optical analog of ultrasound, but rather than back-scattered sound, it detects back-reflected light [12]. The resolution in comparison to ultrasound is 10-50 times better, and usually lies in the range of 1-20 µm in axial and transverse direction [13, 14]. Like ultrasound, OCT is able to image non-invasively and non-destructively.

Standard elements of an OCT device include a light source, an interferometer, a reference arm and a detector. Light coming from the source is split by the interferometer into 2 paths of light: one path leads to the sample, while the other goes to the reference arm – a mirror. When light from the reference arm and the sample have traveled the same distance, an interference pattern arises. Areas in the sample exhibiting great reflectivity, such as collagen fibrils, will consequently generate greater interference and thereby a larger signal than areas with lower reflectivity, such as adipose tissue. The combined signal is collected by the detector and an image, typically cross-sectional, can be reconstructed.

For time domain OCT (TD-OCT), the reference arm is translated longitudinal in time to determine the depth of the tissue-scattered light. TD-OCT typically uses a broadband light source – as the low coherence length translates to a high axial resolution [15] – in the NIR wavelength range to achieve a larger sensing depth. Frequency domain OCT (FD-OCT) either uses a combination of tunable laser with a photodiode detector or a broadband wavelength with a spectrometer [16]. The acquired signal contains information on the entire depth of one point, and subsequently the depth profile can be constructed by the Fourier transformation. The main advantage of this method is that the reference arm is static instead of moving, which allows for much faster scanning speed [17].

Both FD-OCT and TD-OCT systems are commercially available and are standard-of-care in ophthalmology [18]. Also in interventional cardiology, where OCT has been integrated in catheters, the use of OCT is rapidly growing. With the development of new modalities, like full field OCT (FF-OCT), other fields of interest are being explored, including the field of oncology [14, 19].

In this thesis we looked at FF-OCT: an optical biopsy technique with high resolution, that provides *en face* images. Figure *1* shows the schematic and actual setup of one of the FF-OCT system (LLTech, France) that we used. It is a time domain system that uses a 150-watt white halogen light source with a central wavelength of 700 nm with spectral width of 125 nm. Furthermore, it uses a Linnik-type interferometer that allows for the parallel acquisition of all pixels on a 2D camera [20, 21]. Resolution is 1 µm in 3D. In depth imaging is possible as well, but in scattering tissue this is limited to approximately 500 µm. So far, several studies report the use of FF-OCT, i.e. on ocular, skin and brain tissue [20–22]. These first studies showed that normal structures can be recognized and differences can be seen when comparing normal tissue to tumor tissue. This is largely due to changes in the architecture of the tissue, as the endogenous contrast of cell nuclei is not sufficient to be detected with FF-OCT.

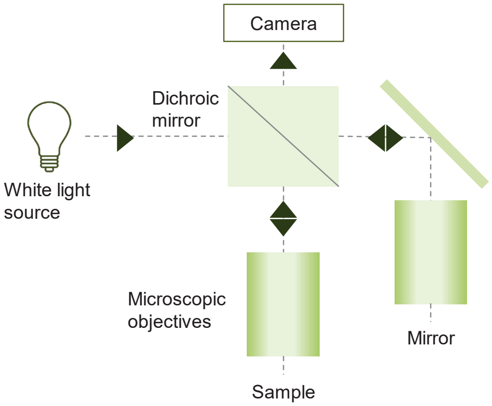

Figure 1. A schematic set-up of the FF-OCT system (based on [23])

Reflectance spectroscopy

Reflectance spectroscopy measures the spectral response of tissue-light interaction. These tissue-light interactions provide information about the tissues' absorption and scattering properties. Absorption of photons can occur without re-emitting another photon and is wavelength dependent. By looking at the light that is re-captured, and thus not absorbed, information on chromophores – the absorbers in the tissue – is acquired. In the visible range, blood (oxygenated and de-oxygenated hemoglobin) is the main absorber in biological tissue. In the NIR range, fat and water are the main absorbers. Light is also absorbed by other chromophores such as bilirubin and beta-carotene, depending on the tissue type. Light is scattered through interactions with the underlying cellular structures, such as cell nuclei. Information on the size and density of these structures provide an insight in the tissues' morphology.

Most commonly, reflectance spectroscopy illuminates the tissue with a broadband white light source through one or multiple optical fibers, and captures the returning light through different or the same fiber(s). A spectrometer collects the returning light and converts it into a spectrum. In literature, several methods are described to analyze the acquired reflectance spectra. One method is to use a physical analysis method: *a priori* knowledge of the tissue components is used to extract and quantify physiological information from the obtained spectra [24–27].

Numerous studies used the absorption and scattering properties of tissue to show differences between normal and tumor tissue, for example in lymph nodes, liver and lung. In general, normal tissue can be differentiated from tumor tissue by higher oxygen saturation, higher blood volume and lower scattering parameters [28–30]. These differences could give physicians feedback on suitable biopsy locations or tumor margins.

In this thesis we looked at single fiber reflectance (SFR) spectroscopy: the same single fiber delivers the outgoing and collects the returning light (Figure *2*). As a consequence, reflectance spectra can be measured through a biopsy needle. Measurement depth is shallow, as it is related to the fiber diameter.

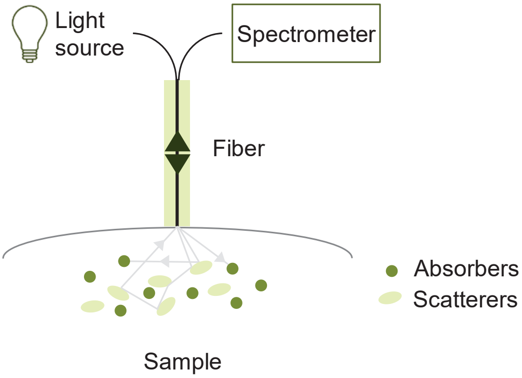

Figure 2. Single fiber reflectance spectroscopy

Fluorescence lifetime measurements

Certain molecules have the ability to absorb light at a particular wavelength and emit light at a longer wavelength; this is called fluorescence. After light absorption, almost all molecules relax to the lowest vibrational state of the first exited state, from which molecules return to their ground energy state. Returning to ground state occurs either via non-radiative decay or radiative decay (non-harmful photons), the latter is responsible for fluorescence. The average time it takes a molecule to radiatively decay after having been excited is the fluorescence lifetime. The lifetime is influenced by intrinsic characteristics of the fluorophore itself, the environment it is in [31] – such as pH, local viscosity, polarity and temperature – and interactions with other fluorophores, while it is largely insensitive to differences in fluorophore concentration and fluorescence intensity [32]. Therefor lifetime provides complementary functional information to fluorescence intensity imaging.

To measure fluorescence lifetime, typically in the order of hundreds of picoseconds to hundreds of nanoseconds, dedicated equipment is necessary. Similar to OCT, fluorescence lifetime can be measured using a time-domain and frequency-domain approach. TD measurements are either performed by time gated image intensifiers or time correlated single photon counting. The principle however is very similar: a short light pulse is emitted to the tissue, for example with a high frequency pulsed laser, and returning photons are detected through a detection module such as photomultiplier tubes or avalanche photodiodes. The arrival times of the photons are determined and a lifetime can be calculated from the slope of the decay curves. FD measurements are related to TD via the Fourier transform. A sinusoid light wave with a certain frequency is emitted. The re-emitted light, detected with photomultiplier tubes or charge-coupled devices, occurs at the same frequency, but with a phase shift and reduction in amplitude. From these parameters, the lifetime can be calculated [31, 32].

Fluorescence lifetime is widely used in preclinical research and clinical applications of fluorescence lifetime are also being explored, for example to investigate the efficacy of targeted therapy [33] or to differentiate between tumor and normal tissue [34].

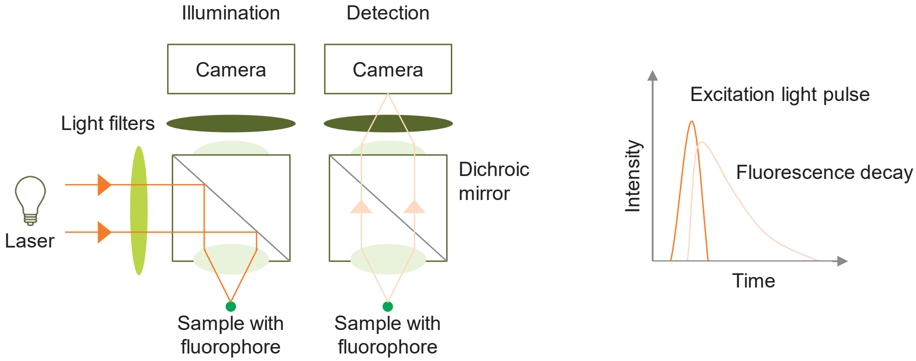

Figure 3. Schematic setup (used in this thesis) to measure fluorescence lifetime

APPLICATIONS

Pancreatic cancer

Pancreatic cancer is the 4th leading cause of cancer death in the Netherlands, while it is ranked 10th in incidence [35]. The 5-year survival rate is only 6%, mainly due to late detection as early-stage pancreatic cancer is usually clinically silent [36, 37]. The only curative treatment for the most prevalent carcinoma type of the pancreas – infiltrating ductal adenocarcinoma (IDAC) – is surgery, but only about 20% of patients are eligible for this treatment [36]. These are patients with a tumor that is not yet metastasized, has no severe vascular infiltration and is thought to be completely resectable [38]. Currently neoadjuvant therapy – chemotherapy or radiation – to downsize the primary tumor and treat micrometastatic disease prior to resection gains more interest [39]. This does however require a biopsy to pathologically confirm the presence of tumor. Subsequently, if the tumor is surgically removed, it is important to remove the entire tumor. In this thesis we looked at two different applications of optical techniques for pancreatic cancer: (1) single fiber reflectance spectroscopy to guide biopsies, and (2) FF-OCT to differentiate tumor from normal pancreatic tissue with an ultimate goal to intraoperatively inspect resection margins.

Patients suspected of a pancreatic lesion, usually are subjected to a CT scan, which is best for disease staging and provides 80% accuracy for prediction of resectability [36]. For cytological diagnosis, endoscopic ultrasound fine needle aspiration (EUS-FNA) is most commonly used: a relatively safe procedure with high specificity. However, its high sampling error results in a low-negative predictive value and requires an on-site cytopathologist [40]. Furthermore, when (peritumoral) pancreatitis is present – which frequently occurs – the accuracy of EUS-FNA drops considerably. In this thesis we looked at the feasibility and added value of SFR spectroscopy to guide the gastroenterologist during the EUS-FNA procedure, with an ultimate goal to improve its accuracy.

Patients who are eligible for surgery, typically undergo a pancreatoduodenectomy (for tumors located in the pancreatic head) or a distal pancreatectomy (for tumors located in the body and tail of the pancreas). One important prognosticator of the 5-year survival rate after surgery are clear (R0) resection margins [41–43]: the resection specimen should be clear from tumor within 1 mm of the margins. However, due to the dispersed growing pattern of IDACs, its anatomical proximity to vital surrounding structures, and the presence of peritumoral inflammation, positive margins frequently occur: up to 60-80% [42–47]. At the moment, during surgery, surgeons mostly have to rely on visual inspection and palpation. In this thesis we imaged normal and pathological pancreatic tissue using FF-OCT, and looked at the accuracy with which the pathologists could distinguish these.

Fertility preservation

Advanced screening methods and novel treatment modalities have led to an improved overall survival for cancer patients, making the long-term adverse effects of treatment more important. Significant consequences of chemo- and pelvic radiotherapy in premenopausal women are decreased fertility or even infertility [48], leading to a lower quality of life [49, 50]. Therefore, fertility preservation is extremely important and has high priority. Current available techniques include embryo and oocyte cryopreservation, ovarian transposition, and ovarian tissue cryopreservation [51]. In ovarian transplantation – only suitable for patients with pelvic malignancies requiring pelvic radiotherapy – the ovaries are moved outside the radiation field [52]. Patients receiving chemotherapy are not benefited by ovarian transposition; for these patients the Dutch guidelines indicate embryo and oocyte cryopreservation as preferred method [53]. Before cancer treatment, patients receive a hormone treatment to stimulate the ovaries and harvest oocytes, which can either be cryopreserved as oocytes, or as embryos. The biggest disadvantage however, is that administration of adjuvant therapy has to be delayed.

Ovarian tissue cryopreservation can be performed immediately, making it the only available method for patients in which the start of adjuvant therapy cannot be delayed [54]. In short, one of the ovaries is laparoscopically removed, the cortex – outer portion of the ovary in which the oocytes reside – is cut into small fragments, which are frozen and stored in liquid nitrogen [55]. The cortex fragments can be thawed and transplanted back to the remaining ovary or a peritoneal window after the completion of cancer treatment. It is still seen as an experimental technique, up to date ovarian tissue transplantation has been performed in 318 women worldwide, and renewed ovarian endocrine function was reported in 95% of them [56]. One major concern however is the safety of the procedure: malignant cells might be present in the transplanted ovarian tissue, possibly reintroducing cancer.

Current techniques used to examine the ovarian cortex fragments such as histology, polymerase chain reaction analysis and xenotransplantation are destructive [51]. This means, only few fragments can be tested for the presence of tumor cells, and those that are tested cannot be transplanted back. In this thesis we looked at the feasibility of FF-OCT – a non-destructive technique – to image ovarian cortex fragments.

Breast cancer

Breast cancer is the most common cancer type in women – with almost 15,000 new cases per year – and the second cause of cancer death in the Netherlands [35]. Around 60 to 75% of patients is treated with breast conserving therapy (BCT): surgically removing the tumor while leaving as much of the breast intact as possible followed by radiotherapy [57, 58]. Multiple studies have demonstrated that BCT is as effective as a mastectomy for the treatment of stages I and II invasive breast cancer when looking at local recurrence and overall survival [57, 59, 60]. However, it is important to remove all tumor tissue, as positive resection margins significantly increase the odds on local recurrence (pooled odds ratio of 2) [61].

A negative margin means that no tumor cells are found at the cut edge of the resected specimen. A positive resection margin, where tumor cells are found at the cut edge, means the patient either has to undergo a re-excision or an adjusted radiation therapy protocol, depending on the extensiveness of tumor on the margin [62]. To remove the whole tumor and achieve negative resection margins, surgeons rely, intraoperatively, mainly on visualization and palpation. Some surgical guidance techniques, such as wire-guided localization, intraoperative ultrasound (US) guidance, radio occult lesion localization, and radiolabeled seed localization have been developed to localize non-palpable lesions [63, 64]. Furthermore, pathological techniques to examine the margins intraoperatively, such as frozen section analysis and imprint cytology are extensively researched for the purpose of reducing the percentage of positive margins. However, all these methods have known drawbacks, such as time-consuming and resource-intensive nature, difficulty in visualizing high-grade carcinomas, and imprecision, due to sampling errors and poor resolution [65–69]: re-excision rates still lie around 20% [58, 61, 70, 71]. These numbers emphasize the necessity for the development of new intraoperative margin assessment tools. In this thesis we looked at the use of FF-OCT to image breast tissue, and its feasibility to help pathologists to distinguish normal from tumor tissue.

OUTLINE OF THIS THESIS

The central objective of this thesis is to study the feasibility of optical imaging techniques to differentiate tumor tissue from surrounding tissue. The main research question of this thesis:

Is it feasible to differentiate tumor tissue from surrounding tissue using optical imaging techniques; and which technique can be of added value for clinicians in which clinical situation?

Chapter 2, 3 and 4 focus on the use of full field optical coherence tomography for fertility preservation and margin detection in breast and pancreatic cancer. The fifth chapter of this thesis focusses on the use of single fiber reflectance spectroscopy to guide EUS-FNA procedures of pancreatic lesions. In the last chapter, fluorescence lifetime measurements are used to distinguish bound from unbound tracer, with the ultimate goal to better detect margins during surgery.. (*Table 1*)

Table 1. Techniques and clinical applications used in this study.

	Full Field OCT	SFR Spectroscopy	Fluorescence lifetime
Margin detection	X		X
Diagnosis		X	
Tissue preservation	X		

REFERENCES

1. Histed SN, Lindenberg ML, Mena E, et al (2012) Review of Functional/ Anatomic Imaging in Oncology. Nucl Med Commun 33:349–361 . doi: 10.1097/MNM.0b013e32834ec8a5
2. Weissleder R, Pittet MJ (2008) Imaging in the era of molecular oncology. Nature 452:580–589 . doi: 10.1038/nature06917
3. Frangioni J V. (2008) New technologies for human cancer imaging. J Clin Oncol 26:4012–21 . doi: 10.1200/JCO.2007.14.3065
4. Laal M (2013) Innovation process in medical imaging. Procedia - Soc Behav Sci
5. Margulis AR, Sunshine JH (2000) Radiology at the turn of the millennium. Radiology. doi: 10.1353/jowh.2008.0015
6. Glunde K, Pathak AP, Bhujwalla ZM (2007) Molecular-functional imaging of cancer: to image and imagine. Trends Mol. Med.
7. Arnaldo D'Amico, Corrado Di Natale, Fabio Lo Castro SI, Martinelli AC and E, Byrnes J (2009) Unexploded Ordnance Detection and Mitigation
8. Stammes MA, Bugby SL, Porta T, et al (2018) Modalities for image- and molecular-guided cancer surgery. Br. J. Surg 2018; 105: e69–e83
9. Taruttis A, Ntziachristos V (2012) Translational optical imaging. Am. J. Roentgenol. 2012;199: 263-271.10.2214/AJR.11.8431
10. Dhawan AP, D'Alessandro B, Fu X (2010) Optical imaging modalities for biomedical applications. IEEE Rev Biomed Eng. doi: 10.1109/RBME.2010.2081975
11. Keereweer S, Van Driel PBAA, Snoeks TJA, et al (2013) Optical image-guided cancer surgery: Challenges and limitations. Clin Cancer Res. doi: 10.1158/1078-0432.CCR-12-3598
12. Huang D, Swanson EA, Lin CP, et al (1991) Optical coherence tomography. Science (80-.).
13. Fujimoto JG (2001) Optical coherence tomography. Comptes Rendus L Acad Des Sci Ser Iv Phys Astrophys. doi: Doi 10.1016/S1296-2147(01)01257-4
14. Vakoc BJ, Fukumura D, Jain RK, Bouma BE (2012) Cancer imaging by optical coherence tomography: Preclinical progress and clinical potential. Nat. Rev. Cancer
15. Marschall S, Sander B, Mogensen M, et al (2011) Optical coherence tomography-current technology and applications in clinical and biomedical research. Anal. Bioanal. Chem.
16. Bouma BE, Yun S-H, Vakoc BJ, et al (2009) Fourier-domain optical coherence tomography: recent advances toward clinical utility. Curr Opin Biotechnol. doi: 10.1016/j.copbio.2009.02.007
17. Adhi M, Duker JS (2013) Optical coherence tomography-current and future applications. Curr. Opin. Ophthalmol. 2013 May ; 24(3): 213–221. doi:10.1097/ICU.0b013e32835f8bf8.
18. Dubois A (2012) Extended full-field optical coherence microscopy. Sel Top Opt Coherence Tomogr. doi: 10.5772/29673
19. Dubois A, Grieve K, Moneron G, et al (2004) Ultrahigh-resolution full-field optical coherence tomography. Appl Opt. doi: 10.1364/AO.43.002874
20. Grieve K, Paques M, Dubois A, et al (2004) Ocular tissue imaging using ultrahigh-resolution, full-field optical coherence tomography. Investig Ophthalmol Vis Sci. doi: 10.1167/iovs.04-0584

21. Binding J, Ben Arous J, Léger J-F, et al (2011) Brain refractive index measured in vivo with high-NA defocus-corrected full-field OCT and consequences for two-photon microscopy. Opt Express. doi: 10.1364/OE.19.004833
22. Dalimier E, Salomon D (2012) Full-field optical coherence tomography: A new technology for 3D high-resolution skin imaging. Dermatology. doi: 10.1159/000337423
23. LLtechimaging (2016) www.lltechimaging.com.
24. Cerussi A, Shah N, Hsiang D, et al (2006) In vivo absorption, scattering, and physiologic properties of 58 malignant breast tumors determined by broadband diffuse optical spectroscopy. J Biomed Opt. doi: 10.1117/1.2337546
25. Ghosh N, Mohanty SK, Majumder SK, Gupta PK (2001) Measurement of optical transport properties of normal and malignant human breast tissue. Appl Opt. doi: 10.1364/AO.40.000176
26. Evers DJ, Nachabe R, Vranken Peeters M-J, et al (2013) Diffuse reflectance spectroscopy: towards clinical application in breast cancer. Breast Cancer Res Treat. doi: 10.1007/s10549-012-2350-8
27. Kanick SC, van der Leest C, Aerts JGJ V., et al (2010) Integration of single-fiber reflectance spectroscopy into ultrasound-guided endoscopic lung cancer staging of mediastinal lymph nodes. J Biomed Opt. doi: 10.1117/1.3290822
28. Kanick SC, van der Leest C, Djamin RS, et al (2010) Characterization of mediastinal lymph node physiology in vivo by optical spectroscopy during endoscopic ultrasound-guided fine needle aspiration. J Thorac Oncol. doi: 10.1097/JTO.0b013e3181ddbc0e
29. Spliethoff JW, Prevoo W, Meier MAJ, et al (2016) Real-time In Vivo Tissue Characterization with Diffuse Reflectance Spectroscopy during Transthoracic Lung Biopsy: A Clinical Feasibility Study. Clin Cancer Res 22:357–365 . doi: 10.1158/1078-0432.CCR-15-0807
30. Tanis E, Evers DJ, Spliethoff JW, et al (2016) In vivo tumor identification of colorectal liver metastases with diffuse reflectance and fluorescence spectroscopy. Lasers Surg Med. doi: 10.1002/lsm.22581
31. Suhling K, Levitt J, Chung P-H (2014) Time-resolved fluorescence anisotropy imaging. Methods Mol Biol. doi: 10.1007/978-1-62703-649-8_22
32. Berezin MY, Achilefu S (2010) Fluorescence Lifetime Measurements and Biological Imaging. Chem Rev 110:2641–2684 . doi: 10.1021/cr900343z
33. Ardeshirpour Y, Chernomordik V, Zielinski R, et al (2012) In Vivo Fluorescence Lifetime Imaging Monitors Binding of Specific Probes to Cancer Biomarkers. PLoS One 7:e31881 . doi: 10.1371/journal.pone.0031881
34. Hatami N (2010) Fluorescence lifetime imaging microscopy for brain tumor image-guided surgery. J Biomed Opt 15:056022 . doi: 10.1117/1.3486612
35. beheerd door IKNL Nederlandse Kankerregistratie
36. Vincent A, Herman J, Schulick R, et al (2011) Pancreatic cancer. In: The Lancet
37. Hidalgo M (2010) Pancreatic cancer. N Engl J Med. doi: 10.1016/j.mpsur.2010.01.005
38. (2011) Richtlijn Pancreascarcinoom - Landelijke werkgroep Gastro-intestinale tumoren
39. Tsai S, Evans DB (2016) Therapeutic advances in localized pancreatic cancer. JAMA Surg.
40. Miura F, Takada T, Amano H, et al (2006) Diagnosis of pancreatic cancer. HPB (Oxford). doi: 10.1080/13651820500540949

41. Verbeke CS, Leitch D, Menon K V., et al (2006) Redefining the R1 resection in pancreatic cancer. Br J Surg. doi: 10.1002/bjs.5397
42. Campbell F, Smith RA, Whelan P, et al (2009) Classification of R1 resections for pancreatic cancer: The prognostic relevance of tumour involvement within 1 mm of a resection margin. Histopathology. doi: 10.1111/j.1365-2559.2009.03376.x
43. Esposito I, Kleeff J, Bergmann F, et al (2008) Most pancreatic cancer resections are R1 resections. Ann Surg Oncol. doi: 10.1245/s10434-008-9839-8
44. Delpero JR, Bachellier P, Regenet N, et al (2014) Pancreaticoduodenectomy for pancreatic ductal adenocarcinoma: A French multicentre prospective evaluation of resection margins in 150 evaluable specimens. HPB. doi: 10.1111/hpb.12061
45. Neoptolemos JP, Palmer DH, Ghaneh P, et al (2017) Comparison of adjuvant gemcitabine and capecitabine with gemcitabine monotherapy in patients with resected pancreatic cancer (ESPAC-4): a multicentre, open-label, randomised, phase 3 trial. Lancet (London, England). doi: 10.1016/S0140-6736(16)32409-6
46. Jamieson NB, Foulis AK, Oien KA, et al (2010) Positive mobilization margins alone do not influence survival following pancreatico-duodenectomy for pancreatic ductal adenocarcinoma. Ann Surg. doi: 10.1097/SLA.0b013e3181d77369
47. Verbeke CS, Gladhaug IP (2012) Resection margin involvement and tumour origin in pancreatic head cancer. Br. J. Surg.
48. Morgan S, Anderson RA, Gourley C, et al (2012) How do chemotherapeutic agents damage the ovary? Hum. Reprod. Update
49. Loscalzo MJ, Clark KL (2007) The Psychosocial Context of Cancer-Related Infertility. In: Oncofertility
50. Duffy C, Allen S (2009) Medical and Psychosocial Aspects of Fertility After Cancer. Cancer J. doi: 10.1097/PPO.0b013e3181976602
51. De Vos M, Smitz J, Woodruff TK (2014) Fertility preservation in women with cancer. Lancet (London, England). doi: 10.1016/S0140-6736(14)60834-5
52. Gubbala K, Laios A, Gallos I, et al (2014) Outcomes of ovarian transposition in gynaecological cancers; A systematic review and meta-analysis. J Ovarian Res. doi: 10.1186/1757-2215-7-69
53. NVOG (2016) Nederlandse richtlijn fertiliteitsbehoud bij vrouwen met kanker
54. Donnez J, Dolmans MM (2013) Fertility preservation in women. Nat. Rev. Endocrinol.
55. Rosendahl M, Schmidt KT, Ernst E, et al (2011) Cryopreservation of ovarian tissue for a decade in Denmark: A view of the technique. Reprod Biomed Online. doi: 10.1016/j.rbmo.2010.10.015
56. Gellert SE, Pors SE, Kristensen SG, et al (2018) Transplantation of frozen-thawed ovarian tissue: an update on worldwide activity published in peer-reviewed papers and on the Danish cohort. J. Assist. Reprod. Genet.
57. van Maaren MC, de Munck L, de Bock GH, et al (2016) 10 year survival after breast-conserving surgery plus radiotherapy compared with mastectomy in early breast cancer in the Netherlands: a population-based study. Lancet Oncol. doi: 10.1016/S1470-2045(16)30067-5
58. McCahill LE (2012) Variability in Reexcision Following Breast Conservation Surgery. JAMA J Am Med Assoc. doi: 10.1001/jama.2012.43

59. Darby S, McGale P, Correa C, et al (2011) Effect of radiotherapy after breast-conserving surgery on 10-year recurrence and 15-year breast cancer death: Meta-analysis of individual patient data for 10 801 women in 17 randomised trials. Lancet. doi: 10.1016/S0140-6736(11)61629-2
60. Fisher B, Anderson S, Bryant J, et al (2002) Twenty-Year Follow-up of a Randomized Trial Comparing Total Mastectomy, Lumpectomy, and Lumpectomy plus Irradiation for the Treatment of Invasive Breast Cancer. N Engl J Med. doi: 10.1056/NEJMoa022152
61. Houssami N, Macaskill P, Luke Marinovich M, Morrow M (2014) The association of surgical margins and local recurrence in women with early-stage invasive breast cancer treated with breast-conserving therapy: A meta-analysis. Ann Surg Oncol. doi: 10.1245/s10434-014-3480-5
62. (2016) Richtlijn mammacarcinoom - Richtlijnwerkgroep Mammacarcinoom
63. Pleijhuis RG, Graafland M, De Vries J, et al (2009) Obtaining adequate surgical margins in breast-conserving therapy for patients with early-stage breast cancer: Current modalities and future directions. Ann Surg Oncol. doi: 10.1245/s10434-009-0609-z
64. Dua SM, Gray RJ, Keshtgar M (2011) Strategies for localisation of impalpable breast lesions. Breast. doi: 10.1016/j.breast.2011.01.007
65. Kennedy S, Geradts J, Bydlon T, et al (2010) Optical breast cancer margin assessment: An observational study of the effects of tissue heterogeneity on optical contrast. Breast Cancer Res. doi: 10.1186/bcr2770
66. Haka AS, Volynskaya Z, Gardecki JA, et al (2006) In vivo margin assessment during partial mastectomy breast surgery using Raman spectroscopy. Cancer Res. doi: 10.1158/0008-5472.CAN-05-2815
67. Brown JQ, Bydlon TM, Richards LM, et al (2010) Optical assessment of tumor resection margins in the breast. IEEE J Sel Top Quantum Electron. doi: 10.1109/JSTQE.2009.2033257
68. Lue N, Kang JW, Yu CC, et al (2012) Portable optical fiber probe-based spectroscopic scanner for rapid cancer diagnosis: A new tool for intraoperative margin assessment. PLoS One. doi: 10.1371/journal.pone.0030887
69. Revesz E, Khan S a (2011) What are safe margins of resection for invasive and in situ breast cancer? Oncol Willist Park NY
70. Jeevan R, Cromwell DA, Trivella M, et al (2012) Reoperation rates after breast conserving surgery for breast cancer among women in England: retrospective study of hospital episode statistics. BMJ. doi: 10.1136/bmj.e4505
71. Hughes L, Hamm J, McGahan C, Baliski C (2016) Surgeon Volume, Patient Age, and Tumor-Related Factors Influence the Need for Re-Excision After Breast-Conserving Surgery. Ann Surg Oncol. doi: 10.1245/s10434-016-5602-8

2

Noninvasive detection of metastases and follicle density in ovarian tissue using full-field optical coherence tomography

Inge T.A. Peters*, Paulien L. Stegehuis*, Ronald Peek, Florine L. Boer, Erik W. van Zwet, Jeroen Eggermont, Johan R. Westphal, Peter J.K. Kuppen, J. Baptist Trimbos, Carina G.J.M. Hilders, Boudewijn P.F. Lelieveldt, Cornelis J.H. van de Velde, Tjalling Bosse, Jouke Dijkstra, Alexander L. Vahrmeijer

* These authors contributed equally to this article

Clin Cancer Research 2016;22(22):5506-5513

ABSTRACT

Purpose

Autotransplantation of ovarian tissue can be used to restore fertility in cancer patients following gonadotoxic treatment. Whether this procedure is safe remains unclear, as current tumor detection methods render the ovarian tissue unsuitable for transplantation. Full-field optical coherence tomography (FF-OCT) is an imaging modality that rapidly produces high-resolution histology-like images without the need to fix, freeze, or stain the tissue. In this proof-of-concept study, we investigated whether FF-OCT can be used to detect metastases in ovarian tissue, thereby increasing the safety of ovarian tissue autotransplantation. We also evaluated whether cortical ovarian tissue and follicles remain viable following FF-OCT imaging.

Experimental design

Formalin-fixed, paraffin-embedded tissue samples were obtained from seven normal ovaries and fourteen ovaries containing metastases and/or micrometastases. These samples were deparaffinized and imaged using FF-OCT. The FF-OCT images were then compared to corresponding hematoxylin-and-eosin-stained tissue sections. Finally, we examined the effect of FF-OCT imaging on the viability of ovarian tissues and follicles in fresh bovine ovarian tissue using a glucose uptake and neutral red staining, respectively.

Results

FF-OCT illustrated both normal structures and metastases in ovarian tissue within minutes. Primordial follicles were readily identifiable. Finally, tissues and follicles remained viable following FF-OCT imaging for up to 180 and 60 minutes, respectively.

Conclusion

FF-OCT imaging is a promising method for the non-invasive detection of metastases, including micrometastases, in ovarian tissue. Moreover, this method facilitates the selection of cortical ovarian tissue with the highest density of primordial follicles, potentially increasing the likelihood of restoring ovarian function following ovarian tissue autotransplantation.

INTRODUCTION

Although advanced screening methods and novel treatment modalities represent a great leap forward in the treatment of cancer leading to substantially increased survival rates, new concerns have arisen as a consequence of these remedies, particularly among young women. Specifically, chemotherapy and/or pelvic radiotherapy can lead to premature ovarian failure due to accelerated follicle loss.[1] Therefore, preserving female reproductive capability is extremely important and has high priority. Currently, the most established fertility preservation procedures include freezing of embryos and/or oocytes. In addition, cryopreservation and subsequent autotransplantation of cortical ovarian tissue has become more prevalent. Because this method obviates the need for hormonal stimulation, it is deemed particularly suitable for prepubescent girls and young women who cannot delay the start of adjuvant therapy.[2] Autotransplantation of frozen-thawed ovarian tissue has been shown to restore ovarian activity in 93% of cases, and to date 60 resulting live births have been reported worldwide.[3-4] Despite these encouraging statistics, the safety of this procedure cannot yet be ascertained for certain types of cancer, as there is a potential risk of occult ovarian involvement at the time of tissue harvesting.[5-6] Due to the fact that the current tumor detection methods (e.g. histology, PCR analysis) render the tissue fragment unsuitable for transplantation, the presence of disseminated tumor cells can only be determined in the ovarian tissues that are ultimately not transplanted. Consequently, tumor cells that have metastasized to the actual ovarian autografts can be reimplanted, thereby potentially re-establishing cancer in the recipient. Previous reports have documented recurrences following autotransplantation in a patient diagnosed with breast cancer [7] and a patient diagnosed with cervical cancer.[8] However, whether these recurrences can be directly attributed to autotransplantation remains unclear. On the other hand, it is entirely plausible that malignant cells were reintroduced by autotransplantation in a patient with a granulosa cell tumor.[9]

To minimize the likelihood of reintroducing tumor cells, a technique that is capable of discriminating malignant from healthy tissues while leaving the examined tissues unaffected is needed. Full-field optical coherence tomography (FF-OCT) is a promising new imaging modality that satisfies these key criteria. Importantly, FF-OCT rapidly generates high-resolution histologylike images without the need to fix, freeze, or stain the tissue.[10] With FF-OCT, the image contrast is based on the light-scattering properties of different structures in the tissue. FF-OCT has already been used successfully to detect tumors in a wide variety of human tissues, including prostate,[11]skin,[12] brain,[13] lung,[14] and kidney[15] samples.

In this proof-of-concept study, we investigated whether FF-OCT can be used to visualize normal structures as well as metastases—including micrometastases—in human ovarian tissue. In addition, we evaluated whether cortical ovarian tissue and preantral follicles remain viable following FF-OCT imaging.

MATERIALS AND METHODS

Human ovarian tissue specimens

Formalin-fixed, paraffin-embedded (FFPE) specimens of normal ovaries obtained from premenopausal women who underwent prophylactic bilateral oophorectomy because of the presence of a *BRCA* gene mutation in the period 2001-2012 were selected from the archives of the Department of Pathology at the Leiden University Medical Center (LUMC). Patients who were previously treated with chemotherapy or used oral contraceptives prior to oophorectomy were excluded in order to ensure that only functionally active ovaries were included in the study. In addition, via a nationwide search performed by PALGA, the Dutch histopathology and cytopathology network and archive that covers all pathology laboratories within the Netherlands,[16] FFPE specimens of ovarian metastases were collected from women with primary invasive breast cancer at age < 41 years in the period 2000-2010. Ovarian metastases derived from other primary malignancies in which ovarian tissue cryopreservation is performed were collected from the archives of the Department of Pathology at the LUMC. Hematoxylin-and-eosin (H&E) stained tissue sections were obtained and digitized using an IntelliSite Pathology Ultra-Fast scanner 1.6 RA (Philips, Eindhoven, the Netherlands). Following this, the entire FFPE tissue blocks were deparaffinized and imaged using FF-OCT.

All patient samples and clinical data were handled in accordance with the medical ethics guidelines described in the Code of Conduct for the Proper Secondary Use of Human Tissue of the Dutch Federation of Biomedical Scientific Societies (FMWV).[17]

Bovine ovarian tissue specimens

Intact bovine ovaries were collected at an abattoir within 15 minutes after slaughtering and immediately transported on ice to the laboratory at the LUMC. The average transport time was 20 minutes. At the laboratory, each ovary was cut into two halves, and the medulla was removed. The remaining cortex was trimmed to a thickness of 1-2 mm and subsequently cut into fragments measuring 2-3 mm or 5-10 mm in diameter for a glucose uptake assay or a neutral red staining, respectively. Bovine cortical ovarian fragments were stored until imaging (ranging from 0 to 180 minutes) in 24-wells plates at 4°C. Each well contained 1.5 ml DMEM culture medium (Lonza BioPharma; Visp, Switzerland) supplemented with 10% FCS (Gibco, ThermoFisher; Waltham, MA) and 1% penicillin/streptomycin (MP Biomedicals; Santa Ana, CA).

Full-field optical coherence tomography

A commercially available LightCT FF-OCT system (LLTech; Paris, France) was initially used in thisstudy.[18] During the course of the study, the LightCT scanner was upgraded to a newly developed FF-OCT system (LLTech), which is faster and can accommodate larger tissue samples. Both systems consisted of an upright microscope with a 10x objective with a central wavelength of 700 nm with spectral width of 125 nm, and reference arm in the Linnik interferometric configuration.[19-20] The light reflected by the tissue interferes with the light reflected by the reference mirror, and the signal is then isolated from the scattered background light using a combination of four phase shifted interferometric images. The LightCT scanner, which was used for the viability experiments, uses a 150-Watt white halogen lamp as the light source and generates a 0.8 mm x 0.8 mm *en face* image (with a maximum field of view 25 mm in diameter using image mosaicking) at an image rate of 35 Hz. The newly developed FF-OCT system, which was used to image the human ovarian tissues, uses an LED lamp as the light source and generates a 1.3 mm x 1.3 mm *en face* image (with a maximum field of view 45 mm in diameter) at an image rate of 75 Hz.

Image acquisition was similar for the two systems. In brief, the tissue was placed in the sample holder. Deparaffinized ovarian tissue was covered with saline, whereas fresh ovarian tissue was covered with DMEM culture medium (Lonza BioPharma) supplemented with 10% FCS (Gibco, Thermo-Fisher) and 1% penicillin/streptomycin (MP Biomedicals). An optical window was positioned above the tissue, and the tissue was gently flattened against this window. A layer of silicone oil was then applied between the optical window and the microscope objective. A macroscopic image was obtained using a wide-field camera, followed by FF-OCT images, which were made *en face*. The field of view encompassed the entire cortical ovarian fragment. With respect to human ovarian tissues, images were taken at a depth of 0-20 µm to ensure the best possible correspondence with the histology images. Considering the bovine cortical ovarian fragments, images were taken up to a depth of 100 µm, as it was the maximum depth at which high resolution could be retained. The number of images taken in depth depended on the time that was needed to achieve the predefined imaging time for the viability tests (ranging from 0 to 180 minutes). Both systems had 1.5 µm transverse resolution and 1 µm axial resolution.

Determining the viability of ovarian tissue using the glucose uptake assay

Bovine cortical ovarian tissue fragments measuring 2-3 mm in diameter were imaged using the LightCT scanner for 3, 10, 60, or 180 minutes. Fresh cortical ovarian samples that were not imaged served as a control, whereas cortical ovarian tissue samples in which cell death was induced by snap-freezing in liquid nitrogen served as a negative control. After imaging, the ovarian samples were transferred to 24-well plates for culturing. Each well was prepared in triplicate and contained three cortical ovarian samples in 1.5 ml DMEM culture medium (Lonza) supplemented with 10% FCS (Gibco, Thermo-Fisher) and 1% penicillin/streptomycin (MP Biomedicals). During culture, the medium was checked periodically for the presence of bacteria under a light microscope. The glucose content of the culture medium was measured using a blood-gas analyzer (Modular P Chemistry Analyzer; Roche Diagnostics, Indianapolis, IN). After four days in culture, the samples were weighed, and glucose consumption was measured and expressed per milligram of ovarian tissue per day, as previously described.[21-22]

Determining the viability of ovarian follicles using neutral red staining

The viability of preantral ovarian follicles was determined using a neutral red staining assay adapted from the protocol published by Kristensen et al.[23] Fresh bovine cortical ovarian fragments were imaged in triplicate using the LightCT scanner for 3, 10, 60, or 180 minutes. These ovarian fragments were 5-10 mm in diameter and 1-2 mm thick. Fresh cortical ovarian fragments that were not imaged served as a control, and cortical ovarian tissue fragments in which cell death was induced by snap-freezing in liquid nitrogen served as a negative control. After imaging, the ovarian fragments were cut into small pieces. These pieces were placed in 15-ml conical tubes containing 5 ml preheated Serum-free Ultraculture medium (Lonza) supplemented with 1 mg/ml collagenase type IA (Sigma-Aldrich, St. Louis, MO). During incubation, the cell suspensions were triturated through a 5-ml pipette to further disrupt the tissue. After incubation for 25 minutes at 37°C, the samples were centrifuged at 2500 rpm for 5 minutes. The supernatants were poured off, and each pellet of cells was incubated for 1.5 hours at 37°C in 4.8 ml McCoy’s medium (Life Technologies, Carlsbad, CA) supplemented with 2 µl Albuman (200 g/L; Sanquin, Amsterdam, the Netherlands), 50 µl Insulin-Transferrin-Selenium (ITS-G; Life Technologies), 50 µl penicillin/streptomycin (MP Biomedicals), and 75 µl neutral red solution (3.3 g/L; Sigma-Aldrich). The number of red-colored (viable) and uncolored (non-viable) follicles in the partially dissolved ovarian tissue fragments were counted in ten high-power fields per specimen under a light microscope by two independent observers (I.P. and P.S.) who were blinded with respect to the samples.

Statistical analysis

Statistical analysis was performed using SPSS version 23.0 (IBM, Armonk, NY). Inter-observer agreement was calculated using the Pearson correlation coefficient. A multivariate linear regression model was used to compute the mean difference in the glucose uptake of cortical ovarian biopsies between the various FF-OCT exposure times. The values were adjusted for the number of ovaries included. To investigate the effect of FF-OCT imaging on the viability of preantral follicles, we compared the proportions of viable preantral follicles between the various FF-OCT exposure times.

RESULTS

Human ovarian tissue specimens

FFPE tissue samples from seven normal ovaries (obtained from six premenopausal patients) and fourteen ovaries containing metastases and/or micrometastases (obtained from twelve patients) were deparaffinized and imaged using FF-OCT. In most cases, the FF-OCT images could be easily interpreted using the inverse setting. In this inverse setting, structures that reflect light the strongest appear black, whereas structures that reflect light poorly appear white.

Figure 1 shows representative FF-OCT images and corresponding histology images of the most clinically relevant structures in a normal ovary. The primordial follicles, which are small primary oocytes surrounded by a single layer of flattened granulosa cells,[24] appear as either round or crescent-shaped white structures, depending on the level at which they were imaged (Figure 1A-B). In primary follicles, the flat granulosa cells transform into a cuboidal structure and the zona pellucida forms between this layer and the oocyte. On the FF-OCT image, the oocyte appears somewhat darker than the zona pellucida, and the granulosa cells can be distinguished quite well (Figure 1C-D). Figure 1E-F shows a corpus rubrum, which is a small hemorrhage that forms immediately after ovulation. The corpus luteum is composed of an outer layer of smaller thecallutein cells and an inner layer of larger granulosal-lutein cells. On the FF-OCT images, the densely packed thecal-lutein cells reflected more light than the granulosal-lutein cells, which reflected light to the same extent as the corpus rubrum (Figure 1G-H). The corpus albicans (Figure 1I-J) and corpus fibrosum (Figure 1K-L), which are masses of fibrous scar tissues that form when the oocyte is not fertilized, showed high levels of reflection due to their collagen content. Lastly, an inclusion cyst (Figure 1M-N) was identified by its thin dark outer layer and lack of interior structure.

Figure 2A shows representative FF-OCT images of a sagittal section of an ovary containing micrometastases; this sample was derived from a primary invasive ductal breast carcinoma. Figure 2B-C and Figure 2D-E show magnified views of micrometastases measuring 0.9 mm and 1.7 mm, respectively. These metastatic lesions could be distinguished clearly from the surrounding stromal cells, as the stromal cells reflected considerably more light than the lesions. On the FF-OCT images, these lesions have a ‘web-like’ architecture in which the tumor cells appear light gray. Furthermore, a distorted ovarian cortex architecture (Figure 2D) was often seen in the presence of disseminated tumor cells. Figure 3 shows metastatic lesions within ovarian tissues obtained from three individual patients. Figure 3A-B depicts a solitary metastasis that originated from an invasive ductal breast carcinoma; the FF-OCT image shows the microglandular proliferation. In Figure 3CD, the ovarian stroma is completely occupied by the metastatic lesion, which has a characteristic stromal component. The FF-OCT image of a metastasis originating from a primary endometrial carcinoma shows a typical cribriform morphology (Figure 3E), with good correspondence with the previously obtained H&E tissue section (Figure 3F). The morphological features of the remaining ten ovaries containing metastatic disease corresponded to those depicted in Figures 2 and 3. All types of normal ovarian features and metastatic lesions that were identified in the histology (H&E) sections were also detected by FF-OCT.

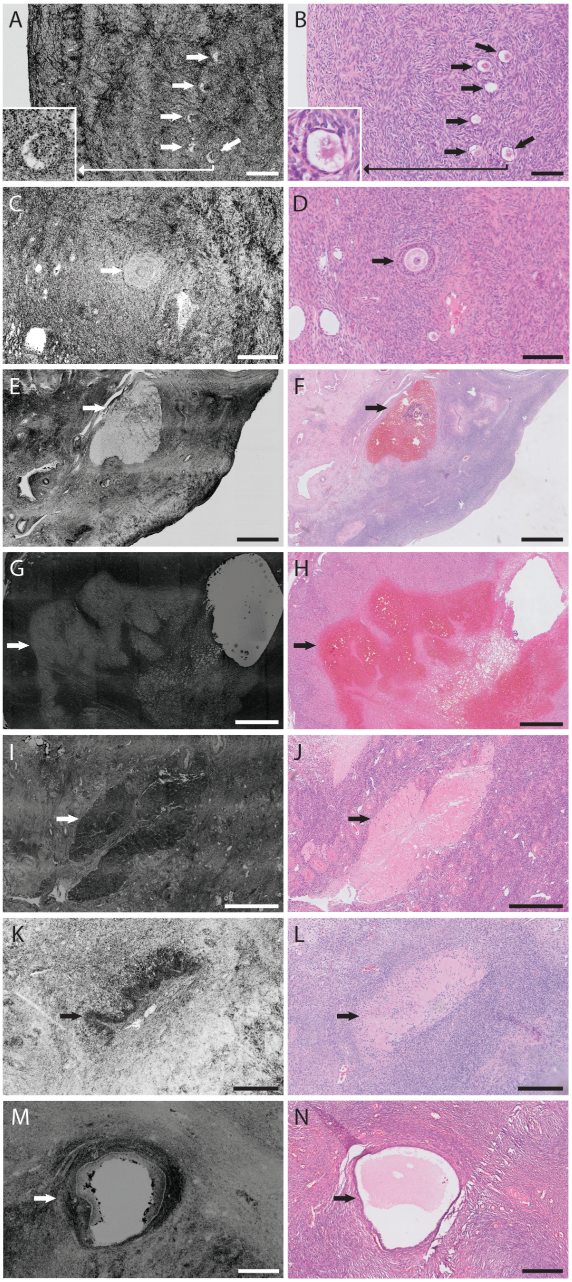

Figure 1. Example inverse FF-OCT images (left column) and corresponding histology images (right column) of normal ovarian tissues. The following normal ovarian structures are shown in the images: primordial follicles (A–B), a primary follicle (C–D), a corpus rubrum (E–F), part of a corpus luteum (G–H), a corpus albicans (I–J), a corpus fibrosum (K–L), and an inclusion cyst (M–N). In each image, the normal ovarian structures are indicated by an arrow. All but one primordial follicle were detected in the FF-OCT image (A) as compared with the corresponding histology image (B). This is due to a slightly different imaging depth. Scale bars, 100 mm (A and B), 150 mm (C and D), 250 mm (K–N), and 1 mm (E–J). Insets show a characteristic primordial follicle (A–B) at three times higher magnification.

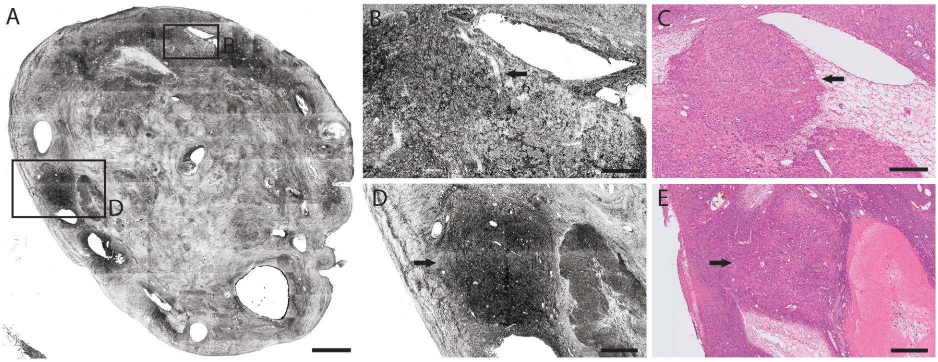

Figure 2. Example inverse FF-OCT images and corresponding histology images of ovarian metastases originating from a primary invasive ductal breast carcinoma. A sagittal view is shown in A, and B to E show magnified views of the micrometastases (indicated by arrows); scale bars, 2 mm (A), 250 mm (B–C), and 500 mm (D–E).

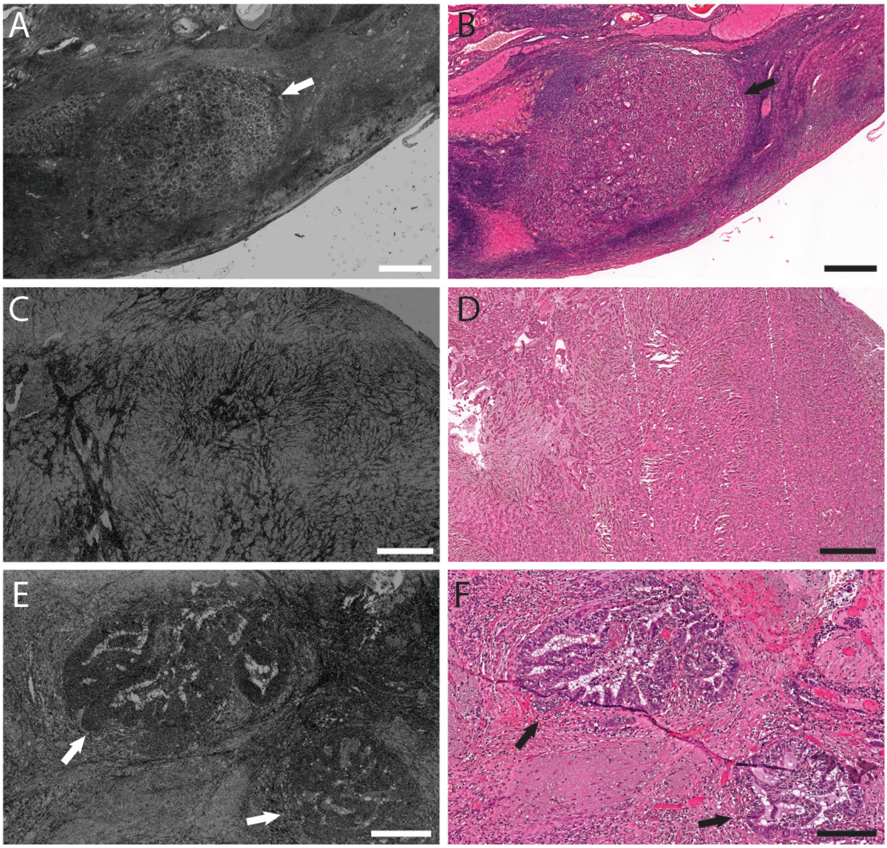

Figure 3. Example inverse FF-OCT images (left column) and corresponding histology images (right column) of ovarian metastases. An ovary containing a solitary metastasis originating from a primary invasive breast carcinoma is shown in A and B (indicated by arrows). An ovary in which disseminated breast tumor cells are dispersed throughout the ovary is shown in C and D. Micrometastases originating from a primary endometrial carcinoma are shown in E and F (indicated by arrows); scale bars, 500 (A–D) and 200 mm (E–F).

Viability of ovarian tissue measured using a glucose uptake assay

Next, we examined whether performing FF-OCT imaging on fresh cortical ovarian tissue affects tissue viability. Table 1 shows the mean glucose consumption per mg ovarian tissue per day over a 4-day culture period of the fresh cortical ovarian tissues that were imaged using FF-OCT for 0, 3, 10, 60, and 180 minutes. All values were adjusted for the number of ovaries used, and none reached statistical significance. Thus, cortical ovarian tissue remained viable — at least with respect to glucose uptake — up to three hours of FF-OCT imaging. No glucose uptake was measured in the cortical ovarian biopsies in which cell death was induced.

Table 1. Viability of cortical ovarian tissue after different FF-OCT exposure times

	Glucose uptake (mmol/mg tissue/d) Mean (95% CI[a])
FF-OCT imaging time	
0 min	50.52 (42.66-58.38)
3 min	46.49 (38.63-54.35)
10 min	44.25 (36.40-52.11)
60 min	40.32 (32.46-48.18)
180 min	46.25 (38.39-54.11)

NOTE: The mean glucose uptake over a 4-day culture period was determined in triplicate, as described in the Materials and Methods section. All values were adjusted for the various ovaries, using a multivariate linear regression model, resulting in a SEM of 4.01.

[a] CI: confidence interval

Viability of preantral ovarian follicles measured using neutral red staining

We also examined the effect of different FF-OCT exposure times on the viability of preantral follicles in fresh cortical ovarian tissue fragments using neutral red staining. The percentage of viable preantral follicles in the samples that were not subjected to FF-OCT imaging was 86% (95% CI 0.81-0.92; Table 2). Although some variation was observed, this viability did not significantly decrease following FF-OCT imaging for up to 60 minutes. Cortical ovarian tissue fragments that were exposed to FF-OCT for 180 minutes had a significantly lower percentage (55%) of viable preantral follicles. As a negative control, no viable preantral follicles were observed in the cortical ovarian tissues in which cell death was induced. Figure 4 shows representative examples of preantral follicles in fresh cortical ovarian tissues that were not exposed to FF-OCT imaging (Figure 4A), preantral follicles that were subjected to FF-OCT imaging for 10 minutes (maximum time required to image a cortical ovarian fragment; Figure 4B) and preantral follicles that were exposed to FF-OCT imaging for 180 minutes (Figure 4C).

Table 2. Viability of preantral follicles after different FF-OCT exposure times

	Total number of follicles observed	Total number of viable follicles	Proportion	95% CI[a]
FF-OCT imaging time				
0 min	145	125	0.86	0.81-0.92
3 min	208	183	0.88	0.84-0.92
10 min	193	189	0.98	0.96-1.00
60 min	195	185	0.95	0.92-0.98
180 min	179	99	0.55	0.48-0.63

NOTE: The proportion of viable preantral follicles was determined by a neutral red staining. Results are based on three different cortical ovarian fragments per condition.

[a] CI: confidence interval

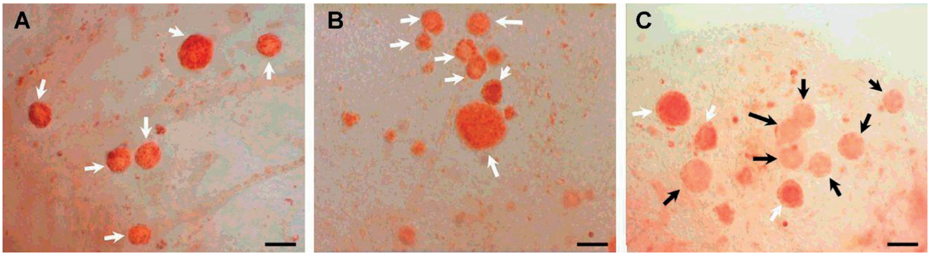

Figure 4. Viability of preantral follicles before and after FF-OCT imaging. Representative images of preantral follicles in fresh cortical ovarian tissues that were not exposed to FF-OCT imaging are shown in A. Preantral follicles in cortical ovarian tissues that were subjected to FF-OCT imaging for 10 minutes are shown in B. Preantral follicles in cortical ovarian tissues that were subjected to FF-OCT imaging for 180 minutes are shown in C. The white and black arrows indicate red-colored (i.e., viable) and uncolored (i.e., non-viable) follicles, respectively; scale bars, 100 mm.

DISCUSSION

In this proof-of-concept study, we investigated whether FF-OCT can be used to detect metastases in ovarian tissue prior to autotransplantation, thereby reducing the risk of reintroducing ovarian tissue that might contain metastases. We found that FF-OCT can be used to visualize both normal structures and metastases — including micrometastases — in ovarian tissues derived from premenopausal women. These findings are particularly relevant from a clinical perspective, given that the pathologist must distinguish between benign and malignant lesions based solely on tomographic images. Routine pathology methods such as histology and immunohistochemistry cannot be used in this context, as these methods render the cortical ovarian tissue unsuitable for autotransplantation. Importantly, our results may serve to help pathologists use FF-OCT as a novel tool for detecting metastases in ovarian tissues.

In our study, we used deparaffinized FFPE tissue samples, as fresh ovarian tissues were not readily available for research purposes and ovarian metastases are relatively rarely encountered. However, we found no difference with respect to visual assessment of normal ovarian structures between the deparaffinized ovarian tissue samples and the fresh ovarian tissues that were used for measuring viability. Our finding is supported by a study of Wilson et al. in which the optical features of various non-paraffinized and deparaffinized tissues were compared and no substantial differences were found.[25]

Because of the relatively few number of ovarian tissue samples that contained micrometastases, we were unable to perform a blinded analysis in which two pathologists independently assessed the FF-OCT images without having access to the original H&E-stained tissue sections. Such an analysis would require a 'training set' in order to familiarize the pathologists with non-neoplastic and neoplastic ovarian tissues on FF-OCT, followed by a 'test set' for which the sensitivity and specificity of FF-OCT imaging could be determined.14-15 Although this type of analysis was beyond the scope of this proof-of-concept study, it should be performed in future studies in order to confirm whether FF-OCT is a suitable diagnostic instrument for use in ovarian tissue.

The maximum depth of FF-OCT imaging that provided high-resolution images in the cortical ovarian strips was approximately 100 µm, which is considerably lower than the imaging depth of up to 500 µm reported for other tissues.10 This difference is due primarily to the large-scale extracellular matrix network in the ovarian cortex,[26-27] which greatly reduces tissue penetration.[28] Nevertheless, imaging depth could be increased somewhat by imaging the cortical ovarian tissue fragments from both sides, thereby effectively doubling the amount of tissue that can be imaged. Moreover, rapid advances in the field of optical imaging will likely enable clinicians to use this non-invasive approach to visualize even deeper structures in the near future.

Interestingly, previous studies that used conventional OCT to examine ovaries achieved an imaging depth of up to 2 mm.[29-30] However, the imaging resolution of conventional OCT is considerably lower than FF-OCT.[31] For our purposes, achieving ultra-high resolution is crucial, as patients with clinically diagnosed early-stage cancer who are eligible for cryopreservation of ovarian tissue can potentially have occult micrometastases in their ovarian tissues.[32-34] Importantly, FF-OCT imaging provides images with a resolution of approximately 1 µm.31 In addition to the detection of occult ovarian involvement, this high-resolution imaging modality provides the opportunity to visually assess the density of primordial follicles in the ovarian autografts, which is highly relevant, given that successfully restoring ovarian activity depends critically on the number of primordial follicles present in the ovarian autograft.3 Thus, FF-OCT provides the added value of selecting the cortical ovarian fragments with the highest potential for restoring fertility.

Because FF-OCT generates images at a rapid rate,15 this technique is particularly suitable to the field of ovarian tissue cryopreservation, where ischemia and oxidative stress during a lengthy avascular period are known to cause loss of primordial follicles.[35] The average time required to image a cortical ovarian fragment measuring 5-10 mm in diameter was seven minutes using the original FF-OCT system, and this time was reduced further to a mere one minute with the newly developed FF-OCT system. During these brief periods, the viability of both the ovarian tissue and the preantral follicles remained high. Even performing FF-OCT imaging for 180 and 60 minutes did not significantly reduce the viability of ovarian tissues and preantral follicles, respectively. These data support the notion that short-term FF-OCT imaging has little effect on either ovarian tissues or preantral follicles. Nevertheless, given that the most meaningful outcome in the field of fertility preservation is ultimately a successful pregnancy, future research will focus on evaluating pregnancy rates following exposure to FF-OCT.

With respect to using FF-OCT as a non-invasive means to detect metastases in the actual ovarian autografts, cortical ovarian strips can be imaged immediately following oophorectomy (see the proposed workflow diagram in Supplementary Figure 1). If the pathologist observes lesions that raise a suspicion of metastases, these fragments could then be analyzed further using histological examination and/or PCR analysis. If these further tests confirm the presence of metastatic tissue in the ovarian fragments, no autotransplantation will be performed. On the other hand, if the histological results are negative (i.e., a false positive result on FF-OCT), the remaining ovarian fragments—particularly those fragments that appeared normal on FF-OCT imaging—can still be transplanted. Moreover, as discussed above, the pathologist can also select the tissue fragments with the highest density of follicles, thereby maximizing the likelihood of restoring the patient’s ovarian function. Importantly, FF-OCT imaging should be performed under sterile conditions in order to prevent bacterial contamination.

In conclusion, FF-OCT imaging is a promising new non-invasive method for rapidly detecting ovarian metastases in ovarian fragments prior to autotransplantation in patients whose ovarian function has been lost. Moreover, this method facilitates the selection of cortical ovarian tissues with the highest density of primordial follicles, significantly increasing the likelihood of restoring ovarian function. Although it is not yet possible to detect all ovarian metastases and/or follicles in the cortical ovarian fragments due to a limited tissue penetration depth, FF-OCT provides a large improvement over the current tumor detection methods as it is the only approach now available by which the actual ovarian autografts, used for transplantation, can be examined.

Acknowledgements

The authors are grateful to the Dutch Pathology Registry (PALGA) and the pathology laboratories for their collaboration. The authors also thank the Clinical Chemistry Laboratory at the Leiden University Medical Center for providing practical help.

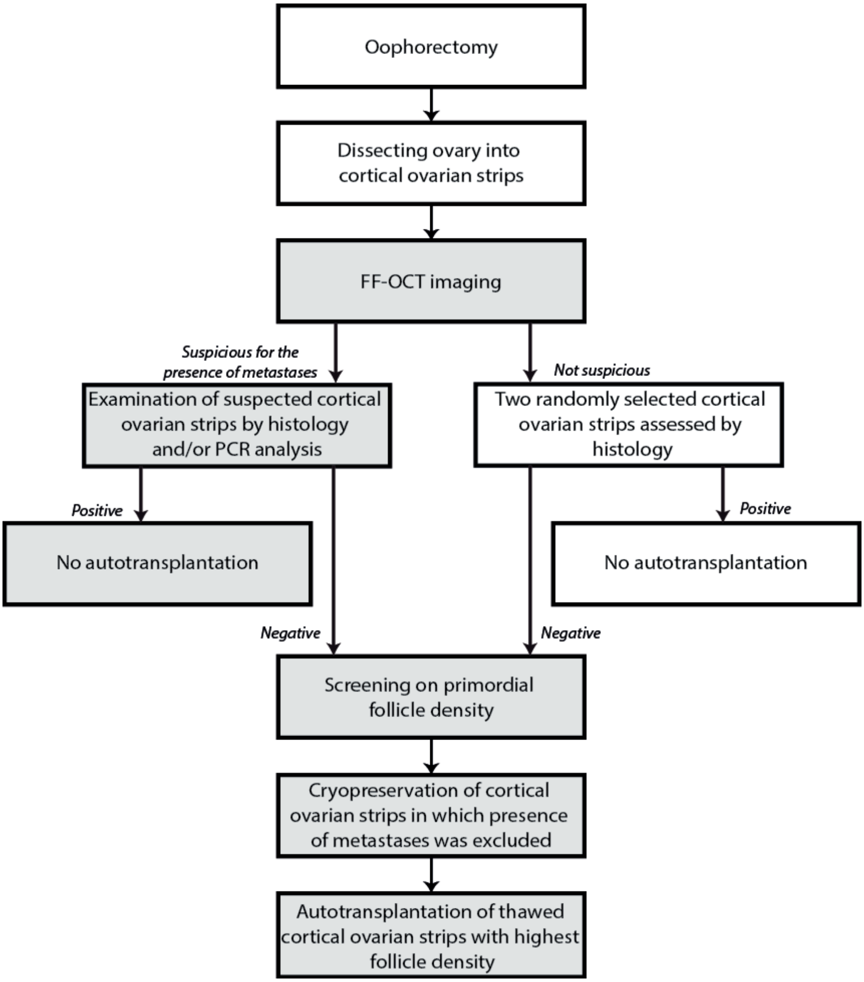

Supplementary figure 1 Proposed clinical workflow for screening cortical ovarian strips prior to autotransplantation in order to minimize the likelihood of reintroducing tumor cells and maximize the likelihood of restoring ovarian function. The light-gray shaded boxes indicate steps in which FF-OCT imaging can provide added value.

REFERENCES

1. Morgan S, Anderson RA, Gourley C, Wallace WH, Spears N. How do chemotherapeutic agents damage the ovary? Hum Reprod Update 2012;18(5):525-535.
2. The Practice Committee of the American Society for Reproductive Medicine. Ovarian tissue cryopreservation: a committee opinion. Fertil Steril 2014;101(5):1237-1243.
3. Donnez J, Dolmans MM, Pellicer A, et al. Restoration of ovarian activity and pregnancy after transplantation of cryopreserved ovarian tissue: a review of 60 cases of reimplantation. Fertil Steril 2013;99(6):1503-1513.
4. Donnez J, Dolmans MM. Ovarian cortex transplantation: 60 reported live births brings the success and worldwide expansion of the technique towards routine clinical practice. J Assist Reprod Genet 2015;32(8):1167-1170.
5. Dolmans MM, Luyckx V, Donnez J, Andersen CY, Greve T. Risk of transferring malignant cells with transplanted frozen-thawed ovarian tissue. Fertil Steril 2013;99(6):1514-1522.
6. Bastings L, Beerendonk CCM, Westphal JR, et al. Autotransplantation of cryopreserved ovarian tissue in cancer survivors and the risk of reintroducing malignancy: a systematic review. Hum Reprod Update 2013;19(5):483-506.
7. Ernst EH, Offersen BV, Andersen CY, Ernst E.Legal termination of a pregnancy resulting from transplanted cryopreserved ovarian tissue due to cancer recurrence. J Assist Reprod Genet 2013;30(7):975-978.
8. Kim SS. Assessment of long term endocrine function after transplantation of frozenthawed human ovarian tissue to the heterotopic site: 10 year longitudinal follow-up study. J Assist Reprod Genet 2012;29(6):489-493.
9. Stern CJ, Gook D, Hale LG, et al. Delivery of twins following heterotopic grafting of frozen-thawed ovarian tissue. Hum Reprod 2014;29(8):1828.
10. Harms F, Dalimier E, Vermeulen P, Fragola A, Boccara AC. Multimodal full-field optical coherence tomography on biological tissue: toward all optical digital pathology. Proc of Spie 2012;8216:821609-1-8.
11. Lopater J, Colin P, Beuvon F, et al. Real-time cancer diagnosis during prostate biopsy: ex vivo evaluation of full-field optical coherence tomography (FFOCT) imaging on biopsy cores. World J Urol 2016;34(2):237-243.
12. Durkin JR, Fine JL, Sam H, Pugliano-Mauro M, Ho J. Imaging of Mohs micrographic surgery sections using full-field optical coherence tomography: a pilot study. Dermatol Surg 2014;40(3):266-274.
13. Assayag O, Antoine M, Sigal-Zafrani B, et al. Large field, high resolution full-field optical coherence tomography: a pre-clinical study of human breast tissue and cancer assessment.Technol Cancer Res Treat 2014;13(5):455-468.
14. Jain M, Narula N, Salamoon B, et al. Fullfield optical coherence tomography for the analysis of fresh unstained human lobectomy specimens. J Pathol Inform 2013;4:26.
15. Jain M, Robinson BD, Salamoon B, Thouvenin O, Boccara C, Mukherjee S. Rapid evaluation of fresh kidney tissue with full-field optical coherence tomography. J Pathol Inform 2015;6:53.

16. Casparie M, Tiebosch AT, Burger G, et al. Pathology databanking and biobanking in The Netherlands, a central role for PALGA, the nationwide histopathology and cytopathology data network and archive. Cell Oncol 2007;29(1):19-24.
17. Federa FMWV. Code for proper secondary use of human tissue in the Netherlands 2002. Available from: http://www.federa.org/codesconduct.
18. LLTechimaging. LightCT FF-OCT system 2016. Available from: http://www.lltechimaging.com/products-applications/products/.
19. Dubois A, Vabre L, Boccara AC, Beaurepaire E. High-resolution full-field optical coherence tomography with a Linnik microscope. Appl Opt 2002;41(4):805-812.
20. Dubois A. Full-field optical coherence microscopy. In: Liu G, editor. Selected topics in optical coherence tomography. Rijeka, Croatia: InTech; 2012; 3-20.
21. Gerritse R, Beerendonk CCM, Westphal JR, Bastings L, Braat DDM, Peek R. Glucose/lactate metabolism of cryopreserved intact bovine ovaries as a novel quantitative marker to assess tissue cryodamage. Reprod Biomed Online 2011;23(6):755-764.
22. Bastings L, Liebenthron J, Westphal JR, et al.Efficacy of ovarian tissue cryopreservation in a major European center. J Assist Reprod Genet 2014;31(8):1003-1012.
23. Kristensen SG, Rasmussen A, Byskov AG, Andersen CY. Isolation of pre-antral follicles from human ovarian medulla tissue. HumReprod 2011;26(1):157-166.
24. Gougeon A, Chainy GB. Morphometric studies of small follicles in ovaries of women at different ages. J Reprod Fertil 1987;81(2):433-442.
25. Wilson JW, Degan S, Warren WS, Fischer MC. Optical clearing of archive-compatible paraffin embedded tissue for multiphoton microscopy.Biomed Opt Express 2012;3(11):2752-2760.
26. Lind AK, Weijdegard B, Dahm-Kahler P, Molne J, Sundfeldt K, Brannstrom M. Collagens in the human ovary and their changes in the perifollicular stroma during ovulation. Acta Obstet Gynecol Scand 2006;85(12):1476-1484.
27. Laronda MM, Jakus AE, Whelan KA, Wertheim JA, Shah RN, Woodruff TK. Initiation of puberty in mice following decellularized ovary transplant. Biomaterials 2015;50:20-29.
28. Trottmann M, Kolle S, Leeb R, et al. Ex vivo investigations on the potential of optical coherence tomography (OCT) as a diagnostic tool for reproductive medicine in a bovine model. J Biophotonics 2016;9(1-2):129-137.
29. Brewer MA, Utzinger U, Barton JK, et al. Imaging of the ovary. Technol Cancer Res Treat 2004;3(6):617-627.
30. Hariri LP, Bonnema GT, Schmidt K, et al. Laparoscopic optical coherence tomography imaging of human ovarian cancer. Gynecol Oncol 2009;114(2):188-194.
31. Dubois A, Moreau J, Boccara C. Spectroscopic ultrahigh-resolution full-field optical coherence microscopy. Opt Express 2008;16(21):17082-17091.
32. Azem F, Hasson J, Ben-Yosef D, et al. Histologic evaluation of fresh human ovarian tissue before cryopreservation. Int J Gynecol Pathol 2010;29(1):19-23.
33. Sanchez-Serrano M, Novella-Maestre E, Rosello-Sastre E, Camarasa N, Teruel J, Pellicer A. Malignant cells are not found in ovarian cortex from breast cancer patients undergoing ovarian cortex cryopreservation. Hum Reprod 2009;24(9):2238-2243.

34. Hoekman EJ, Smit VT, Fleming TP, Louwe LA, Fleuren GJ, Hilders CG. Searching for metastases in ovarian tissue before autotransplantation: a tailor-made approach. Fertil Steril 2014;103(2):469-477.

35. Van Eyck AS, Jordan BF, Gallez B, Heilier JF,Van Langendonckt A, Donnez J. Electron paramagnetic resonance as a tool to evaluate human ovarian tissue reoxygenation after xenografting. Fertil Steril 2009;92(1):374-381.

3

Diagnostic accuracy of full-field optical coherence tomography in patients with *in situ* or invasive breast cancer

Paulien L. Stegehuis, J. Sven D. Mieog, Tjalling Bosse, Arantza FariñaSarasqueta, Jeroen Eggermont, Cornelis J.H. van de Velde, Boudewijn P.F. Lelieveldt , Alexander L. Vahrmeijer, Jouke Dijkstra

Submitted to Clinical Breast Cancer

ABSTRACT

Purpose: Over 20% of women undergoing breast conserving surgery require a re-excision, emphasizing the need for the development of new intraoperative margin assessment tools. Full-field optical coherence tomography (FF-OCT) is a non-invasive, high resolution imaging modality that could potentially help

Methods: 100 images were collected from 44 patients who underwent breast surgery because of cancer. Two pathologists scored independently 77 images after a brief training. Results were compared to those obtained with standard hematoxylin and eosin (H&E) slides.

Results: Overall, pathologist 1 achieved a sensitivity, specificity and accuracy of 63%, 97% and 81% respectively. Pathologist 2 achieved a sensitivity, specificity and accuracy of 86%, 68% and 77% respectively. In 4 cases, both pathologists scored false-positive, the percentage of fat in these cases was significantly higher.

Conclusion: FF-OCT images could be interpreted by pathologists. However, the current accuracy with which this is done, is not yet sufficient to be reliably used in clinical practice. We believe that with several measures – improved training, better contrast and computer aided diagnosis – accuracy can be increased.

INTRODUCTION

Breast cancer is the most commonly diagnosed cancer and leading cause of cancer death in women [1]. The preferred method of treatment for women with early stage breast cancer is breast conserving surgery (BCS) – removing the tumor without removing excess healthy breast tissue – followed by radiotherapy [2]. In BCS, it is pivotal that borders of the excised specimen do not contain any tumor cells, since tumor-positive resection margins are associated with a higher risk of local recurrence [3–6].

To remove all tumor cells and achieve negative resection margins, surgeons rely mainly on visualization and palpation during surgery. Over the years, several surgical guidance techniques were developed to localize non-palpable lesions, such as wire-guided localization, intraoperative ultrasound, radio occult lesion localization, and radiolabeled seed localization. Furthermore, pathological techniques to examine the margins intraoperatively, such as frozen section analysis and imprint cytology are studied for the purpose of reducing the percentage of positive margins in BCS [7]. However, all these methods are limited by their drawbacks, most importantly, time-consuming and resource-intensive nature, difficulty in visualizing high-grade carcinomas, and imprecision, due to sampling errors and poor resolution [7–11]. As a result, over 20% of women undergoing BCS still require a re-excision [12–16], emphasizing the need for the development of new intraoperative margin assessment tools.

Optical imaging has the potential to improve intraoperative margin assessment as the technique enables non-invasive and real-time visualization of molecular and physiological changes associated with cancer. Numerous optical techniques, including diffuse reflectance spectroscopy, intrinsic fluorescence spectroscopy, Raman spectroscopy, fluorescence lifetime imaging, radiofrequency spectroscopy, photoacoustic imaging and optical coherence tomography (OCT) are being investigated for this aim [17–22].

OCT was first described in 1991 and uses low-coherence interferometry to produce two-dimensional cross-sectional images [23]. It has been implemented in ophthalmology and cardiology, and its added value in surgical oncology is being studied [24]. Full-field OCT (FF-OCT) is a modality, based on the principles of white light interference microscopy, and acquires *en face* images by illuminating the whole field of view without scanning [25]. It enables non-invasive, high-resolution imaging of thick fresh tissue without the need for tissue staining, coloring, fixating or slicing, by measuring the backscattered light of tissue structures with different refractive indices.

In a pilot study, Assayag et al. used FF-OCT to image human breast tissue and evaluate whether these images had sufficient detail for a pathologist to make a diagnosis [26]. In that study, images of 78 breast specimens of 21 patients, including both cancer and normal tissue, were assessed by two pathologists, achieving an accuracy of 83%. In this study we tried to replicate those results using the same FF-OCT device within a broader patient cohort and added a second-level interpretation (to differentiate normal, benign, in situ and invasive tissue), to add a more in depth diagnosis.

MATERIAL AND METHODS

Patient and sample selection

Successive patients who underwent surgery for breast cancer at the Leiden University Medical Center were included in this study. From each patient, if achievable, one tissue section with and one tissue section without tumor was obtained. This selection was made based on macroscopic assessment by the pathologist. The fresh tissue sections were not fixated and non frozen. All patient samples and clinical data were handled in accordance with the medical ethic guidelines described in the Code of Conduct for the Proper Secondary Use of Human Tissue of the Dutch Federation of Biomedical Scientific Societies (FMWV) [27].

FF-OCT imaging and sample processing

Images were obtained using a commercially available high resolution FF-OCT system (Light-CT™ scanner, LLTech SAS, Paris, France). The setup consists of an upright microscope with a 10x objective, a halogen light-source with a wavelength of 700±125 nm, and a reference arm in Linnik interferometric configuration [28,29]. The images are acquired at an image rate of 35 Hz, in a *en face* mode. Although the field of view is 0.8 by 0.8 mm, this can be increased by using image mosaicking (with a maximum diameter of 25 mm). Image resolution is 1.5 µm isotropic, and image depth is adjustable, with a maximum depth of several millimeters, depending on tissue properties [30].

The tissue samples were placed in the sample holder, with the surface to be imaged facing upward, and covered in saline. An optical window was positioned on top of the tissue, to which the tissue was gently flattened. A layer of silicone oil was then applied between the optical window and the microscope objective. A macroscopic image was obtained using a wide-field CCD camera, followed by FF-OCT images. FF-OCT images were acquired at a depth of 20 µm, to ensure the best possible correspondence with histology images. Imaging time for one sample (on average 2.5 by 1.5 cm) was on average 30 minutes.

After FF-OCT imaging, tissue samples were formalin fixed and embedded in paraffin. Hematoxylin-and eosin-stained (H&E) slides were obtained and digitalized with a digital pathology slide scanner (IntelliSite Ultra Fast Scanner, Philips, Eindhoven, the Netherlands). FF-OCT images were viewed using in-house developed analysis software based on MeVisLab (MeVis Medical Solutions AG and Fraunhofer MEVIS, Germany).

Assessment FF-OCT images

Two pathologists, one experienced in breast pathology (pathologist 1, TB), and one experienced in gastroenterology and liver pathology (pathologist 2, AF), participated in this study. An image atlas with representative FF-OCT images of normal breast and breast cancer tissues, together with their corresponding H&E images was constructed. Both pathologists followed a brief training, in which the atlas (including 10 images of normal, benign and malignant tissue) was shown, and the technique and method of tissue imaging were explained. The interpretation was performed on 77 images. The images were presented in random order to both pathologists although in the same order. The reading process of the FF-OCT images was standardized. All images were scored in the presence of one assessor (PLS), who completed the pre-designed reading sheet (Appendix 1) on basis of the pathologist's assessment. Pathologists were allowed to digitally zoom the images, to adjust brightness and contrast, and to look at both the original and inverse setting FF-OCT image. In the original setting, hypo-scattering areas (such as adipose tissue) appear black in the image, while hyper-scattering areas (such as collagen) appear white. This is reversed in the inverse setting, making it more similar to H&E images. Clinical data including macroscopic imaging, tumor localization or patient records were not presented to the pathologists during the study.

In a first level interpretation, the pathologists classified the tissue slides as malignant or benign or unclassifiable. In a second level interpretation, the pathologists classified the tissue slides as normal, benign, *in situ* carcinoma or invasive carcinoma. When both *in situ* and invasive carcinoma were present, concordance is only accomplished when the pathologist indicated invasiveness (the more severe diagnosis). Minor discrepancy was defined as *in situ* classification while being invasive carcinoma or the other way around. Major discrepancy was defined as a failed diagnosis or when benign is seen as normal tissue or the other way around.

Statistical analysis

The results of the individual region-of-interest scores were put in a 2x2 *contingency* table to calculate sensitivity, specificity, positive predictive value (PPV), negative predictive value (NPV) and accuracy.

Differences in time to reach a diagnosis were calculated using a t-test assuming unequal variances. Differences in fat percentage (scored by a pathologist based on H&E images) between correctly and incorrectly diagnosed malignant tissues were calculated using an ANOVA table.

RESULTS

Patient and tissue description

A total of 107 tissue samples were collected from surgical specimens from 50 breast cancer patients. Part of those images were used for the training session. These images were not used as test images. In total, 77 images of tissue samples collected from 44 patients were assessed by both pathologists. All patients underwent breast surgery, either lumpectomy or mastectomy. Patient and treatment characteristics are provided in Table 1. In total, 77 images with both histologic and FF-OCT diagnosis were present. On first-level interpretation, 36 were malignant and 41 were benign. On second-level interpretation, 35 were normal breast tissue, 6 were benign breast tissue, either benign lesions (fibroadenoma, myofibroblastoma, location of the tumor-marking clip or the place of a previous biopsy) or inflammation, 6 contained *in situ* carcinoma, 29 contained invasive carcinoma, and 1 contained both *in situ* as invasive carcinoma.

Table 1. Patient and treatment characteristics

Characteristics	N=44
Age (y), mean	55.8 (19-85)
Tumor size (mm), mean	21.8 (3-60)
Histological diagnosis, n (%)	
IC NOS/DCI	*25 (56)*
Grade I	*6 (24)*
Grade II	*6 (24)*
Grade III	*8 (32)*
ILC	*5 (11)*
Grade I	*2 (40)*
Grade II	*2 (40)*
Grade III	*1 (20)*
DCIS	*4 (9)*
FA	*2 (5)*
Other	*8 (18)*
Surgical procedure, n (%)	
Lumpectomy + SN	*16 (36)*
Mastectomy	*3 (7)*
Ablation	*18 (41)*
Needle guided lumpectomy	*4 (9)*
Excision biopsy	*3 (7)*
Neoadjuvant therapy	11 (25)

Diagnostic test characteristics

Pathologist 1 classified 73 out of 77 FF-OCT images (95%), pathologist 2 classified 70 out of 77 FF-OCT images (91%). The pathology assessment of the FF-OCT images in the first-level interpretation is provided in Table 2. Overall accuracy was 81% for pathologist 1, and 77% for pathologist 2. Pathologist 1 achieved a 63% sensitivity and 96% specificity, while pathologist 2 achieved a 86% sensitivity and 68% specificity. Reading time ranged from 0.5 to 11 minutes and was on average 2.7 minutes for pathologist 1. Reading time ranged from 0.5 to 8 minutes and was on average 1.7 minutes for pathologist 2. Both pathologists had a significant higher average reading time when they misdiagnosed; for pathologist 1 this was 4.5 minutes versus 2.3 minutes (p=0.02), for pathologist 2 this was 2.3 minutes versus 1.5 minutes (p=0.02). In the first half of the assessment both pathologists mostly used both the original and the inverted setting of the FF-OCT image to reach a conclusion. In the second half they mostly used the original setting of the FF-OCT images, and they reached a diagnosis faster.

Table 2. Diagnostic test characteristics of FF-OCT on breast cancer specimens per pathologist

	Pathologist 1	**Pathologist 2**
Unclassified	4	7
True positive	22	31
True negative	37	23
False positive	1	11
False negative	13	5
Total	**77**	**77**
Sensitivity	63%	86%
Specificity	97%	68%
Accuracy	81%	77%

Benign FF-OCT images

In 14 out of the 41 benign FF-OCT images either one of the pathologists classified a benign image as a malignant one, none of the images were misclassified by both pathologists. In Figure 1 examples of normal and benign tissue are provided. Normal breast tissue mainly consists of glandular tissue, adipose tissue, and dense and loose fibrous tissue. Glandular tissue can be recognized by structural characteristics, although they are not always as clear as they appear in H&E images as no cytonuclear details can be seen on FF-OCT. The adipose cells are very typical: large hypo-scattering cells which appear black, apart from their membranes. For the supporting fibrous tissue, a wavy architecture corresponds to the loose fibrous tissue. Fibroadenomas are well recognizable on FF-OCT images by the abundance, and size of epithelial tissue and large ducts. Only in 1 out of the 4 FF-OCT images of fibroadenomas one pathologist incorrectly classified it as a an invasive malignancy.

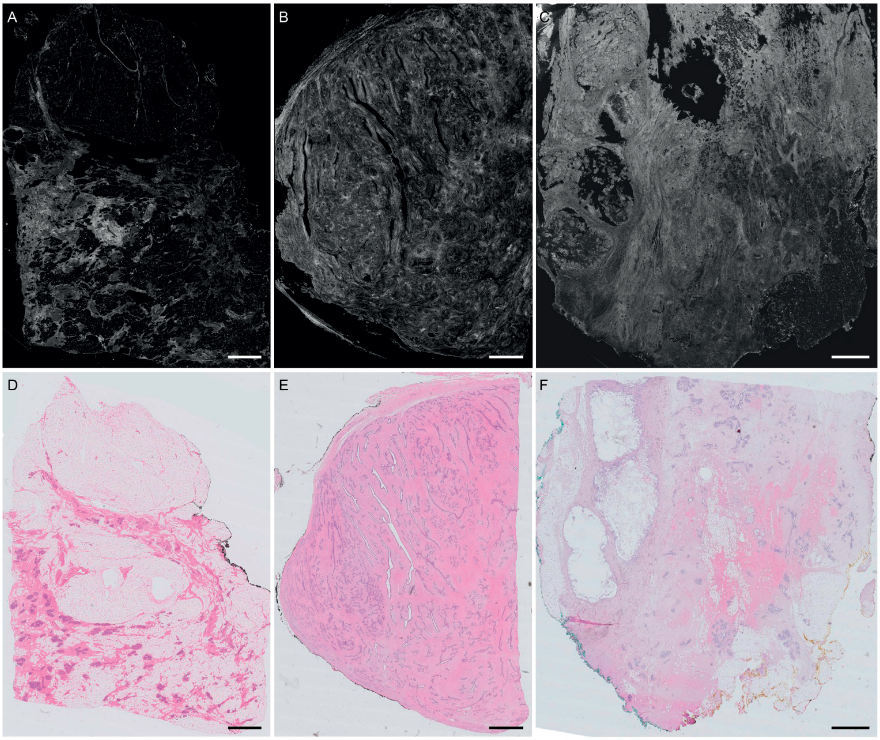

Figure 1. FF-OCT image of normal breast tissue (A), a fibroadenoma (B), and tissue in which the marker was positioned (C), all with their corresponding H&E images (D-F). Scale bars represent 2 mm.

Malignant FF-OCT images

Figure 2 shows examples of both *in situ* carcinoma and invasive ductal carcinoma. Out of the 77 FF-OCT images, 4 were misclassified by both pathologist. all of these were malignant and classified as benign. In two of these cases only some very subtle lobular *in situ* carcinoma was found on H&E examination (Figures 2E and 2F). In one case, a small nest of lymphovascular invasion (LVSI) was found and at the border a small nest of invasive tumor, while the remaining part existed of over 80% of adipose tissue. Upon reviewing this H&E image (which was done after reviewing the FF-OCT images), pathologist 1 already mentioned he would never be able to see this on the FF-OCT images. The last case (Figures 2I and 2L) both contained some *in situ* and invasive carcinoma, and was a grade II IC-NST. The FF-OCT image did not show the typical characteristics, such as a strong stromal reaction. Pathologist 1 did see a lot of epithelial structures, and hesitated to call it *in situ*, but eventually thought the size and amount was not abnormal. He thought it could be atrophic tissue in and older woman.

The fat percentage demonstrated a relationship with diagnostic accuracy (Figure 4). Higher fat percentages in H&E images resulted in a significantly higher number of misdiagnosed cases ($p<0.001$).

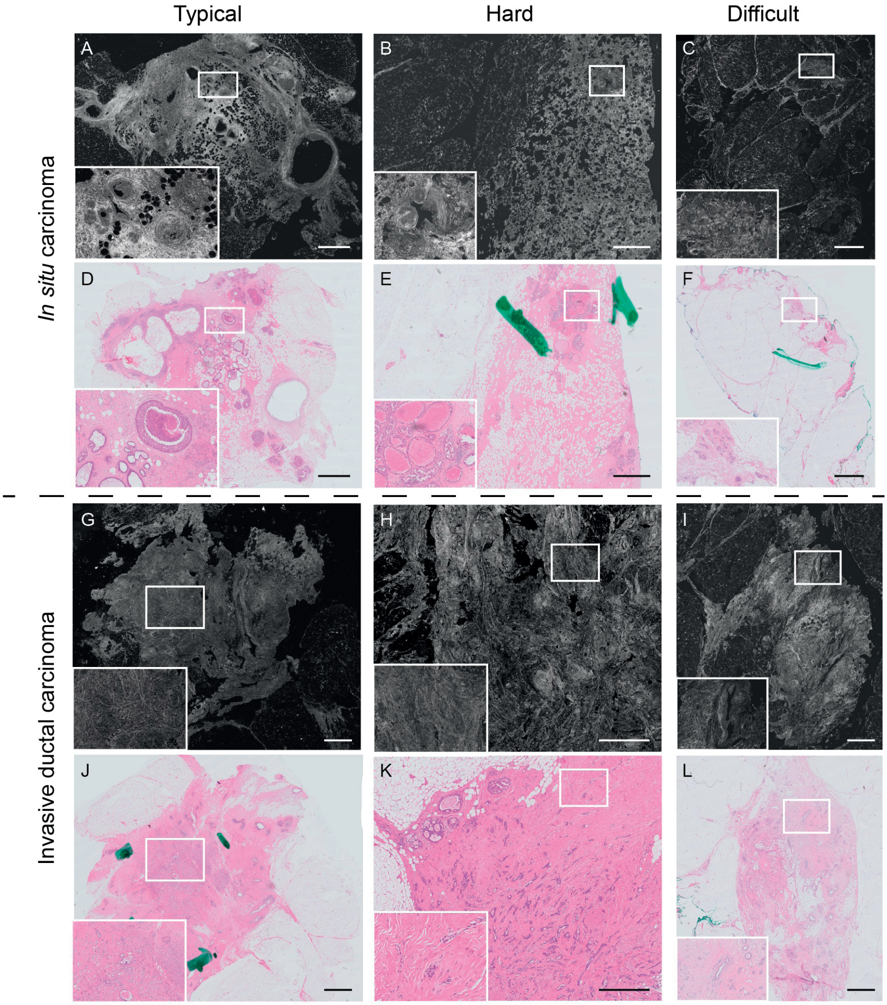

Figure 2. FF-OCT images of *in situ* carcinomas (A-C) and invasive ductal carcinomas (G-I), both with and without typical tumor features recognizable on FF-OCT images, with their corresponding H&E images (D-F, J-L). Some images contain the typical characteristics in abundance, while other only contain either one of them or in a very small amount, making it difficult for pathologist to identify. Scale bars represent 2 mm, except for 2H and K where scale bars represent 1 mm.

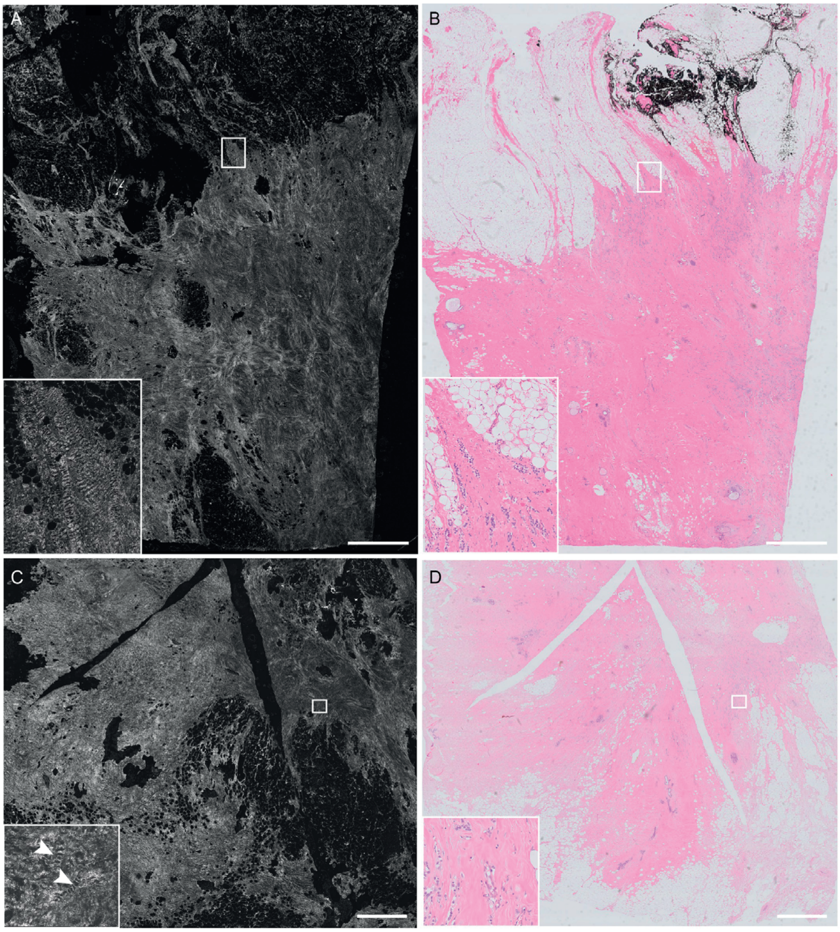

Figure 3. FF-OCT images of an invasive lobular carcinoma (A and C), with their corresponding H&E images (B and D). Scale bars represent 2 mm.

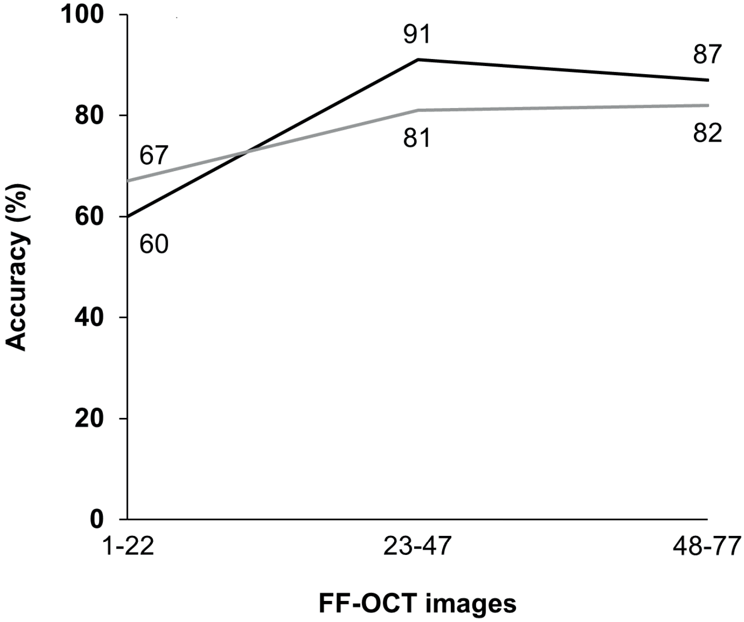

Figure 4. Learning curves of both pathologists.

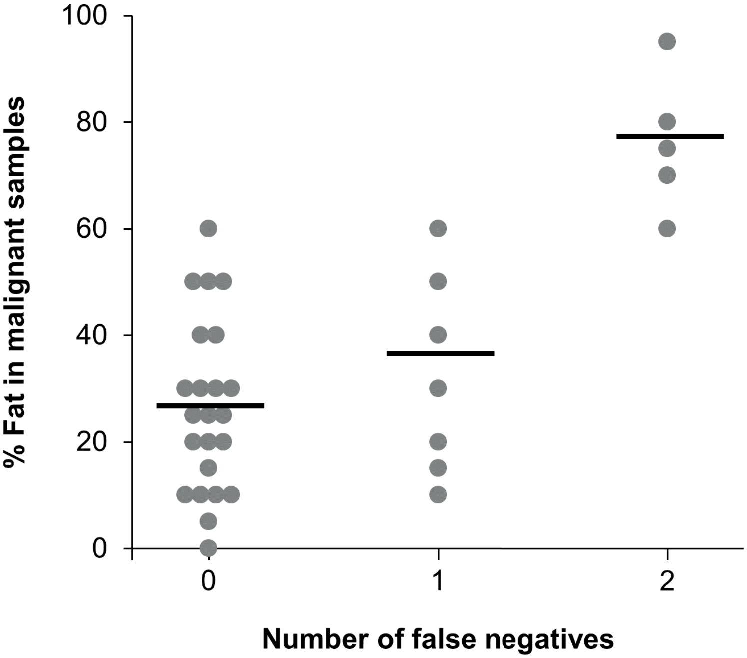

Figure 5. Influence of fat percentage on diagnostic accuracy. (p<0.0001)

Second level interpretation

For the second-level interpretation, pathologist 1 deemed 60 out of 77 cases classifiable and pathologist 2 deemed 50 out of 77 cases classifiable. Table 3 provides their accuracy. In situ carcinoma was hardest to correctly diagnose; only 2 out of 11 (18%) second level interpretations (of both pathologists combined) indicated in situ carcinoma. Major discrepancies mostly were the same cases as the false positives and false negatives of the first level interpretation.

Table 3. Correlation between actual diagnosis and second level interpretation for both pathologists combined. In total 110 second interpretation diagnoses were given.

		Histological assessment			
		Normal	Benign	In situ carcinoma	Invasive carcinoma
FF-OCT assessment	Normal	39	2	4	7
	Benign	1	7	3	-
	In situ carcinoma	-	-	2	2
	Invasive carcinoma	5	3	2	33

DISCUSSION

In this study we investigated whether pathologists were able to distinguish malignant from benign breast tissue based on FF-OCT images. We found that pathologists 1 and 2 reached an accuracy of 81% and 77% respectively. Pathologist 1 was able to interpret the FF-OCT images with a very high specificity (97%), but low sensitivity (63%), while pathologist 2 reached a high sensitivity (86%), but low specificity (68%). Pathologist 2 was more afraid of missing malignancy, pathologist 1 only classified images as malignant when there was a very strong indication. The accuracy we reached is comparable with that of Assayag et al., who reached an accuracy of 83%. This however is not sufficient to eventually use the technique for margin detection in a clinical setting. We do believe that this could be achieved with some adjustments: more extensive training, other contrast mechanisms, and computer aided diagnosis.

To train pathologists effectively, pathologists require direct correlation between H&E and FF-OCT images. However, acquiring FF-OCT images at exactly the same position as H&E coupes are taken, is challenging. We noticed that pathologists were often not very confident on their diagnosis. With more experience and direct feedback, we believe accuracy and confidence of interpretations will grow. This was already seen in the relative small dataset in this study: for both pathologists the learning curve increased (from 60% to 87% for pathologist 1 and from 67% to 82% for pathologist 2). Thereby, other FF-OCT studies also showed an increased accuracy in the assessment of images. In prostate biopsies, accuracy improved from 60% to 80% within one study [31], and was 93% in a later study [32].

Four cases were misdiagnosed by both pathologists, all of them false-positives. In three cases only a very small amount of *in situ* or invasive carcinoma was present, in one case it was a invasive lobular carcinoma grade I. Especially small amounts of tumor, are extremely difficult for pathologists to see in FF-OCT images, as a large part of the diagnosis is made using the architecture and stromal alignment. Images with a lot of fatty tissue, little stroma or only very small amounts of tumor are often mistaken for benign tissue. This was confirmed by our analysis: the amount of fat significantly correlated with the amount of incorrect interpretations. FF-OCT contrast is not sufficient to distinguish intracellular structures nor cytonuclear details. To increase accuracy of FF-OCT image interpretation, more detail is needed, for example to show cell nuclei. Currently, dynamic FF-OCT is being studied to provide enhanced detail, with promising results [33,34]. Dynamic FF-OCT – also label free and non-invasive – visualizes metabolic activity at subcellular scale, by using the time dependence of the FF-OCT signal. Imaging can be performed with a similar setup used in this study, with a CMOS camera with an improved sensitivity.

Thirdly, we think accuracy could be increased by taking advantage of computer aided diagnosis. In previous studies, automated detection algorithms of a-line OCT images were able to distinguish normal breast from tumor tissue with accuracies ranging from 81% to 92% [35–37]. But also in large field images similar to FF-OCT images, automated detection has been proven effectively. Bredfield et al. [38], used tumor associated collagen signatures of breast cancer tissue to automatically detect the tissue type, reaching an overall accuracy of 91.9%. Focusing on collagen topography could even give additional information, as it is associated with a patients prognosis [39].

Finally, in this study, we did not provide clinical data to the pathologists, which is available to them in daily practice. This lack of information made interpretation even harder, as they normally do take this information into account in the interpretation of the histomorphology.

Both pathologists deemed several images uninterpretable, that were excluded from further analysis. These were equally distributed over normal and tumor samples we believe that this exclusion does not represent a specific bias.

Several other groups have studied the use of OCT in breast cancer tissue, showing promising results. One recent study, by Ha *et al*. [40], achieved an average reader accuracy of 87% in assessing OCT images of breast specimens; readers included pathologists, radiologists and surgeons. Yao *et al.* [41], reached a 84% accuracy in assessing OCT images of breast specimens, using an automated classification algorithm. However, both studies suffered from a small dataset and excluded lobular carcinomas. Erickson-Bhatt *et al.* [42], used a hand-held OCT scanner to image resection beds *in vivo* in 35 patients undergoing surgery. Although accuracy rates varied from 58-88% between 5 readers and the study only contained few positive images, this study demonstrated the feasibility of real-time and label-free *in vivo* OCT imaging.

The desired clinical application is intraoperative imaging: looking at resection margins during surgery to lower the re-excision rates for BCS. For this, the system used in this study is not suitable; a handheld and faster device is necessary. Research into handheld OCT systems is extensive, and devices have become better in terms of resolution, speed, costs and size [43]. Also, the first handheld FF-OCT prototype was already described [44], offering new perspectives for *in vivo* imaging.

In this study we showed that pathologists could reach a combined accuracy of 79%. Although this is not yet sufficient, we believe that the measures described above, could improve the accuracy, thereby making it feasible to introduce FF-OCT in the clinical practice.

GRANT SUPPORT

This research was funded by the European Union Seventh Framework Program FP7-ICT-2011-8 under grant agreement number 318729 (CAReIOCA project).

Appendix 1. Reading sheet

Reading sheet OCT beelden MAMMA

Datum:

1. Algemene informatie

Beoordelingsnummer:	Beoordelaar	
Beeldnummer:	Type beeld: positief/negatief/beide	Tijdsduur:
Beeldkwaliteit: slecht /matig/goed		

2. Herkenbare structuren

Herkenbare normale structuren/type weefsels:

☐ Vetweefsel
☐ Stroma
☐ Glandulair weefsel
☐ Stroma
☐ Spierweefsel
☐ Huid

☐ Overig:……………………………………………………………………………………………………

Stromal alignement:……………………………………………………………………………………………

Herkenbare pathologische structuren/type weefsels:

☐ DCIS
☐ LCIS
☐ IDC
☐ ILC
☐ Fibroadenoom
☐ Overig:……………………………………………………………………………………………………
☐ Adenose
☐ Necrose
☐ Retractie artefacten
☐ Microcalcificaties

3. Diagnose

☐ Benigne
☐ Maligne

Specificatie

Normaal	Benigne	In-situ laesie	Invasief
	Mastopatische veranderingen (adenosis, sclerose, cysteus) Fibroadenoom Overig		

REFERENCES

1. F. Bray, Jacques Ferlay, Isabelle Soerjomataram, Siegel; RL, Torre; LA, Jemal A. Global Cancer Statistics 2018: GLOBOCAN Estimates of Incidence and Mortality Worldwide for 36 Cancers in 185 Countries. *CA Cancer J Clin*. 2018. doi:10.3322/caac.21492
2. Senkus E, Kyriakides S, Ohno S, et al. Primary breast cancer: ESMO Clinical Practice Guidelines for diagnosis, treatment and follow-up. *Ann Oncol Off J Eur Soc Med Oncol*. 2015. doi:10.1093/annonc/mdv298
3. Kell MR, Dunne C, Burke JP, Morrow M. Effect of margin status on local recurrence after breast conservation and radiation therapy for ductal carcinoma in situ. *J Clin Oncol*. 2009. doi:10.1200/JCO.2008.17.5182
4. Komoike Y, Akiyama F, Iino Y, et al. Ipsilateral breast tumor recurrence (IBTR) after breast-conserving treatment for early breast cancer: Risk factors and impact on distant metastases. *Cancer*. 2006. doi:10.1002/cncr.21551
5. Houssami N, MacAskill P, Marinovich ML, et al. Meta-analysis of the impact of surgical margins on local recurrence in women with early-stage invasive breast cancer treated with breast-conserving therapy. *Eur J Cancer*. 2010. doi:10.1016/j.ejca.2010.07.043
6. Singletary SE. Surgical margins in patients with early-stage breast cancer treated with breast conservation therapy. *Am J Surg*. 2002. doi:10.1016/S0002-9610(02)01012-7
7. Pleijhuis RG, Graafland M, De Vries J, Bart J, De Jong JS, Van Dam GM. Obtaining adequate surgical margins in breast-conserving therapy for patients with early-stage breast cancer: Current modalities and future directions. *Ann Surg Oncol*. 2009. doi:10.1245/s10434-009-0609-z
8. Butler-Henderson K, Lee AH, Price RI, Waring K. Intraoperative assessment of margins in breast conserving therapy: A systematic review. *Breast*. 2014. doi:10.1016/j.breast.2014.01.002
9. Medina-Franco H, Abarca-Pérez L, García-Alvarez MN, Ulloa-Gómez JL, Romero-Trejo C, Sepúlveda-Méndez J. Radioguided occult lesion localization (ROLL) versus wire-guided lumpectomy for non-palpable breast lesions: A randomized prospective evaluation. *J Surg Oncol*. 2008. doi:10.1002/jso.20880
10. Rahusen FD, Bremers AJA, Fabry HFJ, Taets van Amerongen AHM, Boom RPA, Meijer S. Ultrasound-guided lumpectomy of nonpalpable breast cancer versus wire-guided resection: A randomized clinical trial. *Ann Surg Oncol*. 2002. doi:10.1245/ASO.2002.04.009
11. Angarita FA, Nadler A, Zerhouni S, Escallon J. Perioperative measures to optimize margin clearance in breast conserving surgery. *Surg Oncol*. 2014. doi:10.1016/j.suronc.2014.03.002
12. Wilke LG, Czechura T, Wang C, et al. Repeat surgery after breast conservation for the treatment of stage 0 to II breast carcinoma: A report from the national cancer data base, 2004-2010. *JAMA Surg*. 2014. doi:10.1001/jamasurg.2014.926
13. McCahill LE. Variability in Reexcision Following Breast Conservation Surgery. *JAMA J Am Med Assoc*. 2012. doi:10.1001/jama.2012.43
14. Jeevan R, Cromwell DA, Trivella M, et al. Reoperation rates after breast conserving surgery for breast cancer among women in England: retrospective study of hospital episode statistics. *BMJ*. 2012. doi:10.1136/bmj.e4505

15. van Leeuwen MT, Falster MO, Vajdic CM, et al. Reoperation after breast-conserving surgery for cancer in Australia: statewide cohort study of linked hospital data. *BMJ Open*. 2018;8(4):e020858. doi:10.1136/bmjopen-2017-020858

16. Landercasper J, Whitacre E, Degnim AC, Al-Hamadani M. Reasons for Re-Excision After Lumpectomy for Breast Cancer: Insight from the American Society of Breast Surgeons Mastery^{SM} Database. *Ann Surg Oncol*. 2014. doi:10.1245/s10434-014-3905-1

17. Shipp DW, Rakha EA, Koloydenko AA, Macmillan RD, Ellis IO, Notingher I. Intra-operative spectroscopic assessment of surgical margins during breast conserving surgery. *Breast Cancer Res*. 2018. doi:10.1186/s13058-018-1002-2

18. Phipps JE, Gorpas D, Unger J, Darrow M, Bold RJ, Marcu L. Automated detection of breast cancer in resected specimens with fluorescence lifetime imaging. *Phys Med Biol*. 2018. doi:10.1088/1361-6560/aa983a

19. Zhang J, Rector J, Lin JQ, et al. Nondestructive tissue analysis for ex vivo and in vivo cancer diagnosis using a handheld mass spectrometry system. *Sci Transl Med*. 2017. doi:10.1126/scitranslmed.aan3968

20. Kennedy BF, McLaughlin RA, Kennedy KM, et al. Optical coherence micro-elastography: mechanical-contrast imaging of tissue microstructure. *Biomed Opt Express*. 2014. doi:10.1364/BOE.5.002113

21. Wong TTW, Zhang R, Hai P, et al. Fast label-free multilayered histology-like imaging of human breast cancer by photoacoustic microscopy. *Sci Adv*. 2017. doi:10.1126/sciadv.1602168

22. de Boer LL, Molenkamp BG, Bydlon TM, et al. Fat/water ratios measured with diffuse reflectance spectroscopy to detect breast tumor boundaries. *Breast Cancer Res Treat*. 2015. doi:10.1007/s10549-015-3487-z

23. Huang D, Swanson EA, Lin CP, et al. Optical coherence tomography. *Science (80-)*. 1991. doi:10.1126/science.1957169

24. van Manen L, Dijkstra J, Boccara C, et al. The clinical usefulness of optical coherence tomography during cancer interventions. *J Cancer Res Clin Oncol*. 2018. doi:10.1007/s00432-018-2690-9

25. Dubois A. Full-field optical coherence microscopy. In: *Selected Topics in Optical Coherence Tomography*. Vol 23. Osa; 2012:3-20.

26. Assayag. Large Field, High Resolution Full-Field Optical Coherence Tomography: A Pre-clinical Study of Human Breast Tissue and Cancer Assessment. *TCRT Express*. 2013. doi:10.7785/tcrtexpress.2013.600254

27. Federa. No Title. Code for Proper Secondary Use of Tissue (2001).

28. Dubois A, Grieve K, Moneron G. Ultrahigh-resolution full-field optical coherence tomography. *Appl …*. 2004;43(14):2875-2883.

29. Dubois A, Vabre L, Boccara A-C, Beaurepaire E. High-resolution full-field optical coherence tomography with a Linnik microscope. *Appl Opt*. 2002. doi:10.1364/AO.41.000805

30. Grieve K, Dubois A, Simonutti M, et al. In vivo anterior segment imaging in the rat eye with high speed white light full-field optical coherence tomography. *Opt Express*. 2005. doi:10.1364/OPEX.13.006286

31. Lopater J, Colin P, Beuvon F, et al. Real-time cancer diagnosis during prostate biopsy: ex vivo evaluation of full-field optical coherence tomography (FFOCT) imaging on biopsy cores. *World J Urol*. 2016. doi:10.1007/s00345-015-1620-6

32. Yang C, Ricco R, Sisk A, et al. High efficiency for prostate biopsy qualification with full-field OCT after training. *Photonic Ther Diagnostics XII*. 2016. doi:10.1117/12.2210955
33. Apelian C, Harms F, Thouvenin O, Boccara AC. Dynamic full field optical coherence tomography: subcellular metabolic contrast revealed in tissues by interferometric signals temporal analysis. *Biomed Opt Express*. 2016. doi:10.1364/BOE.7.001511
34. Thouvenin O, Boccara C, Fink M, Sahe J, Păques M, Grieve K. Cell motility as contrast agent in retinal explant imaging with full-field optical coherence tomography. *Investig Ophthalmol Vis Sci*. 2017. doi:10.1167/iovs.17-22375
35. Zysk AM, Nguyen FT, Chaney EJ, et al. Clinical feasibility of microscopically-guided breast needle biopsy using a fiber-optic probe with computer-aided detection. *Technol Cancer Res Treat*. 2009. doi:10.1177/153303460900800501
36. Mujat M, Ferguson RD, Hammer DX, Gittins C, Iftimia N. Automated algorithm for breast tissue differentiation in optical coherence tomography. *J Biomed Opt*. 2009. doi:10.1117/1.3156821
37. Goldberg BD, Iftimia N V., Bressner JE, et al. Automated algorithm for differentiation of human breast tissue using low coherence interferometry for fine needle aspiration biopsy guidance. *J Biomed Opt*. 2008. doi:10.1117/1.2837433
38. Bredfeldt J, Liu Y, Conklin M, Keely P, Mackie T, Eliceiri K. Automated quantification of aligned collagen for human breast carcinoma prognosis. *J Pathol Inform*. 2014. doi:10.4103/2153-3539.139707
39. Dekker TJA, Charehbili A, Smit VTHBM, et al. Disorganised stroma determined on pre-treatment breast cancer biopsies is associated with poor response to neoadjuvant chemotherapy: Results from the NEOZOTAC trial. *Mol Oncol*. 2015. doi:10.1016/j.molonc.2015.02.001
40. Ha R, Friedlander LC, Hibshoosh H, et al. Optical Coherence Tomography: A Novel Imaging Method for Post-lumpectomy Breast Margin Assessment—A Multi-reader Study. *Acad Radiol*. 2018. doi:10.1016/j.acra.2017.09.018
41. Yao X, Gan Y, Chang E, Hibshoosh H, Feldman S, Hendon C. Visualization and tissue classification of human breast cancer images using ultrahigh-resolution OCT. *Lasers Surg Med*. 2017. doi:10.1002/lsm.22654
42. Erickson-Bhatt SJ, Nolan RM, Shemonski ND, et al. Real-time imaging of the resection bed using a handheld probe to reduce incidence of microscopic positive margins in cancer surgery. *Cancer Res*. 2015. doi:10.1158/0008-5472.CAN-15-0464
43. Monroy GL, Won J. Clinical translation of handheld optical coherence tomography: practical considerations and recent advancements. *J Biomed Opt*. 2017. doi:10.1117/1.JBO.22.12.121715
44. Benoit a la Guillaume E, Martins F, Boccara C, Harms F. High-resolution handheld rigid endomicroscope based on full-field optical coherence tomography. *J Biomed Opt*. 2016. doi:10.1117/1.JBO.21.2.026005

4

Validation of full-field optical coherence tomography in distinguishing malignant and benign tissue in resected pancreatic cancer specimens

Labrinus van Manen[*], Paulien L. Stegehuis[*], Arantza Fariña-Sarasqueta, Lorraine M. de Haan, Jeroen Eggermont, Bert A. Bonsing, Hans Morreau, Boudewijn P. F. Lelieveldt, Cornelis J. H. van de Velde, Alexander L. Vahrmeijer, Jouke Dijkstra, J. Sven D. Mieog[*] These authors contributed equally to this work.

PLOS ONE | 2017 Apr 17;12(4):e0175862

ABSTRACT

Background

Pancreatic cancer is the fourth leading cause of cancer-related mortality in the United States. The minority of patients can undergo curative-intended surgical therapy due to progressive disease stage at time of diagnosis. Nonetheless, tumor involvement of surgical margins is seen in up to 70% of resections, being a strong negative prognostic factor. Realtime intraoperative imaging modalities may aid surgeons to obtain tumor-free resection margins. Full-field optical coherence tomography (FF-OCT) is a promising diagnostic tool using high-resolution white-light interference microscopy without tissue processing. Therefore, we composed an atlas of FF-OCT images of malignant and benign pancreatic tissue, and investigated the accuracy with which the pathologists could distinguish these.

Materials and methods

One hundred FF-OCT images were collected from specimens of 29 patients who underwent pancreatic resection for various indications between 2014 and 2016. One experienced gastrointestinal pathologist and one pathologist in training scored independently the FF-OCT images as malignant or benign blinded to the final pathology conclusion. Results were compared to those obtained with standard hematoxylin and eosin (H&E) slides.

Results

Overall, combined test characteristics of both pathologists showed a sensitivity of 72%, specificity of 74%, positive predictive value of 69%, negative predictive value of 79% and an overall accuracy of 73%. In the subset of pancreatic ductal adenocarcinoma patients, 97% of the FF-OCT images (n = 35) were interpreted as tumor by at least one pathologist. Moreover, normal pancreatic tissue was recognised in all cases by at least one pathologist. However, atrophy and fibrosis, serous cystadenoma and neuroendocrine tumors were more often wrongly scored, in 63%, 100% and 25% respectively.

Conclusion

FF-OCT could distinguish normal pancreatic tissue from pathologic pancreatic tissue in both processed as non-processed specimens using architectural features. The accuracy in pancreatic ductal adenocarcinoma is promising and warrants further evaluation using improved assessment criteria.

INTRODUCTION

Pancreatic cancer is the fourth leading cause of cancer related deaths with a 5-year survival rate of 8% in the United States [1]. Many patients present with locally advanced or metastasized disease and are beyond cure. Patients diagnosed with localized disease can undergo a potentially curable treatment and have a 5-year survival rate around 20% [2±4]. Treatment consists of high-risk surgery (morbidity of 40±50% and mortality around 5% [5, 6]) usually followed or preceded by chemo(radio)therapy. During surgery, it is important to achieve a complete (R0) resection, as a distance of the tumor from the resection margin of _1 mm (R1 resection) is one of the most important prognosticators for poor survival in Europe [2, 7±9]. However, adequate intraoperative judgment is challenging, because the surgeon has to rely on visual inspection and palpation only. The presence of peritumoral inflammation in pancreatic cancer makes the distinction with normal tissue even more difficult. The incidence of R1 resections is up to 60±80% in published series of standardized pathological assessment [8±13], underlining the importance of adequate intraoperative resection margin assessment.

Although various imaging modalities (such as CT, MRI, EUS and PET) are used to diagnose pancreatic cancer and assess its resectability prior to surgery, only few techniques are suitable during surgery [14]. Frozen section analysis is currently the most used intraoperative modality, especially to assess extra-pancreatic lesions [15]. However, it has low sensitivity (38%) evaluating resection margins, and is therefore only used in selected cases at our institution [15]. Intraoperative ultrasound can be used to detect metastases or assess resectability, but its value in reducing positive resection margins is unknown, [14] and is the study object of an ongoing clinical trial at our institution. An emerging technique is near-infrared fluorescence imaging, which is based on a fluorescent tracer and dedicated cameras. Pre-clinical results demarcating pancreatic tumor are promising, but use tracers that are currently not yet FDA approved [16]. Thus, the current state-of-the art surgical approach encompasses high-risk intervention with limited success and little to no intraoperative visualisation of the malignant process. Novel intraoperative imaging tools are needed to improve the assessment of resectability and to guide subsequent resection.

Optical coherence tomography (OCT) was first described in 1991 and uses low-coherence interferometry to produce 2-dimensional cross-sectional images [17]. It is already standard-of-care in ophthalmology and cardiology, and with the development of new OCT modalities, other fields of interest – like oncology – are being discovered [18]. Full-field OCT (FF-OCT) is such a newly developed modality, based on the principles of white light interference microscopy, and acquires *en face* images by illuminating the whole field of view without scanning [19]. It enables non-invasive high-resolution imaging up to several millimetres of tissue without the need for tissue processing, by measuring the backscattered light of tissue structures with different refractive indices. Several studies report the use of FF-OCT in the field of oncology, i.e. on ovarian [20], skin [21] and brain tissue [22]. All showed encouraging results; architectural changes could be identified, and in a quick fashion a large surface could be scanned. Only one study has been conducted in pancreatic cancer, but this was to evaluate fine needle aspirates [23]. FF-OCT has not yet been tested in pancreas resection specimens to discriminate malignant and benign tissues.

In this feasibility study, we investigated whether pathologists were able to distinguish malignant from normal and benign pancreatic tissue based on FF-OCT images, obtained from surgical specimens.

MATERIALS AND METHODS

Patient and sample selection

Twenty-nine patients who underwent surgery for suspect pancreatic cancer at the Leiden University Medical Center (LUMC) were included in this study. Fresh tissue samples were collected prospectively (October 2015 until January 2016) from surgical specimens from 17 patients with (pre)malignant pancreatic lesions. Formalin-fixed paraffin embedded (FFPE) samples from 12 patients were collected retrospectively (January 2014 until December 2014) from both benign and malignant pancreatic neoplasms to acquire FF-OCT images of different pancreatic neoplasms. No patients with a preoperative diagnosis of benign disease were included, for instance, patients with chronic or auto-immune pancreatitis were not included. From each of the 29 patients, if achievable, minimal one tissue section with presence of tumor and one tissue section without tumor were obtained. For the fresh samples, the selection was based on the macroscopic assessment by the pathologist; for FFPE samples, the selection was based on microscopic assessment. This resulted in 50 tissue samples (25 fresh samples and 25 FFPE samples). Per tissue sample, two regions of interest were selected by the study coordinator, LM, based on the corresponding H&E slides. These two regions of interest from a single tissue sections could be either both benign, both malignant or one malignant and one benign.

FFPE tissue blocks were deparaffinised, using a standard protocol. The study protocol was approved by the local medical ethics committee of the LUMC. The prospective collection of the fresh tissue samples was performed within the framework of routine clinical care. Therefore patient consent was not obtained, as this study was not subject to the Dutch Medical Research Involving Human Subjects Act, according to our local medical ethics committee. One author (LM) had access to patient information during clinical data acquisition after which patient data were anonymized. All patient samples and clinical data were handled in accordance with the medical ethics guidelines described in the Code of Conduct for the Proper Secondary Use of Human Tissue of the Dutch Federation of Biomedical Scientific Societies [24].

FF-OCT imaging and sample processing

Images were obtained using a high resolution FF-OCT system (Light-CT™ scanner, LLTech SAS, Paris, France). In short, the setup consists of an upright microscope with a 10x objective, a halogen light-source with wavelength of 700±125 nm, and a reference arm in Linnik interferometric configuration [25, 26]. It generates high resolution (1.5 µm isotropic), 0.8 by 0.8 mm *en face* images, but the field of view is increased using image mosaicking (with a maximum diameter of 25 mm), at an image rate of 35 Hz. Image depth is adjustable, with a maximum depth of several millimeters, depending on tissue properties [27].

Tissue samples were placed in a sample holder in 0.9% NaCl solution with the surface to be imaged facing upward. A glass slide was positioned above the tissue to which it was gently flattened, and a layer of silicone oil was applied between the optical window and the microscope objective. A macroscopic image was obtained using a wide-field camera, followed by FF-OCT images. To ensure good correspondence with the histology images, FF-OCT images were acquired at a depth of around 20 µm. Imaging time for one sample was on average 30 minutes. After FF-OCT imaging, tissue samples were formalin fixed and embedded in paraffin. H&E slides were obtained and digitalised with a digital pathology slide scanner (IntelliSite Ultra Fast Scanner, Philips, Eindhoven, the Netherlands). FF-OCT images were viewed using in-house developed analysis software based on MeVisLab (MeVis Medical Solutions AG and Fraunhofer MEVIS, Germany).

Study design

Two pathologists – one experienced and one resident – followed a brief training prior to assessment of the FF-OCT images. The training was divided in two parts: in the first part the technique and method of tissue imaging were explained, and in the second part FF-OCT images were shown with their corresponding H&E images. The images of this training atlas were magnified regions of interest showing details of the different pancreatic tissues (such as normal pancreas, pancreatitis and pancreatic ductal adenocarcinoma (PDAC)); the whole slide was not presented to the pathologists. Moreover, the regions of interest used in the training atlas were different in the test cohort.

The 100 regions of interest to be assessed by the pathologists were shown in the context of both the total FF-OCT image, and an enlarged (detail) image. They were offered to the pathologists in both the original and inverse setting, as shown in Fig 1. During assessment pathologists were able to digitally zoom the images. FF-OCT images were randomly presented in the same order to the pathologists who were blinded to the H&E slides, patient information and final pathological diagnosis of the specimen. The pathologists had to classify the marked region-of-interest as malignant or benign. If the pathologists found that the image quality was too poor to reach a decision, it was classified as not interpretable.

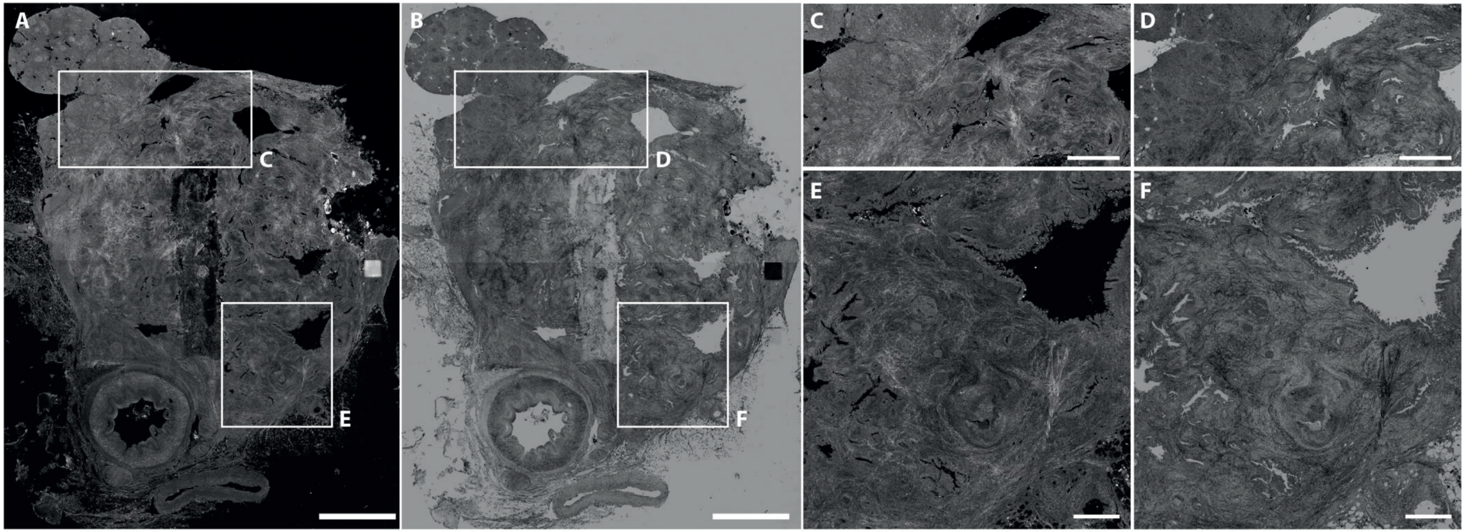

Figure 1. Example FF-OCT image of a well-differentiated pancreatic ductal adenocarcinoma as shown to the pathologist for assessment. The whole FF-OCT images were shown to the pathologists, but they were asked to only assess the selected regions of interest (two per FF-OCT image). Both the original (A,C,E) and the inverse (B,D,F) FF-OCT images are shown. Scale bars, 5 mm (A,B), 2 mm (C,D), and 1 mm (E,F).

Statistical analysis

The results of the individual region-of-interest scores were put in a 2x2 contingency table to calculate sensitivity, specificity, positive predictive value (PPV), negative predictive value (NPV) and accuracy for the complete cohort. In addition, diagnostic test characteristics and the interobserver variability were calculated after each cohort of 25 consecutive FF-OCT images. SPSS version 23 (IBM Corporation, Armonk, NY, USA) was used to calculate the interobserver variability and to compare the agreement in tumor identification by both pathologists, for which chi-squared tests were used. Kappa values were interpreted as described by Landis et Koch [28]. P<0.05 was considered statistical significant. Graphs were created using Graphpad version 7 (Graphpad Software, La Jolla, CA, USA).

RESULTS

In FF-OCT images of normal pancreatic tissue, the morphologic features of major components could be identified, like interlobular septae, acinar tissue, islet cells, pancreatic ducts and blood vessels (Fig 2). Recognition of nerve bundles in normal pancreatic tissue was difficult (Fig 2). Interlobular septae are visible as light grey strands which are located between the lobuli. Islet cells were recognised as highlighted groups of cells located in acinar tissue.

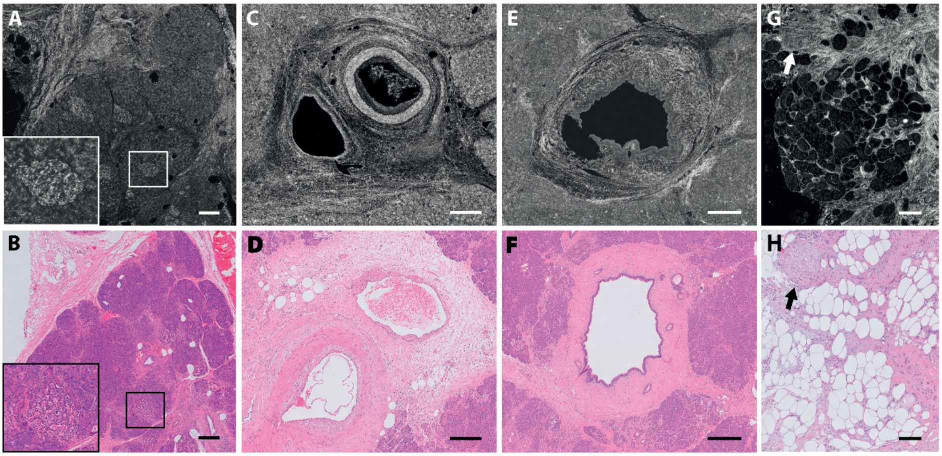

Figure 2. Examples of FF-OCT images of normal pancreatic tissue and corresponding histology. Structures that are easily identified on FF-OCT images include normal pancreatic parenchyma (A-B), vessels (C-D), and a large pancreatic duct (E-F). Harder to recognize are nerve bundles (G-H). Scale bars, 250 µm (A-B, G-H), and 150 µm(C-F). Inset shows an islet of Langerhans (A-B) at 2.5 times higher magnification.

Histomorphology of pancreatic cancer in general and especially of PDAC is complex, being sometimes challenging to distinguish between malignant and reactive, benign glands in the context of pancreatitis even on H&E images [29]. On H&E images various criteria are used to distinguish between benign and malignant tissue. First of all, the pathologists look at low magnification level to detect the presence of normal pancreatic architecture. Desmoplastic stroma, irregular ducts and disorganised glands are characteristics that indicate potential malignancy. Atypical cell nuclei, intraluminal necrosis, perineural invasion and ingrowth into structures as lymph nodes, blood vessels and fat tissue are all characteristics that point toward malignancy. If the lobular structure is maintained even in the presence of irregular ducts with some cytonuclear atypia, pancreatitis should be considered. However, the difficulty resides in the fact that these essential features for the diagnostic on H&E slides are regularly not evaluable on the FF-OCT images. As shown in Table 1, only stroma and architectural distortion of pancreatic tissue and tumor glands are easily recognizable on FF-OCT images.

Table 1. Comparison of features of pancreatic ductal adenocarcinoma detectable on H_E and on FF-OCT images.

Features of malignancy	Detectable on H&E[a]	Detectable on FF-OCT
Disorganisation of lobuli and glands	+	+
Presence of atypical glands	+	±[b]
Atypical cell nuclei	+	-
Presence of tumor stroma	±	+
Ingrowth into structures (a.o. lymph nodes, blood vessels, fat)	+	±
Intraluminal necrosis	+	±
Perineural invasion	+	±

[a] Adapted from Hruban et al. [28], these diagnostic characteristics are used in assessment of H&E images.

[b] Large atypical glands could be detected, but smaller glands are less visible and sometimes mistaken for blood vessels.

Scoring FF-OCT images

Fifty samples from 29 patients have been included in this study. Patient and tumor characteristics are presented in Table 2. Of these tissue samples, 100 FF-OCT images were available for assessment: 57 benign and 43 malignant sections. The results of the FF-OCT assessment by the pathologists are detailed in Table 3 (and in S1 File). The more experienced gastrointestinal pathologist scored 6 images as not interpretable, the pathologist in training none. Of these 6 images± 3 fresh and 3 deparaffinised FFPE± 3 were benign and 3 were malignant. These images were scored by the pathologist in training; 3 images were scored correctly, and 3 images were scored incorrectly. Leaving these 6 images out of the analysis, the experienced pathologist achieved a higher accuracy than the less experienced pathologist: 80% versus 67%, respectively. The combined results showed the following test characteristics: sensitivity of 72%, specificity of 74%, PPV of 67%, NPV of 79% and an accuracy of 73%.

Table 2. Patient and tumor characteristics

Characteristics	
Age, *mean* (y)	65.7
Sex, n (%)	
Male	13 (45)
Female	16 (55)
ASA score, *n* (%)	
1	5 (17)
2	19 (66)
≥3	5 (17)
Tumor size (mm), *mean*	33.2
Tumor location, n (%)	
Pancreatic head	13 (45)
Pancreas body/tail	10 (35)
Distal CBD	1 (3)
Peri-ampullar	5 (17)
Histological diagnosis, n (%)	
Adenocarcinoma	23 (79)
Well differentiated	3
Moderately differentiated	10
Poorly differentiated	7
Unknown[a]	3
IPMN	1 (3)
MCN	2 (7)
NET	2 (7)
Serous cystadenoma	1 (3)
Surgical procedure, n (%)	
PPPD	17 (59)
Whipple	1 (3)
Distal pancreatectomy	9 (31)
Central pancreatectomy	1 (3)
Total pancreatectomy	1 (3)

[a] Differentiation grade could not be determined in 3 cases, because of pancreatic fibrosis after neoadjuvant (chemo)radiotherapy.

Abbreviations:

ASA: American Society of Anesthesiologists; CBD: Common bile duct; PPPD: Pylorus-preserving pancreaticoduodenectomy; IPMN: Intraductal papillary mucinous neoplasm; MCN: Mucinous cystic neoplasm; NET: *Neuroendocrine* tumor

Table 3. Test characteristics of FF-OCT on pancreatic tissue. True positives are FF-OCT images which were correctly identified as malignant. True negatives are FF-OCT images which were correctly identified as benign. False positives are FF-OCT images which were incorrectly identified as malignant. False negatives are FF-OCT images which were incorrectly identified as benign. Pathologist 1 is the experienced pathologist, pathologist 2 is the pathologist in training.

Pathologist	True positive	True negative	False positive	False negative	Not interpretable	Sensitivity	Specificity	Accuracy
1	28	47	8	11	6	72%	85%	80%
2	30	37	21	12	0	71%	64%	67%
Overall (mean)	29	42	15	12	3	72%	74%	73%

A more detailed overview of the scores per histologic type is provided in Table 4. Normal pancreatic parenchyma was correctly recognised by both pathologists in 32 of the 40 cases. Atrophy and fibrosis (Fig 3) were wrongly scored by both pathologists in 63%, serous cystadenoma in 100% and neuroendocrine tumors in 25% of the cases. Pathologists evaluated 35 FF-OCT images of a PDAC (Fig 4), of which 34 were correctly scored as malignant by at least one pathologist. Well (grade 1) and moderately (grade 2) differentiated PDAC were scored as malignant by both pathologists in 67% and 57% of cases, respectively (Table 4). Whereas, poorly differentiated (grade 3) PDAC was scored as malignant by both pathologist in 1 out of 8 cases (13%).

Table 4. Accuracy per histological diagnosis

	Correctly identified by both pathologists	Correctly identified by one pathologist	None correctly identified
Benign			
Normal pancreatic parenchyma	32	8	0
Pancreatitis	1	2	0
Atrophy or fibrosis	1	2	5
Serous cystadenoma	0	0	2
Mucinous cystic neoplasm	1	0	0
Malignant			
Grade 1 NET	0	1	1
Grade 2 NET	1	1	0
Grade 1 PDAC	4	2	0
Grade 2 PDAC	12	8	1
Grade 3 PDAC	1	7	0
Malignant IPMN	1		
Total[a]	**54**	**31**	**9**

[a] 6 images were scored as not interpretable by one of the pathologists, these are excluded from this analysis.

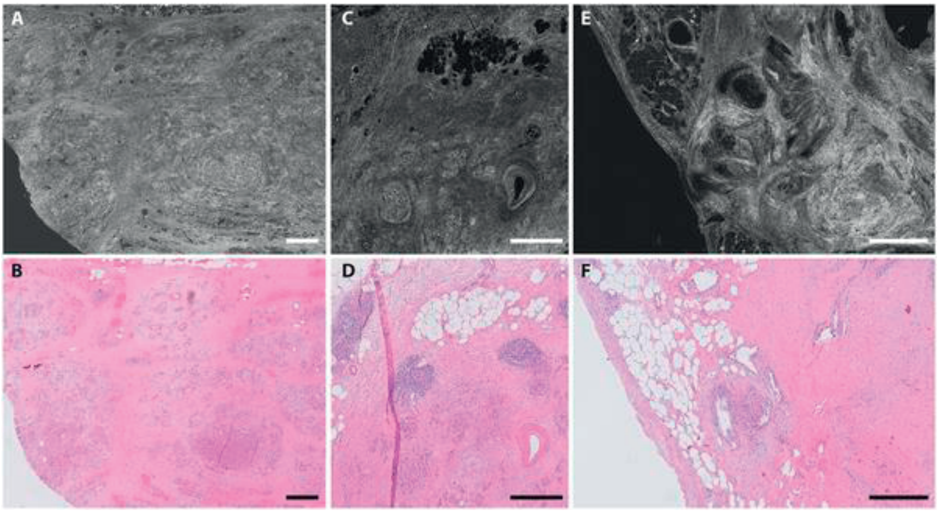

Figure 3. Example of benign pancreatic tissue FF-OCT images and corresponding histology. Fibrotic pancreatic tissue after neoadjuvant therapy (A-B), pancreatitis (C-D), and a serous cystadenoma (E-F); scale bars all 500 µm.

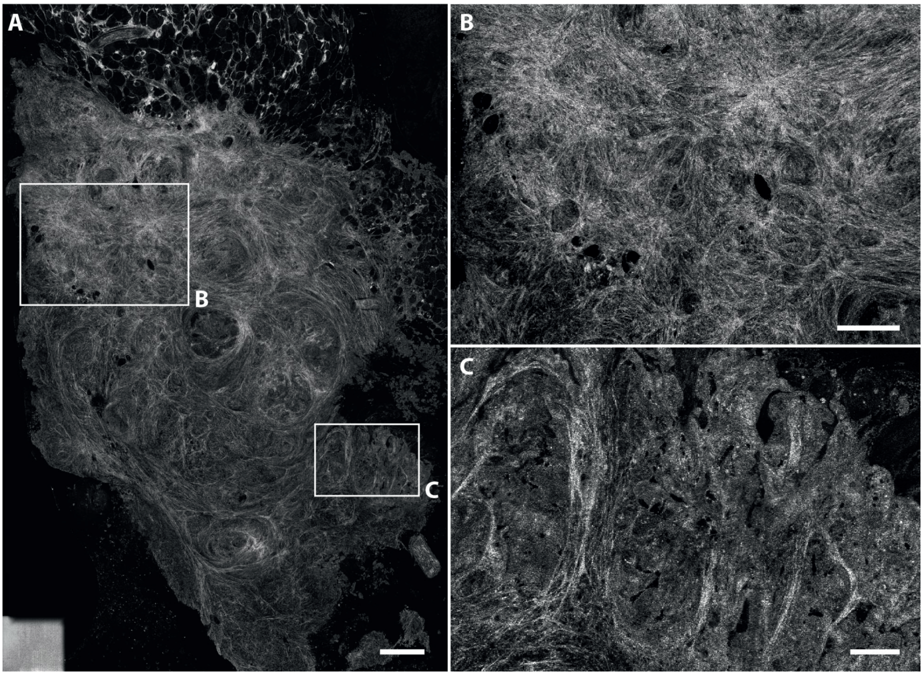

Figure 4. Example FF-OCT image of a well differentiated pancreatic ductal adenocarcinoma. A shows a n overview. B shows a magnified view of stromal disorganization, and C shows nests of tumor cells. Scale bars, 2 mm (A), 1 mm (B), and 500 µm (C).

The first 50 FF-OCT images given to the pathologists were taken from deparaffinised FFPE pancreatic tissue specimens, whereas the others were taken from fresh specimens. Univariate analysis showed no significant difference (P = 0.24) in evaluating fresh or deparaffinised FFPE FF-OCT images, however, fresh FF-OCT images appear to provide a more detailed view and improved visualization of tumor stroma.

Interobserver variability

The overall interobserver variability (Kappa) was calculated and there was a fair agreement between the pathologists (Kappa: 0,33). After presentation of each set of 25 consecutive FF-OCT images the interobserver variability was measured and an increase of 0.1 to 0.5 was observed, as shown in Fig 5.

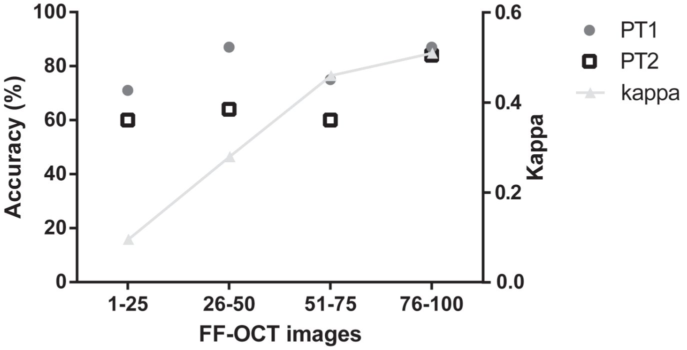

Figure 5. Accuracy and interobserver variability. Pathologist 1 is the experienced pathologist, pathologist 2 is the pathologist in training.

DISCUSSION

In this study we investigated whether pathologists were able to distinguish malignant from benign pancreatic tissue based on FF-OCT images. We found that normal, healthy pancreatic tissue could be distinguished from malignant tissue very well due to the characteristic architecture of normal pancreatic parenchyma. Distinguishing other benign tissue types like chronic pancreatitis was harder. We also found that the experienced pathologist was better in assessing the FF-OCT images than the pathologist in training. To our knowledge this is the first study to evaluate the correlation between H&E slides and FF-OCT in detecting malignancies in fixated and fresh pancreatic resection specimens. The diagnostic accuracy of 73% obtained in this study is not yet adequate, but we believe this can be improved upon by taking several measures: using other contrast mechanisms, improving knowledge on collagen topology, and more extensive training.

Pancreatic pathology and in particular morphological differentiation between pancreatic ductal adenocarcinoma and pancreatitis is challenging even on H&E. On FF-OCT this differentiation is difficult as well; although FF-OCT provides high resolution, the endogenous contrast is not proficient to see cell nuclei. Techniques to reveal subcellular metabolic contrast are being developed, showing encouraging results [30]. Other contrast mechanisms can provide additional information and thereby increase diagnostic accuracy.

Secondly, improved knowledge on the collagen topology could increase the diagnostic accuracy. As collagen reflects light very well, tumor stroma is evidently visible on FF-OCT images. The pathologists mostly evaluated the FF-OCT images based on these architectural features. However in this study, both pathologists often misdiagnosed pancreatic atrophy and fibrosis as malignant. In these cases the presence of collagen fibers dominating the image could be mistaken for tumor stroma as PDAC is characterized by extensive and disorganized desmoplastic stroma [31]. Recently it was shown that its collagen topology differs significantly from that of pancreatitis [32]. Improved knowledge on the collagen topology of these benign conditions, and possibilities to detect these differences and correlation between stromal alignment and organization, and diagnosis, could increase the diagnostic accuracy. This feature could also be exploited in the future by automated detection of collagen characteristics, as was previously done for second harmonic generation images of breast cancer [33].

Our study consisted of two parts: 50 image regions of deparaffinised tissue and 50 image regions of fresh tissue shown to the pathologists in that order. In tissue imaged both fresh and deparaffinised we see that the intensity of collagen is higher in fresh tissue (S1 Fig). We did not find significant differences in the assessment between these parts. However, an increase in accuracy was shown for both pathologists in the second half (images 26±50 and 76±100) of each part, suggesting a learning curve. Another study on FF-OCT where they looked at prostate biopsies showed an overall accuracy of 70%, with a learning curve from 60% to 80% after evaluation of 119 images; this is concordant with our data [34]. A later study on FF-OCT images of prostate core biopsies showed, after extensive training an overall accuracy of 93%. This implies that for pancreatic tissues further improvement is possible [35], therefore we believe that more training could further improve the diagnostic accuracy. We made a flowchart for assessment of pancreatic FF-OCT images which could support pathologists, although it should be validated in future studies (Fig 6).

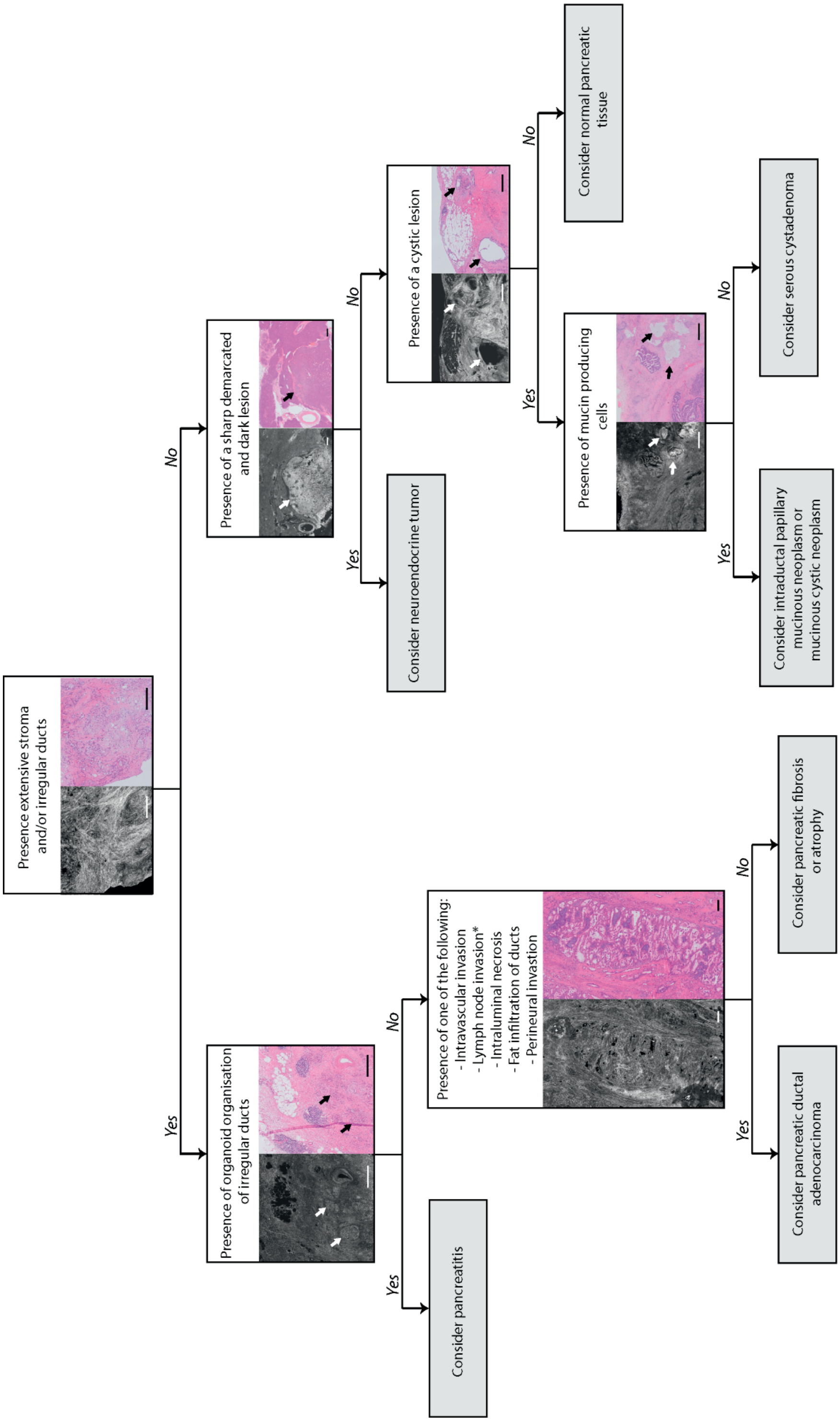

Figure 6. Proposed decision tree to evaluate pancreatic FF-OCT images. Scalebars are all 500 µm. *The FF-OCT image and corresponding histology image only depict lymph node invasion.

Finally, we did not provide any clinical data to the pathologists. This lack of clinical information made interpretation even more difficult as compared to daily practice when such information is available and taken into account in the interpretation of the histomorphology.

We have not imaged resection margins of the surgical specimens as that would have affected the clinical workflow too much, however, we included fresh pancreatic tissue for imaging to mimic the future application of intraoperative use. Moreover, we selected interesting and clinically relevant locations on the H&E and the corresponding FF-OCT images; for example, transition zones of infiltrating tumor glands and surrounding tissue (S2 Fig). Furthermore, to achieve an R0 resection margin in Europe, imaging up to 1 mm is necessary. In this study, we imaged at a depth of 20 µm to ensure good correspondence with reference H&E. As resolution decreases with increasing imaging depth, future studies should analyze the influence on accuracy with increased imaging depth.

The more experienced pathologist did not find the imaging quality good enough to give a diagnosis in six cases that were excluded from further analysis. These images were equally distributed between the different groups (malignant, benign, fresh, deparaffinised) we believe that this exclusion does not represent a specific bias.

Several other groups tried to identify pancreatic tumor tissue in order to reduce the amount of positive margins during surgery using various techniques. Hu et al. [36] used nonlinear optical microscopy to image pancreatic tumor xenografts harvested at different stages. They also saw an increased density of the collagen fibers in tumor compared with normal tissue. However, they did not do a blind reading of the images. Eberlin et al. [37], used mass spectrometry imaging and an automatic classifier to distinguish normal from cancer human pancreas tissue. They obtained a high agreement with pathology, but excluded cellular compositions that were not accounted for in their classifier, such as inflammation and necrosis, which is in contrast with our study, which included a broad spectrum of benign areas of disease to mimic clinical scenarios. Also our group studied the use of fluorescence-guided surgery during pancreatic resections. However, in human studies the results have been disappointing so far, as no useful tumor demarcation could be visualized with non-specific contrast agents [38, 39]. Currently, studies using tumor-specific fluorescent contrast agents are ongoing (Trial ID:NTR5673) [40].

Resection margins can either be examined *in vivo* before and during resection and after resection in the resection bed, or *ex vivo* on the resected specimen. Erickson-Bhatt et al. [41], used a portable OCT system to image the resection bed after a wide local excision of breast cancer. Tao *et al*. [42], also looked at resection margins in breast cancer, but examined *ex vivo* frozen sections using nonlinear microscopy, reaching an accuracy of 94.1%. We envision that FF-OCT could eventually be used during surgery at clinically suspect resection margins to further improve radical resection rates by extending the resection margin to facilitate *en bloc* tumor removal or by resecting additional tissue after suggestion of residual disease.

The FF-OCT device used in this study is not yet applicable in surgery. For translation into the operating room for *in vivo* imaging a handheld and faster device is necessary; for *ex vivo* assessment of resected specimens a bench top system is sufficient. Progression is made on both accounts. The first handheld endomicroscope based on FF-OCT was recently described by Benoit a la Guillaume et al. [43], which opens new perspectives for *in vivo* imaging. Furthermore, a 7 times faster and 3 times more sensitive camera was introduced in the device, also bringing it closer to clinical implementation [44].

In conclusion, FF-OCT could distinguish normal pancreatic tissue from pathologic pancreatic tissue, however, further development of the FF-OCT device and more experience in evaluating FF-OCT images of the pancreas is necessary before introduction in the clinical practice of pancreatic surgery.

REFERENCES

1. Siegel RL, Miller KD, Jemal A. Cancer statistics, 2016. CA Cancer J Clin. 2016; 66(1):7±30. https://doi.org/10.3322/caac.21332 PMID: 26742998
2. Wagner M, Redaelli C, Lietz M, Seiler CA, Friess H, Buchler MW. Curative resection is the single most important factor determining outcome in patients with pancreatic adenocarcinoma. Br J Surg. 2004; 91 (5):586±94. https://doi.org/10.1002/bjs.4484 PMID: 15122610
3. Reddy S, Wolfgang CL, Cameron JL, Eckhauser F, Choti MA, Schulick RD, et al. Total pancreatectomy for pancreatic adenocarcinoma: evaluation of morbidity and long-term survival. Ann Surg. 2009; 250 (2):282±7. https://doi.org/10.1097/SLA.0b013e3181ae9f93 PMID: 19638918
4. Neoptolemos JP, Stocken DD, Bassi C, Ghaneh P, Cunningham D, Goldstein D, et al. Adjuvant chemotherapy with fluorouracil plus folinic acid vs gemcitabine following pancreatic cancer resection: a randomized controlled trial. JAMA. 2010; 304(10):1073±81. https://doi.org/10.1001/jama.2010.1275 PMID: 20823433
5. Tran KT, Smeenk HG, van Eijck CH, Kazemier G, Hop WC, Greve JW, et al. Pylorus preserving pancreaticoduodenectomy versus standard Whipple procedure: a prospective, randomized, multicenter analysis of 170 patients with pancreatic and periampullary tumors. Ann Surg. 2004; 240(5):738±45. https://doi.org/10.1097/01.sla.0000143248.71964.29 PMID: 15492552
6. Yeo CJ, Cameron JL, Sohn TA, Coleman J, Sauter PK, Hruban RH, et al. Pancreaticoduodenectomy with or without extended retroperitoneal lymphadenectomy for periampullary adenocarcinoma: comparison of morbidity and mortality and short-term outcome. Ann Surg. 1999; 229(5):613±22; discussion 22±4. PMID: 10235519
7. Nitschke P, Volk A, Welsch T, Hackl J, Reissfelder C, Rahbari M, et al. Impact of Intraoperative Reresection to Achieve R0 Status on Survival in Patients With Pancreatic Cancer: A Single-center Experience With 483 Patients. Ann Surg. 2016.
8. Delpero JR, Bachellier P, Regenet N, Le Treut YP, Paye F, Carrere N, et al. Pancreaticoduodenectomy for pancreatic ductal adenocarcinoma: a French multicentre prospective evaluation of resection margins in 150 evaluable specimens. HPB (Oxford). 2014; 16(1):20±33.
9. Neoptolemos JP, Palmer DH, Ghaneh P, Psarelli EE, Valle JW, Halloran CM, et al. Comparison of adjuvant gemcitabine and capecitabine with gemcitabine monotherapy in patients with resected pancreatic cancer (ESPAC-4): a multicentre, open-label, randomised, phase 3 trial. Lancet. 2017.
10. Esposito I, Kleeff J, Bergmann F, Reiser C, Herpel E, Friess H, et al. Most pancreatic cancer resections are R1 resections. Ann Surg Oncol. 2008; 15(6):1651±60. https://doi.org/10.1245/s10434-008-9839-8 PMID: 18351300
11. Campbell F, Smith RA, Whelan P, Sutton R, Raraty M, Neoptolemos JP, et al. Classification of R1 resections for pancreatic cancer: the prognostic relevance of tumour involvement within 1 mm of a resection margin. Histopathology. 2009; 55(3):277±83. https://doi.org/10.1111/j.1365-2559.2009.03376.x PMID: 19723142
12. Jamieson NB, Foulis AK, Oien KA, Going JJ, Glen P, Dickson EJ, et al. Positive mobilization margins alone do not influence survival following pancreatico-duodenectomy for pancreatic ductal adenocarcinoma. Ann Surg. 2010; 251(6):1003±10. https://doi.org/10.1097/SLA.0b013e3181d77369 PMID: 20485150

13. Verbeke CS, Gladhaug IP. Resection margin involvement and tumour origin in pancreatic head cancer. Br J Surg. 2012; 99(8):1036±49. https://doi.org/10.1002/bjs.8734 PMID: 22517199
14. Handgraaf HJ, Boonstra MC, Van Erkel AR, Bonsing BA, Putter H, Van De Velde CJ, et al. Current and future intraoperative imaging strategies to increase radical resection rates in pancreatic cancer surgery. Biomed Res Int. 2014; 2014:890230. https://doi.org/10.1155/2014/890230 PMID: 25157372
15. Nelson DW, Blanchard TH, Causey MW, Homann JF, Brown TA. Examining the accuracy and clinical usefulness of intraoperative frozen section analysis in the management of pancreatic lesions. American journal of surgery. 2013; 205(5):613±7; discussion 7. Epub 2013/04/18. https://doi.org/10.1016/j. amjsurg.2013.01.015 PMID: 23592172
16. Boonstra MC, Tolner B, Schaafsma BE, Boogerd LS, Prevoo HA, Bhavsar G, et al. Preclinical evaluation of a novel CEA-targeting near-infrared fluorescent tracer delineating colorectal and pancreatic tumors. Int J Cancer. 2015; 137(8):1910±20. https://doi.org/10.1002/ijc.29571 PMID: 25895046
17. Huang D, Swanson EA, Lin CP, Schuman JS, Stinson WG, Chang W, et al. Optical coherence tomography. Science (New York, NY). 1991; 254(5035):1178±81. Epub 1991/11/22.
18. Vakoc BJ, Fukumura D, Jain RK, Bouma BE. Cancer imaging by optical coherence tomography: preclinical progress and clinical potential. Nat Rev Cancer. 2012; 12(5):363±8. https://doi.org/10.1038/nrc3235 PMID: 22475930
19. Dubois A. Full-Field Optical Coherence Microscopy. In: Liu G, editor. Selected Topics in Optical Coherence Tomography: InTech; 2012. p. 3±20.
20. Peters IT, Stegehuis PL, Peek R, Boer FL, van Zwet EW, Eggermont J, et al. Non-invasive detection of metastases and follicle density in ovarian tissue using full-field optical coherence tomography. Clin Cancer Res. 2016.
21. Assayag O, Antoine M, Sigal-Zafrani B, Riben M, Harms F, Burcheri A, et al. Large field, high resolution full-field optical coherence tomography: a pre-clinical study of human breast tissue and cancer assessment. Technology in cancer research & treatment. 2014; 13(5):455±68. Epub 2013/09/05.
22. Binding J, Ben Arous J, Leger JF, Gigan S, Boccara C, Bourdieu L. Brain refractive index measured in vivo with high-NA defocus-corrected full-field OCT and consequences for two-photon microscopy. Opt Express. 2011; 19(6):4833±47. https://doi.org/10.1364/OE.19.004833 PMID: 21445119
23. Grieve K, Palazzo L, Dalimier E, Vielh P, Fabre M. A feasibility study of full-field optical coherence tomography for rapid evaluation of EUS-guided microbiopsy specimens. Gastrointest Endosc. 2015; 81 (2):342±50. https://doi.org/10.1016/j.gie.2014.06.037 PMID: 25262102
24. Federa F. Code for proper secondary use of human tissue in the Netherlands 2002. http://www.federa.org/codes-conduct.
25. Dubois A, Grieve K, Moneron G, Lecaque R, Vabre L, Boccara C. Ultrahigh-resolution full-field optical coherence tomography. Applied optics. 2004; 43(14):2874±83. Epub 2004/05/18. PMID: 15143811
26. Dubois A, Vabre L, Boccara AC, Beaurepaire E. High-resolution full-field optical coherence tomography with a Linnik microscope. Applied optics. 2002; 41(4):805±12. Epub 2002/05/08. PMID: 11993929
27. Grieve K, Dubois A, Simonutti M, Paques M, Sahel J, Le Gargasson JF, et al. In vivo anterior segment imaging in the rat eye with high speed white light full-field optical coherence tomography. Opt Express. 2005; 13(16):6286±95. PMID: 19498641

28. Landis JR, Koch GG. The measurement of observer agreement for categorical data. Biometrics. 1977; 33(1):159±74. Epub 1977/03/01. PMID: 843571

29. Hruban RH, Fukushima N. Pancreatic adenocarcinoma: update on the surgical pathology of carcinomas of ductal origin and PanINs. Modern pathology: an official journal of the United States and Canadian Academy of Pathology, Inc. 2007; 20 Suppl 1:S61±70. Epub 2007/05/09.

30. Apelian C, Harms F, Thouvenin O, Boccara AC. Dynamic full field optical coherence tomography: subcellular metabolic contrast revealed in tissues by interferometric signals temporal analysis. Biomed Opt Express. 2016; 7(4):1511±24. https://doi.org/10.1364/BOE.7.001511 PMID: 27446672

31. Erkan M, Hausmann S, Michalski CW, Fingerle AA, Dobritz M, Kleeff J, et al. The role of stroma in pancreatic cancer: diagnostic and therapeutic implications. Nature reviews Gastroenterology & hepatology.2012; 9(8):454±67. Epub 2012/06/20.

32. Drifka CR, Tod J, Loeffler AG, Liu Y, Thomas GJ, Eliceiri KW, et al. Periductal stromal collagen topology of pancreatic ductal adenocarcinoma differs from that of normal and chronic pancreatitis. Modern pathology: an official journal of the United States and Canadian Academy of Pathology, Inc. 2015; 28(11):1470±80.

33. Bredfeldt JS, Liu Y, Conklin MW, Keely PJ, Mackie TR, Eliceiri KW. Automated quantification of aligned collagen for human breast carcinoma prognosis. Journal of pathology informatics. 2014; 5(1):28. https://doi.org/10.4103/2153-3539.139707 PMID: 25250186

34. Lopater J, Colin P, Beuvon F, Sibony M, Dalimier E, Cornud F, et al. Real-time cancer diagnosis during prostate biopsy: ex vivo evaluation of full-field optical coherence tomography (FFOCT) imaging on biopsy cores. World journal of urology. 2015. Epub 2015/06/24.

35. Yang C, Ricco R, Sisk A, Duc A, Sibony M, Beuvon F, et al. High efficiency for prostate biopsy qualification with full-field OCT after training. Proc SPIE 9689, Photonic Therapeutics and Diagnostics XII.2016;96891J.

36. Hu W, Zhao G, Wang C, Zhang J, Fu L. Nonlinear optical microscopy for histology of fresh normal and cancerous pancreatic tissues. PLoS One. 2012; 7(5):e37962. https://doi.org/10.1371/journal.pone.0037962 PMID: 22655087

37. Eberlin LS, Margulis K, Planell-Mendez I, Zare RN, Tibshirani R, Longacre TA, et al. Pancreatic Cancer Surgical Resection Margins: Molecular Assessment by Mass Spectrometry Imaging. PLoS Med. 2016;13(8):e1002108. https://doi.org/10.1371/journal.pmed.1002108 PMID: 27575375

38. Hutteman M, van der Vorst JR, Mieog JS, Bonsing BA, Hartgrink HH, Kuppen PJ, et al. Near-infrared fluorescence imaging in patients undergoing pancreaticoduodenectomy. Eur Surg Res. 2011; 47(2):90±7. https://doi.org/10.1159/000329411 PMID: 21720166

39. van der Vorst JR, Vahrmeijer AL, Hutteman M, Bosse T, Smit VT, van de Velde CJ, et al. Near-infrared fluorescence imaging of a solitary fibrous tumor of the pancreas using methylene blue. World J Gastrointest Surg. 2012; 4(7):180±4. https://doi.org/10.4240/wjgs.v4.i7.180 PMID: 22905287

40. de Geus SW, Boogerd LS, Swijnenburg RJ, Mieog JS, Tummers WS, Prevoo HA, et al. Selecting Tumor-Specific Molecular Targets in Pancreatic Adenocarcinoma: Paving the Way for Image-Guided Pancreatic Surgery. Mol Imaging Biol. 2016.

41. Erickson-Bhatt SJ, Nolan RM, Shemonski ND, Adie SG, Putney J, Darga D, et al. Real-time Imaging of the Resection Bed Using a Handheld Probe to Reduce Incidence of Microscopic Positive

Margins in Cancer Surgery. Cancer research. 2015; 75(18):3706±12. Epub 2015/09/17. https://doi.org/10.1158/0008-5472.CAN-15-0464 PMID: 26374464

42. Tao YK, Shen D, Sheikine Y, Ahsen OO, Wang HH, Schmolze DB, et al. Assessment of breast pathologiesusing nonlinear microscopy. Proc Natl Acad Sci U S A. 2014; 111(43):15304±9. https://doi.org/10.1073/pnas.1416955111 PMID: 25313045
43. Benoit a la Guillaume E, Martins F, Boccara C, Harms F. High-resolution handheld rigid endomicroscope based on full-field optical coherence tomography. Journal of biomedical optics. 2016; 21(2):26005. https://doi.org/10.1117/1.JBO.21.2.026005 PMID: 26857471
44. LLTech. www.lltechimaging.com 2016 [16-09-2016].

5

Toward optical guidance during endoscopic ultrasound-guided fine needle aspirations of pancreatic masses using single fiber reflectance spectroscopy: a feasibility study

Paulien L. Stegehuis*, Leonora S. F. Boogerd*, Akin Inderson, Roeland A. Veenendaal, P. van Gerven, Bert A. Bonsing, J. Sven Mieog, Arjen Amelink, Maud Veselic, Hans Morreau, Cornelis J. H. van de Velde, Boudewijn P. F. Lelieveldt, Jouke Dijkstra, Dominic J. Robinson , Alexander L. Vahrmeijer

*Both authors contributed equally to the study and share first authorship.

Journal of Biomedical Optics 22(2), 024001 (February 2017)

ABSTRACT

Endoscopic ultrasound-guided fine needle aspirations (EUS-FNA) of pancreatic masses suffer from sample errors and low-negative predictive values. Fiber-optic spectroscopy in the visible to near-infrared wavelength spectrum can noninvasively extract physiological parameters from tissue and has the potential to guide the sampling process and reduce sample errors. We assessed the feasibility of single fiber (SF) reflectance spectroscopy measurements during EUS-FNA of pancreatic masses and its ability to distinguish benign from malignant pancreatic tissue. A single optical fiber was placed inside a 19-gauge biopsy needle during EUS-FNA and at least three reflectance measurements were taken prior to FNA. Spectroscopy measurements did not cause any related adverse events and prolonged procedure time with ⍰5 min. An accurate correlation between spectroscopy measurements and cytology could be made in nine patients (three benign and six malignant). The oxygen saturation and bilirubin concentration were significantly higher in benign tissue compared with malignant tissue (55% versus 21%, p=0.038; 166 µmol/L versus 17 µmol/L, p=0.039, respectively). To conclude, incorporation of SF spectroscopy during EUS-FNA was feasible, safe, and relatively quick to perform. The optical properties of benign and malignant pancreatic tissue are different, implying that SF spectroscopy can potentially guide the FNA sampling.

INTRODUCTION

Endoscopic ultrasound-guided fine needle aspiration (EUS-FNA) is increasingly used as a diagnostic modality to obtain a cytological diagnosis of suspect pancreatic masses. Surgery is currently the only treatment option for long-term survival in patients with pancreatic cancer. However, only a small minority of patients is eligible for surgery due to late detection, and it is often performed without pathological confirmation of the diagnosis.[1] Neoadjuvant therapy gains more interest to downsize the primary tumor and treat micrometastatic disease prior to resection.[2] Consequently, the need for a pathological confirmation is warranted before the start of chemotherapy.[3,4] Although EUS-FNA is a relatively safe procedure with a high specificity, it suffers from a high sampling error, resulting in a low-negative predictive value, and the need for an on-site cytopathologist.[5,6] Moreover, the accuracy of EUS-FNA drops considerably when (peritumoral) pancreatitis is present, which most frequently occurs.[7]

Several techniques have been investigated to enhance the diagnostic accuracy including contrast enhancement, confocal laser endomicroscopy, and optical coherence tomography.[8–12] However, these techniques involve administration of a contrast agent or extensive training to interpret the images. Fiber-optic spectroscopy is a relatively novel diagnostic modality that already showed its feasibility in a pilot study to characterize pancreatic tissue and to differentiate between normal and malignant tissue during surgery.[13] Although these first *in vivo* results were encouraging, the size of the probe was not compatible with the small lumen of an FNA needle. No studies have yet been performed to assess the feasibility of fiber-optic spectroscopy during pancreatic EUS-FNA procedures.

Reflectance spectroscopy provides information about tissue absorption and scattering parameters. Light in the visible to near-infrared wavelength range is dominantly absorbed in the biological tissue by oxygenated and deoxygenated hemoglobin. Light is also absorbed by other chromophores, such as bilirubin and beta-carotene, depending on the tissue type. Single fiber (SF) reflectance spectroscopy uses only an SF to both emit the outgoing and capture the returning light. The advantage of using an SF is its ability to fit through an endoscopic biopsy needle, which, combined with its small sampling depth of approximately the fiber diameter,[14] allows measurements at the exact biopsy location. Using *a priori* knowledge of the absorption spectra of the chromophores, a previously developed, described, and validated mathematical model can be used to extract and quantify physiological information, such as tissue oxygenation and blood volume fraction, from the obtained spectra.[14,15] In previous studies, our group has shown the potential of SF reflectance spectroscopy in detecting abnormal mediastinal lymph nodes during EUS-FNA procedures in patients with a clinical suspicion of lung cancer.[16]

In this study, we evaluated the feasibility of the incorporation of SF reflectance spectroscopy into pancreatic EUS-FNA procedures. The primary objectives were to assess the safety—assessed through adverse events—and ease of use—assessed through additional time taken—during the procedure. Moreover, we measured wavelength-dependent optical characteristics of pancreatic masses and assessed whether we could distinguish benign from malignant pancreatic tissue based on their optical properties.

MATERIAL AND METHODS

Patients

This trial was approved by the Medical Ethics Committee of the Leiden University Medical Center and was performed in accordance with the ethical standards of the Helsinki Declaration of 1975. Sixteen patients planned to undergo an EUS-FNA procedure to obtain a diagnosis of a pancreatic mass were included. All patients provided informed consent and were anonymized. The EUS-FNA procedures were performed by two experienced gastroenterologists.

Measurement Setup

The experimental setup used in this study has been described in detail previously[15] and is shown in Fig.1. In short, the setup utilizes a single optical fiber connected to a quadfurcated optical fiber. Two arms are connected; one arm leading from a halogen light source HL-2000-FHSA (Ocean Optics, the Netherlands), and a second arm leading to a spectrophotometer SD-2000 (Ocean Optics, the Netherlands) to measure white light reflectance. A calibration procedure was performed to account for internal reflections, variability in lamp-specific output and in fiber-specific transmission properties.[17]

Sterilized single-use fibers (Leoni, Germany) had a core diameter of 300 µm, an outer diameter of 700 µm, an SMA905 connector, a distal polished fiber for wide-angle beam, a numerical aperture of 0.22, and a length of 3 m (±0.2 m). The sampling depth depends on the optical properties but is typically similar to the core diameter of the fiber.[14]

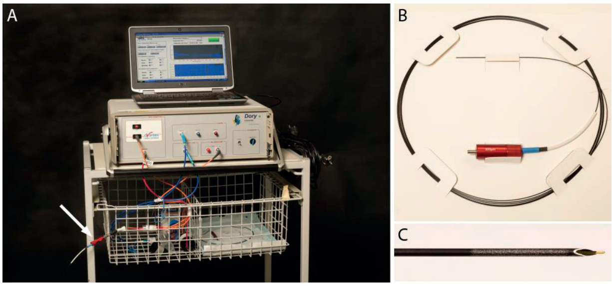

Figure 1. Measurement setup. (a) The measurement device with laptop. The white arrow points at the connection point for the fiber. (b) The optical fiber, with a length of 3 m and an outer diameter of 700 µm. (c) Incorporation of the optical fiber into 19-G puncture needle.

Examination Procedure

The procedure was performed using a curved linear array echo endoscope EG-327UK Slim, EG-3870UTK (Pentax Europe GmbH, Hamburg, Germany) or EG-580UT (Fujifilm, Tokyo, Japan). Patients were positioned in left lateral decubitus position under conscious sedation (50 mcg fentanyl, 3 mg midazolam) or deep sedation (propofol, administered by nurse anesthesist). After visualization of the pancreatic mass, the stylet of a 19-G biopsy needle (ECHO-19; Cook Medical, Bloomington) was replaced by a sterilized single-use fiber, after which the needle was placed into the endoscope channel and advanced into the target lesion. The fiber was extended a few millimeters through the biopsy needle to enable measurements without influence of the needle shaft. At least three reflectance measurements were acquired before FNA. At the time of these measurements, systemic blood saturation was measured using a pulse oximeter. Individual reflectance spectroscopy measurements were averaged over 10 measurements with an integration time of 100 ms. After obtaining spectroscopy measurements, the fiber was removed and the routine procedure was continued. The cytology slides with the resulting FNA were marked to correlate spectroscopy measurements to cytology outcome. The puncture was repeated a maximum of 5 times until the on-site cytopathologist had confirmed the adequacy of the sample. Spectroscopy measurements were only taken prior to the first puncture.

Pathologic Assessment of Cytology

The aspirated material was examined on-site to judge the sample for its adequacy. Punction material was expelled from the needle onto the glass slides and gently smeared. Air-dried smears were stained using the rapid RAL staining (RAL Diagnostics, Martical, France). Remaining material was formalin fixed; this material gives opportunity of performing ancillary techniques. After the procedure, all slides were examined by an experienced cytopathologist.

Mathematical Analysis of Spectra

SF reflectance spectra were analyzed using an analytical model to describe the wavelength-dependent optical properties to extract physiological and morphological information from the sampled tissue. Previously, a similar model has been described for analysis of other tissues.[18] Attenuation due to absorption within the tissue is modeled using a modified Beer–Lambert law and is a function of both the tissue absorption coefficient (μ_a) and the SF photon path length. The reflectance amplitude, as well as the SF photon path length, depend on the scattering properties of the tissue, with a dependence on the reduced scattering coefficient (μ'_s) and on the angular distribution of scattering (phase function), modeled through phase function parameter $\gamma=(1-g2)/(1-g1)$ with g1 and g2 the first and second moments of the phase function, respectively. The dependence of the SF reflectance signal on phase function parameter gamma results from the overlapping source–detector areas utilized in SF measurements, for which the diffusion approximation does not hold.[19] The complete model used to fit the data is given in the following equation:

$$
\begin{aligned}
&R_{\mathrm{SF}}^{\mathrm{Model}}(\mu_a, \mu_s', \gamma, d_{\mathrm{fib}}, \mathrm{NA}, \eta_{\mathrm{medium}}) \\
&= \frac{\mathrm{NA}^2}{\eta_{\mathrm{medium}}^2}\left[1 + 0.62\gamma^2 e^{-2.3\gamma^2(\mu_s' d_{\mathrm{fib}})}\right]\left[\frac{(\mu_s' d_{\mathrm{fib}})^{0.57\gamma}}{2.3\gamma^2 + (\mu_s' d_{\mathrm{fib}})^{0.57\gamma}}\right] \\
&\times e^{-\mu_a \frac{1.05\gamma^{0.6} d_{\mathrm{fib}}}{(\mu_s' d_{\mathrm{fib}})^{0.18}[0.64+(\mu_a d_{\mathrm{fib}})^{0.64}]}}, \qquad (1)
\end{aligned}
$$

where d_{fib} is the fiber core diameter and NA is the numerical aperture of the fiber (0.3 mm and 0.22, respectively) and η_{medium} is the refractive index of the pancreatic tissue under investigation, assumed to be 1.38.[20] The reduced scattering coefficient was fitted as a power-law function,[17] $\mu'_s = a_0(\lambda/\lambda_0)^{a1}$. Gamma was assumed to be constant over the fitted wavelength range, $\gamma = a2$. Furthermore, instead of fitting γ as a free parameter, we have also fitted Eq.(1) keeping γ fixed at 1.4, 1.6, and 1.8, which is an expected range for γ in biological tissues.[21] We have verified that these different approaches for fitting the data to Eq.(1) did not result in differences in the estimated absorption coefficient of more than 6%.

Since we have not previously performed measurements on pancreatic tissue, our initial model assumed that absorption was attributable to oxygenated (HbO_2) and deoxygenated hemoglobin (Hb) confined within the local microvasculature and bilirubin according to the following equation:

$$
\mu_a^{\mathrm{tissue}} = a_3 C_v [a_4 \mu_a^{\mathrm{HbO_2}} + (1 - a_4)\mu_a^{\mathrm{Hb}}] + \mu_a^{\mathrm{BIL}} a_5, \qquad (2)
$$

where a_3 is the blood volume fraction, a_4 is the microvascular hemoglobin oxygen saturation, C_v is a factor that accounts for the effect of discrete blood vessels on the absorption coefficient and enables an estimation of the average blood vessel diameter $d_v = a_6$, a_5 is the bilirubin concentration, μ_a^{BIL} is the specific absorption coefficient of bilirubin, and μ_a^{HbO2} and μ_a^{Hb} are the specific absorption coefficients of oxy- and deoxyhemoglobin, respectively.

A Levenberg–Marquardt algorithm was used to estimate the parameter values a1−a6 by minimizing the chi-squared metric between measured reflectance data and model predictions. Confidence intervals on parameter estimates were calculated from the square root of the diagonal of the covariance matrix.[22] Parameter values were averaged over repeated measurements, weighted by the confidence interval of individual spectral fits, and reported with the associated weighted standard deviation.

In this study, spectra that showed evidence of a blood pool within the detection volume were identified by blood volume fraction $a_3 > 40\%$ and excluded from the analysis as was done previously.[18]

Statistical Analysis

The statistical analysis and the graphs were generated using SPSS statistical software (Version 22.0, Chicago, Illinois). Statistical analysis was carried out using the Kruskal–Wallis test on the parameters obtained from the fit. This test replaces data by rank and is considered adequate when data does not show a Gaussian distribution.[23]

RESULTS

Patients

Sixteen patients undergoing a pancreatic EUS-guided FNA were included. In three patients no FNA, and thus no spectroscopic measurements, was performed, due to lack of visualization of the pancreatic mass. In the remaining thirteen patients, we were able to perform spectroscopic measurements. Of these, two patients were excluded due to a poor connection between the sterile measurement fiber and the quadfurcated optical fiber causing erroneous spectra and two patients were excluded due to lack of precise correlation with pathology (Fig.2). In the latter two patients, the yield of the 19-G needle biopsies was inadequate and instead, good quality FNAs were acquired with the more flexible and smaller 25-G needle. One of the excluded patients was a patient with a pancreatic neuroendocrine tumor; the final puncture, obtained with a 25-G needle, was performed at the same location where the 19-G needle was positioned and spectroscopy measurements were taken. Because the cytology correlation might not be completely reliable, we described SF reflectance spectra of this patient separately. Characteristics of these patients are listed in Table 1.

Cytological results could be correlated with spectroscopy measurements in the remaining nine patients, with cytological diagnosis of the spectroscopy-related FNA sample showing malignancy in six patients and benign disease in three patients. Two out of the three patients whose cytology showed a benign anomaly were at the end of their treatment plan suspect to suffer from pancreatic cancer. Patient #7 diagnosed with fibrotic inflammation, underwent pancreatic surgery based on clinical symptoms and preoperative images. The surgery was aborted due to hemodynamic instability. Patient #16, diagnosed with fibrosis, showed an increase in tumor volume and thickened lymph nodes on a CT-scan, performed one month after the EUS-FNA. Both patients died within four months after the EUS-FNA procedure. Although no final histopathological diagnosis could be made, this was most likely due to a pancreatic adenocarcinoma.

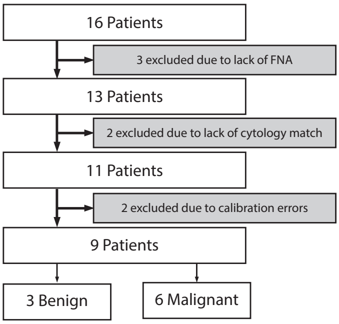

Figure 2. Inclusion scheme of patients

Table 1 Patient characteristics. Patients 3, 6, and 12 were included, but no biopsy was taken so no SF reflectance spectroscopy measurements were performed.

Patient	Gender	Age	Site	Diameter tumor (mm)	Cytology
1	M	71	Corpus	30	Malignant: mucinous cystic tumor
2	M	74	Corpus/tail	80	Malignant: adenocarcinoma
4[a]	F	47	Head	NS	Neuroendocrine tumor
5	F	54	Head	NS	Malignant: metastasis adenocarcinoma ovary
7	F	70	Whole pancreas	50	Benign: fibrotic inflammation
8 [a]	M	47	Head	25	Malignant: highly dysplastic cells
9 [a]	M	63	Head and tail	NS	Benign: autoimmune pancreatitis
10	F	55	Tail	40	Malignant: adenocarcinoma
11	M	60	Corpus	33	Benign: autoimmune pancreatitis
13	F	60	Processus uncinatus	NS	Malignant: adenocarcinoma
14	F	53	Processus uncinatus	24	Malignant: adenocarcinoma
15 [a]	M	69	Head/ Processus uncinatus	44	Benign: fibrosis
16	M	74	Head	20	Benign: fibrosis

Single Fiber Reflectance Spectra

No adverse events related to the spectroscopy measurements were observed. Additional endoscopy time related to the spectroscopic measurements was approximately five minutes.

Representative SF reflectance spectra from measurements taken at a benign and malignant spot (patients #16 and #2) are displayed in Fig. 3. In Table 2, the measured values of blood oxygen saturation, blood volume, and bilirubin concentration are displayed. Pancreatic tissue does not show much hemoglobin absorption features in the spectra, which are typically visible as “dips” in reflectance between 500 and 600 nm. The lack of strong absorption features in the spectra is reflected in the fitted values for the blood volume, which are low for both benign and malignant sites (1.1% and 2.2%, respectively; Fig. 4). The microvascular saturation is significantly higher at benign sites than malignant sites (55% versus 21%, p = 0.038; Fig. 4). Bilirubin absorbs light mostly between 400 and 500 nm, with a peak around 450 nm. Benign sites were associated with significantly higher bilirubin content than malignant sites (166 μmol/L versus 17 μmol/L, $p = 0.039$; Fig. 4). The amplitude and slope of the reduced scattering coefficient (a_0 and a_1, respectively) were not significantly different between benign and malignant tissue. Measurements of the patient who suffered from a pancreatic neuroendocrine tumor showed a blood level of 33.6% ± 1.6% with a saturation of 86.2% ± 12.1%.

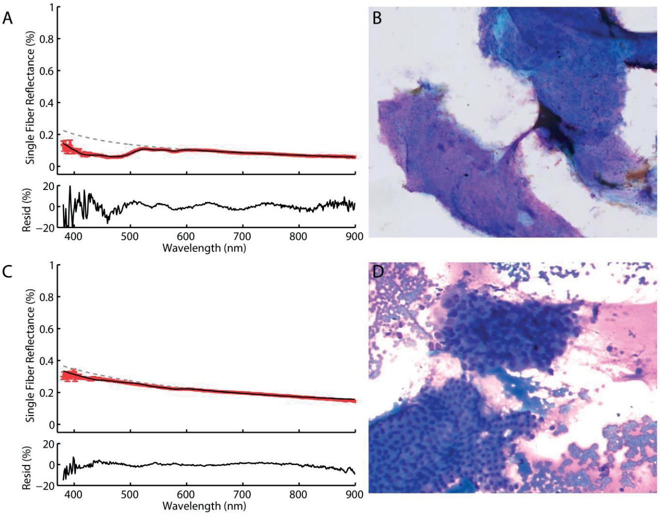

Figure 3. Fitted spectra with corresponding cytology. (a) and (c) Spectra of a benign and malignant sample, respectively. The red line in the spectra indicates the actual measurements, and the black line shows the fit. The dotted line represents the expected spectra if no absorbers would be present in the sample. The residual—difference between measurement and fit—is shown below the spectra. (b) The corresponding cytology sample of (a): the lower left corner shows fibrosis (low magnification). (d) The corresponding cytology samples of (c): pancreatic ductal adenocarcinoma cells are shown in the middle (high magnification).

Table 2. Extracted means and standard deviations of blood volume, saturation, and bilirubin per patient.

Patient	Cytology	Blood volume (%)		Saturation (%)		Bilirubin (μmol/L)	
	result	Mean	SD	Mean	SD	Mean	SD
1	Malignant	0.7	0.3	29.4	45.9	2.5	1.8
2	Malignant	0.9	0.5	20.9	5.0	7.2	2.7
5	Malignant	1.4	0.4	0.0	7.8	11.8	3.1
7	Benign	0.3	0.1	48.3	30.3	39.2	18.1
10	Malignant	5.1	4.1	0.0	50.0	3.4	2.4
11	Benign	0.8	0.3	50.8	42.4	338.8	239.7
13	Malignant	3.1	1.9	49.6	4.2	26.6	0.5
14	Malignant	1.8	0.2	28.7	8.9	48.6	3.2
16	Benign	2.0	1.5	64.9	18.0	119.3	95.1

SD: Standard deviation

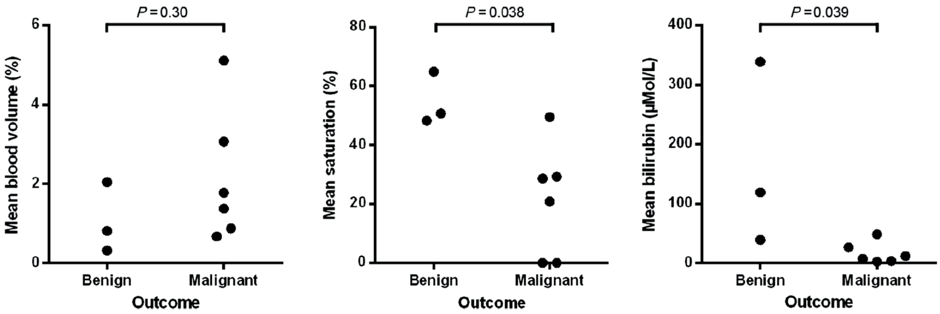

Figure 4. Difference in blood volume, saturation, and bilirubin concentration between cytological confirmed benign and malignant sites. Every individual patient is indicated by a dot. P-values are displayed above the scatterplots.

DISCUSSION

In this study, we showed that the incorporation of SF spectroscopic measurements during EUS-FNA procedures of the pancreas is feasible and safe. Because the fiber can be preloaded, measurements can be performed relatively easily and quickly. In our pilot study, the endoscopic procedure was prolonged with �5 min on average, which could be shortened after gaining more experience. No adverse events related to the spectroscopy measurements were observed, making it a safe procedure. Moreover, we demonstrated that optical properties, extracted from the SF reflectance spectra, appeared to be different between benign and malignant pancreatic aspirations. Therefore, incorporation of fiber-optic spectroscopy could potentially help to guide the FNA procedures and thereby reduce the sampling error and increase its negative predictive value without significantly affecting the complexity or time of the procedure.

Although EUS-FNA currently has a high specificity, it suffers from a low-negative predictive value implying that a negative result cannot be relied upon.[24] This is also confirmed by the current study: cytology results of three out of the nine patients showed a benign condition. Two out of these three patients (fibrotic inflammation and fibrosis), eventually turned out to have a malignancy by follow-up treatment or diagnosis and the FNA results thus represent sample errors. As more attention is given to neoadjuvant chemotherapy,[2] which requires a pathological diagnosis, it is highly important to reduce the sampling error and increase the negative predictive value of EUS-FNA procedures.

Pancreatic ductal adenocarcinoma is a hypovascular and a hypoxic tumor.[25–27] This is confirmed in this study, since both the benign and malignant sites showed very low levels of mean blood volume (1.1% and 2.1%, respectively). These results are supported by a study of Erkan et al.,[25] in which the microvascular density was determined: normal pancreas showed a five times higher microvascular density than fibrotic areas of chronic pancreatitis, and four times higher than pancreatic ductal adenocarcinoma. Interestingly, one of the patients in which we took measurements (but lacked good cytological correlation) was diagnosed with a pancreatic neuroendocrine tumor, which are known to be hypervascular.[28] That measurement indeed showed a far higher blood level of 33.6% ± 1.6% with a saturation of 86.2% ± 12.1%.

The saturation of hemoglobin is a marker for the level of hypoxia.[29,30] We found significant lower mean saturation values in malignant areas compared to benign areas (21% and 55%, respectively), despite high overall arterial oxygen saturation values (>97%). This is in agreement with results of Koong et al.,[31] who intraoperatively measured pancreatic tissue oxygenation (using an Eppendorf pO2 histograph) and found significant tumor hypoxia, whereas normal tissue showed normal oxygenation. In another study, patients undergoing pancreatic surgery received pimonidazole—a hypoxia tracer that can be detected in tissue by immunohistochemistry—and showed that more hypoxia was present in the epithelial regions than in the stromal regions of the tumor (although there was a high intra- and intertumoral heterogeneity) and the absence of hypoxia in adjacent normal pancreatic tissue.[32] Additionally, Lohse et al.[33] measured hypoxia in the stromal compartment of patient-derived pancreatic xenografts. They concluded that the levels of hypoxia in the tumor-associated stroma were generally lower when compared to the tumor compartment. These studies support our results. Although we did not measure normal tissue, we did—most likely—measure stromal areas of pancreatic adenocarcinoma in the two patients who suffered from fibrosis and inflammation (according to the cytology results obtained through EUS-FNA). These patients indeed showed a higher saturation and thus lower hypoxia levels than epithelial pancreatic adenocarcinoma regions. Furthermore, hypoxia is a known biomarker and potential therapeutic target in pancreatic cancer[34–36] and *in vivo* saturation measurements could provide interesting additional information to increase our understanding of the role of hypoxia before and during neoadjuvant treatment.

The levels of bilirubin found in this study are within the range that could be expected for this patient cohort. However, we cannot directly correlate the bilirubin concentration measured in pancreatic tissue to the bilirubin concentration measured in plasma, since we are only optically sampling a small amount of tissue with a low blood volume fraction. Moreover, we did not prospectively measure serum bilirubin levels prior to EUS-FNA. This would be a valuable addition as bilirubin levels can change quickly in cholestatic patients. It is interesting to speculate on the reason for our observation of lower bilirubin levels in malignant tissue compared to benign tissue. This may be a consequence of the (isolated) tumor microenvironment characterized by low blood volume, combined with the reduced availability of heme in rapidly proliferating tumor cells[37] and the possible degradation of bilirubin, known to be a strong antioxidant[38] in tumor cells under oxidative and (inflammatory) stress.

One other clinical study described *in vivo* spectroscopy measurements in human pancreatic tissue.[13] It was concluded that a difference between normal and malignant tissue could be observed in collected reflectance at wavelengths around 470 and 650 nm, measured with a multifiber probe. However, the diameter of the multifiber probe is too large to fit through an endoscopic biopsy needle, making a translation to standard EUS-FNA procedures difficult.

In this study, reflectance spectra were analyzed using a fit algorithm [Eq. (1)] that incorporates the fact that the reflectance amplitude and the SF photon path length depend on the scattering properties of the tissue, with a dependence on not just the reduced scattering coefficient (μ'_s) but also on the angular distribution of scattering (phase function) modeled through phase function parameter γ. We note that the use of Eq. (1) to fit the data no longer requires the use of the method described in a study by Kanick et al.[39] In that study, instead of explicitly expressing the γ dependence of the collected SF reflectance, a set of empirical constants was used that minimized the error between the true and fitted SF path lengths. However, since the combined effects of μ_a, μ'_s, and γ on SF reflectance are now fully captured by Eq. (1), such an approach based on empirical constants is no longer necessary for accurate estimation of μ_a. The fact that the different methods of fitting to Eq. (1) did not result in differences in the estimated μ_a of more than 6% indicates that this new method of fitting is robust.

A limitation of our study is the overall small sample size and small number of benign tissue measurements. However, our primary aim was to study the feasibility of incorporating SF reflectance spectroscopy measurements into the EUS-FNA procedure. Although it is encouraging that even with a small sample size differences in optical properties are observed, a larger (multicenter) study, including a wide variety of pancreatic lesions, is needed to fully exploit the potential of SF spectroscopy to guide the EUS-FNA sampling. In this study, we grouped pancreatitis with fibrous tumor parts (that were regarded as benign by the cytologist) together. More samples would enable us to also study the differences between these individual groups. The group of Hoffman et al., developed an orthotopic human tumor graft mouse model in which different fluorescent proteins were tested to image tumor progression.[40,41] This approach could be interesting as it allows visual distinction between pancreatic cancer cells and the surrounding stroma.[42,43] In addition, several clinical trials are currently investigating the safety and feasibility of intraoperative near-infrared fluorescence imaging using pancreatic cancer-specific contrast agents (NTR5673, NCT02736578).

The fiber used in this study fits through a 19-G needle, but is too thick for the more flexible 22-G needle, which is currently the preferred size at our gastroenterology department. Furthermore, we noticed that the SMA-connector of the sterile fiber was not always easily connected to the quadfurcated fiber, causing erroneous reflections in two patients. Future studies will, therefore, be performed with a smaller diameter fiber that fits through a 22-G needle, and with tighter tolerance requirements on the SMA-connector to secure a tight connection between fiber and measurement setup.

Real-time feedback is crucial to guide the gastroenterologist to epithelial tumor regions during the procedure, and, since our spectral fitting method is sufficiently fast (<1s), this is feasible. Finally, to make the incorporation of SF reflectance spectroscopy into the FNA procedure even more simple, the small SF could potentially be integrated into the shaft of the biopsy needle, as already shown in a 15-G needle.[44] Integration of the optic fiber would allow direct visualization of the difference between benign and malignant tissue per patient, as we currently do not have data on intrapatient differences.

In conclusion, incorporation of SF reflectance spectroscopy measurements in EUS-FNA procedures of the pancreas is feasible and safe. Moreover, the optical properties differ between benign and malignant tissue sites, which could be used for real-time guidance of FNA sampling to reduce the sample error of these procedures and improve overall performance.

Disclosures

The authors declare no conflicts of interest, financial or otherwise.

Acknowledgments

Work at the LUMC was funded by the European Union Seventh Framework Program FP7-ICT-2011-8under Grant Agreement No. 318729 (CAReIOCA project), the Dutch Cancer Society under Grant Agreement No. UL2010-4732, and the Bas Mulder Award (Grant No. UL2015-7665) from the Alpe d'HuZes Foundation/Dutch Cancer Society.

REFERENCES

1. E. P. Tamm et al., “Imaging of pancreatic adenocarcinoma: update on staging/resectability,” Radiol. Clin. North Am., 50 (3), 407 –428 (2012).
2. S. Tsai and D. B. Evans, “Therapeutic advances in localized pancreatic cancer,” J. Am. Med. Assoc. Surg., 74 (11), 2913 –2921 (2016).
3. J.-M. Dumonceau et al., “Indications, results, and clinical impact of endoscopic ultrasound (EUS)-guided sampling in gastroenterology: European Society of Gastrointestinal Endoscopy (ESGE) clinical guideline,” Endoscopy, 43 (10), 897 –912 (2011).
4. M. Hidalgo, “Pancreatic cancer,” N. Engl. J. Med., 362 (17), 1605 –1617 (2010).
5. M. A. Eloubeidi et al., “Yield of endoscopic ultrasound-guided fine-needle aspiration biopsy in patients with suspected pancreatic carcinoma,” Cancer, 99 (5), 285 –292 (2003).
6. J. Chen et al., “Diagnostic accuracy of endoscopic ultrasound-guided fine-needle aspiration for solid pancreatic lesion: a systematic review,” J. Cancer Res. Clin. Oncol., 138 (9), 1433 –1441 (2012).
7. A. Fritscher-Ravens et al., “Comparison of endoscopic ultrasound-guided fine needle aspiration for focal pancreatic lesions in patients with normal parenchyma and chronic pancreatitis,” Am. J. Gastroenterol., 97 (11), 2768 –2775 (2002).
8. K. Kamata et al., “New techniques of endoscopic ultrasonography for the pancreaticobiliary diseases,” Ultrasonography, 35 (3), 169 –179 (2016).
9. K. Grieve et al., “A feasibility study of full-field optical coherence tomography for rapid evaluation of EUS-guided microbiopsy specimens,” Gastrointest. Endosc., 81 (2), 342 –350 (2015).
10. V. J. A. Konda et al., “First assessment of needle-based confocal laser endomicroscopy during EUS-FNA procedures of the pancreas (with videos),” Gastrointest. Endosc., 74 (5), 1049 –1060 (2011).
11. R. Regunathan et al., “Feasibility and preliminary accuracy of high-resolution imaging of the liver and pancreas using FNA compatible microendoscopy (with video),” Gastrointest. Endosc., 76 (2), 293 –300 (2012).
12. N. K. Reddy et al., “Contrast-enhanced endoscopic ultrasonography,” World J. Gastroenterol., 17 (1), 42 –48 (2011).
13. W. R. Lloyd et al., “In vivo optical spectroscopy for improved detection of pancreatic adenocarcinoma: a feasibility study,” Biomed. Opt. Express, 5 (1), 9 –15 (2014).
14. S. C. Kanick et al., “Monte Carlo analysis of single fiber reflectance spectroscopy: photon path length and sampling depth,” Phys. Med. Biol., 54 (22), 6991 –7008 (2009).
15. S. C. Kanick, H. J. C. M. Sterenborg and A. Amelink, “Empirical model of the photon path length for a single fiber reflectance spectroscopy device,” Opt. Express, 17 (2), 860 –871 (2009).
16. S. C. Kanick et al., “Characterization of mediastinal lymph node physiology in vivo by optical spectroscopy during endoscopic ultrasound-guided fine needle aspiration,” J. Thorac. Oncol., 5 (7),
17. F. van Leeuwen-van Zaane et al., “In vivo quantification of the scattering properties of tissue using multi-diameter single fiber reflectance spectroscopy,” Biomed. Opt. Express, 4 (5), 696 –708 (2013).
18. S. C. Kanick et al., “Integration of single-fiber reflectance spectroscopy into ultrasound-guided endoscopic lung cancer staging of mediastinal lymph nodes,” J. Biomed. Opt., 15 (1), 017004 (2010).

19. U. A. Gamm et al., "Quantification of the reduced scattering coefficient and phase-function-dependent parameter γ of turbid media using multidiameter single fiber reflectance spectroscopy: experimental validation," Opt. Lett., 37 (11), 1838 –1840 (2012).
20. S. Y. Lee et al., "Characterizing human pancreatic cancer precursor using quantitative tissue optical spectroscopy," Biomed. Opt. Express, 4 (12), 2828 (2013).
21. U. A. Gamm et al., "Measurement of tissue scattering properties using multi-diameter single fiber reflectance spectroscopy: in silico sensitivity analysis," Biomed. Opt. Express, 2 (11), 3150 –3166 (2011).
22. A. Amelink, D. J. Robinson and H. J. C. M. Sterenborg, "Confidence intervals on fit parameters derived from optical reflectance spectroscopy measurements," J. Biomed. Opt., 13 (5), 054044 (2008).
23. W. H. Kruskal and W. A. Wallis, "Use of ranks in one-criterion variance analysis," Source J. Am. Stat. Assoc., 47 (260), 583 –621 (1952).
24. F. Miura et al., "Diagnosis of pancreatic cancer," HPB (Oxford), 8 337 –342 (2006).
25. M. Erkan et al., "Cancer-stellate cell interactions perpetuate the hypoxia-fibrosis cycle in pancreatic ductal adenocarcinoma," Neoplasia, 11 (5), 497 –508 (2009).
26. C. Feig et al., "The pancreas cancer microenvironment," Clin. Cancer Res., 18 (16), 4266 –4276 (2012).
27. D. Lytras et al., "Microvessel landscape assessment in pancreatic ductal adenocarcinoma: unclear value of targeting endoglin (CD105) as prognostic factor of clinical outcome," Pancreas, 44 (1), 87 –92 (2015).
28. L. R. McKenna and B. H. Edil, "Update on pancreatic neuroendocrine tumors," Gland Surg, 3 (4), 258 –275 (2014).
29. J. Im and N. Rajaram, "Optical molecular imaging and spectroscopy of oxygenation and metabolism in tumors," IEEE J. Sel. Top. Quantum Electron., 22 (3), 78 –87 (2016).
30. M. Gerling et al., "Real-time assessment of tissue hypoxia in vivo with combined photoacoustics and high-frequency ultrasound," Theranostics, 4 (6), 604 –613 (2014).
31. A. C. Koong et al., "Pancreatic tumors show high levels of hypoxia," Int. J. Radiat. Oncol. Biol. Phys., 48 (4), 919 –922 (2000).
32. N. C. Dhani et al., "Analysis of the intra- and intertumoral heterogeneity of hypoxia in pancreatic cancer patients receiving the nitroimidazole tracer pimonidazole," Br. J. Cancer, 113 (6), 864 –871 (2015).
33. I. Lohse et al., "Assessment of hypoxia in the stroma of patient-derived pancreatic tumor xenografts," Cancers (Basel), 6 (1), 459 –471 (2014).
34. M. Erkan, M. Kurtoglu and J. Kleeff, "The role of hypoxia in pancreatic cancer: a potential therapeutic target?," Expert Rev. Gastroenterol. Hepatol., 10 (3), 301 –316 (2015).
35. Q. Chang et al., "Hypoxia predicts aggressive growth and spontaneous metastasis formation from orthotopically grown primary xenografts of human pancreatic cancer," Cancer Res., 71 (8), 3110 –3120 (2011).
36. W. R. Wilson and M. P. Hay, "Targeting hypoxia in cancer therapy," Nat. Rev. Cancer, 11 (6), 393 –410 (2011).

37. M. M. Alam et al., “A holistic view of cancer bioenergetics: mitochondrial function and respiration play fundamental roles in the development and progression of diverse tumors,” Clin. Transl. Med., 5 (3), 1 –14 (2016).

38. T. Jansen and A. Daiber, “Direct antioxidant properties of bilirubin and biliverdin. Is there a role for biliverdin reductase?,” Front. Pharmacol., 3 (30), 1 –10 (2012).

39. S. C. Kanick et al., “Method to quantitate absorption coefficients from single fiber reflectance spectra without knowledge of the scattering properties,” Opt. Lett., 36 (15), 2791 –2793 (2011).

40. M. Yang et al., “Dual-color fluorescence imaging distinguishes tumor cells from induced host angiogenic vessels and stromal cells,” Proc. Natl. Acad. Sci. U. S. A., 100 (24), 14259 –14262 (2011).

41. A. Suetsugu et al., “Multi-color palette of fluorescent proteins for imaging the tumor microenvironment of orthotopic tumorgraft mouse models of clinical pancreatic cancer specimens,” J. Cell. Biochem., 113 (7), 2290 –2295 (2012).

42. H. J. M. Handgraaf et al., “Current and future intraoperative imaging strategies to increase radical resection rates in pancreatic cancer surgery,” Biomed Res. Int., 2014 1 –8 (2014).

43. M. C. Boonstra et al., “Preclinical evaluation of a novel CEA-targeting near-infrared fluorescent tracer delineating colorectal and pancreatic tumors,” Int. J. Cancer, 137 (8), 1910 –1920 (2015).

44. J. W. Spliethoff et al., “Real-time in vivo tissue characterization with diffuse reflectance spectroscopy during transthoracic lung biopsy: a clinical feasibility study,” Clin. Cancer Res., 22 (2), 357 –365 (2016).

6

Fluorescence lifetime measurements for the recognition of tumor tissue: Comparing two clinically relevant cRGD-based near-infrared fluorescent agents

Paulien L. Stegehuis*, Martin C. Boonstra*, Karien de Rooij, Harald A.R. Homulle, Claudio Bruschini, Edoardo Charbon, Riccardo Sinisi, Hendrica A.J.M. Prevoo, Cock J.H. van de Velde, Boudewijn P.F. Lelieveldt, Alexander L. Vahrmeijer, Martijn van de Giessen, Jouke Dijkstra

*These two authors contributed equally.

Submitted to Molecular Imaging

ABSTRACT.

Fluorescence lifetime measurements may increase the specificity of intraoperative tumor identification. We measured in vitro and in vivo fluorescence lifetimes of two cRGD-based fluorophores – cRGD-ICG and cRGD-ZW800-1 – and investigated the ability to differentiate between their bound, tumor-specific, and unbound, aspecific, state.

In vitro, U87MG glioblastoma cells were incubated with different concentrations of either cRGD-ICG or cRGD-ZW800-1. In vivo, mice with subcutaneous U87MG tumors were administered with either cRGD-ICG or cRGD-ZW800-1 along with a subcutaneous bolus in the tail. A time-domain single photon avalanche diode based system was used to measure fluorescence lifetimes of tumor and tail at 1-, and 24 hours.

In vitro, for cRGD-ICG no significant differences in lifetimes were measured between the concentrations, or between the different groups. In vivo, lifetimes of cRGD-ICG at the tumor were longer than those at the tail after both 1 hour ($p<0.001$), and 24 hours ($p=0.022$). Lifetimes of cRGD-ZW800-1 at the tumor were shorter than those at the tail after both 1 hour ($p<0.001$), and 24 hours ($p=0.036$). Histology confirmed bound and unbound states of the fluorescent dyes.

The results showed that bound fluorescence probe exhibits a different lifetime compared to unbound fluorescence probe, indicating that in vivo lifetime measurements could potentially be used in addition to fluorescence guided surgery, to improve its specificity.

INTRODUCTION

Next to techniques that provide anatomical information such as MRI and CT, pre-operative imaging techniques, such as single-photon emission computed tomography (SPECT) and positron emission tomography (PET), increasingly aid oncologic surgeons in staging patients and planning their surgical procedure.[1–3] Besides the incidental use of ultrasound, during surgery surgeons mainly rely on their hands and eyes with which it is challenging to discriminate between malignant and healthy tissues, potentially leading to inadequate resection margins and damage to (complex) vital structures.[4,5]

The recently introduced tumor-specific fluorescence-guided surgery (FGS) technique – using fluorescence intensity of exogenous contrast agents – can aid surgeons in identifying malignant tissues during surgery.[4] Similar to SPECT/PET, FGS is based on molecular imaging, combining fluorophores with tumor-specific ligands. However, FGS shows higher spatial resolutions and provides real-time intraoperative feedback. The sensitivity and specificity of FGS depend on the tumor-to-background ratio (TBR) of the fluorescent signal: the ratio between the amount of signal in the tumor and that in the background. For sufficient TBRs, there always is a wash-out time of unbound agents, which can be as high as 72 hours for antibodies, and down to hours for smaller peptide-based agents.[6,7] Generally, a TBR of two or higher is considered sufficient.[8] Due to the inability of FGS to differentiate between specific (target bound) and aspecific (not target bound) tracer signals, and the lag-time between injection and optimal imaging time-points, it can be difficult to recognize clear margins and acquire adequate signals. No adjustment of the injected dose of the agent can be performed during operation. For example, when during surgery signals are too weak, no secondary dose can be administered as the optimal time-point is often hours till days later. Therefore, complementary techniques must be developed that can be used in parallel to FGS and deal with these demerits, like the analysis of fluorescence lifetime.

The lifetime of a fluorophore – the time a molecule resides in the excited state before returning to the ground state through fluorescence emission – is influenced by its physiological environment.[9,10] In contrast to fluorescence intensity imaging, fluorescence lifetime imaging is generally insensitive to differences in concentration.[11,12] To measure fluorescence lifetimes, which are typically in the order of nanoseconds, dedicated equipment is necessary.

Several preclinical studies reported successful in vivo lifetime imaging of exogenous contrast agents for different applications.[13–16] Biffi et al., conjugated rituximab (a monoclonal antibody) with Cy5.5 targeting CD20 antigen that is expressed on B-cell lymphoid malignancies. They reported higher lifetimes at the tumor than at the surrounding normal tissue.[13] Ardeshipour and colleagues used fluorescence lifetime to study the efficacy of HER2 targeted therapy for breast cancer. They conjugated Alexafluor 750 to a HER2-specific Affibody and found that this probe showed a lower lifetime when bound to HER2 compared with unbound probe.[14] Nakajima et al., showed the feasibility of detecting peritoneal ovarian tumors with Rhodamine green using lifetime measurements, and observed that fluorescence intensity can be compromised by blood contamination whereas these lesions could still be detected by their fluorescence lifetimes.[16] Although providing promising results, none of these used fluorophores that can be translated into human studies.

Clinically, the fluorophores methylene blue (MB) and indocyanine green (ICG) laid the foundation for FGS and are at present the only two near infrared (NIR) fluorescent dyes approved for off-label clinical use.[17] More dedicated NIR fluorescent dyes, such as IRDye800CW and ZW800-1, were subsequently developed and are currently manufactured following cGMP guidelines and showed no toxicity or adverse events in animal toxicity studies and first-in-human studies.[18–22]

Conjugating these NIR fluorescent dyes to tumor recognizing vehicles enables highly distinctive imaging. The amino acid sequence arginine-glycine-aspartate (RGD) is such a vehicle: it is a natural occurring peptide that recognizes at least 8 different integrins ($\alpha_v\beta_1$, $\alpha_V\beta_3$, $\alpha_v\beta_5$, $\alpha_v\beta_6$, $\alpha_v\beta_8$, $\alpha_5\beta_1$, $\alpha_8\beta_1$ and $\alpha_{IIb}\beta_3$) that are upregulated in various tumor types, and overexpressed on angiogenic endothelial cells within the tumor stroma.[23,24] The high affinity for either the cancer cells, the supporting endothelial cells, or both cell types together makes RGD a powerful vehicle whereby the majority of tumors can be targeted.[25,26] Clinically, RGD-based PET and SPECT tracers are already extensively investigated in Phase I and Phase II imaging studies, revealing their imaging potential, while the peptide (named cilengitide) was investigated for its anticancer effects in a Phase III trial in high doses without significant side effects.[27–30] We used the modified cyclic versions of peptide RGD (cRGDfK, hereafter referred to as cRGD), as they possess enhanced clearance, stability and binding affinity. Moreover, they can easily be conjugated to various labels without losing their affinity.[31]

In this study, we measured the fluorescence lifetime of two clinically relevant tumor-specific fluorophores developed for FGS using an enhanced camera set-up.[32] We examined and compared the fluorescence lifetime properties of cRGD-ICG and cRGD-ZW800-1 when bound or unbound to $\alpha_v\beta_3$ during in vitro and in vivo experiments and showed that fluorescence lifetime measurements can be a complementary technique utilized next to FGS, ultimately broadening the use of NIR fluorescence imaging applications in the clinic.

MATERIALS AND METHODS

Tumor-specific agents

cRGD-ICG was produced at the Ecole Polytechnique Fédérale de Lausanne,[33] while the cRGD-ZW800-1 variant was produced in the peptide lab of the Leiden University Medical Center, following published protocols.[19] Both agents were lyophilized and stored at -80 degrees Celsius and diluted when needed.

Devices used

Fluorescence lifetimes were acquired with an experimental compact measurement setup, named FluoCam (Fig. 1), that measures photon arrival times using an existing single photon synchronous detection (SPSD) system enhanced with a precise gating scheme.[32] The complete time-domain setup consists of a single-photon sensitive sensor array, a picosecond pulsed laser for sample illumination, optical components to illuminate the sample and deliver its fluorescent signal to the sensor, as well as signal processing and lifetime calculation approaches, allowing the complete fine reconstruction of the integral of a fluorescence signal.

The single-photon sensitive sensor itself consists of an array of 60×48 single photon avalanche diodes (SPADs).[32] Each SPAD is contained in a pixel, which employs two 8-bit counters to record the number of photons detected by the corresponding SPAD in a given time window, which can be scanned in time steps as fine as 12.3 ps using programmable delay lines. The need for more complex in-pixel electronics entails, in the technology used for FluoCam, a reduced fill-factor (0.8%). The overall absolute sensitivity is however sufficient to derive sub-nanosecond lifetimes in good agreement with literature, as well as to carry out measurements in vivo.

The single-photon timing resolution per pixel is of the order of 100 ps, whereas the overall system Instrument Response Function has a Full-Width-Half-Maximum (FWHM) of 290 ps. The illumination source is a picosecond diode laser (A.L.S. GmbH, Berlin, Germany) with a wavelength of 790 nm that emits 70 ps FWHM pulses to the sample at a pulse repetition rate of 100 MHz with an average power of 1.7 mW. The laser trigger signal, delayed through the delaylines, is used as a switch between the counters of the SPAD sensor. Two filters (excitation 775/50 nm (center/bandwidth), emission 845/50 nm) and a dichroic mirror (810 nm) deliver excitation illumination to the sample and emission light to the sensor (filter set No41030, Chroma Technology Corporation, Bellows Falls, USA).

Fluorescence intensity images were acquired with a PEARL imaging system (LI-COR Biosciences, Lincoln, Nebraska, USA) in two spectral bands, which are optimized for two LI-COR dyes: the IRDye 680RD (absorbance max 675 nm, emission max 696nm) and the IRDye800CW (absorbance max 779 nm, emission max 795 nm). The PEARL is equipped with two excitation lasers at 685 nm and 785 nm. Exposure times are by default optimized during imaging. The excitation and emission characteristics of ICG and ZW800-1 are sufficiently overlapping with IRDye800CW for sensitive fluorescence intensity imaging.

Finally, high resolution fluorescence intensity scanning was performed using the 800 nm channel (excitation at 785 nm) of the Odyssey scanner (LI-COR Biosciences, Lincoln, Nebraska, USA). This imager is designed for the assessment of in vitro well-plate experiments and the imaging of small, excised tissue samples.

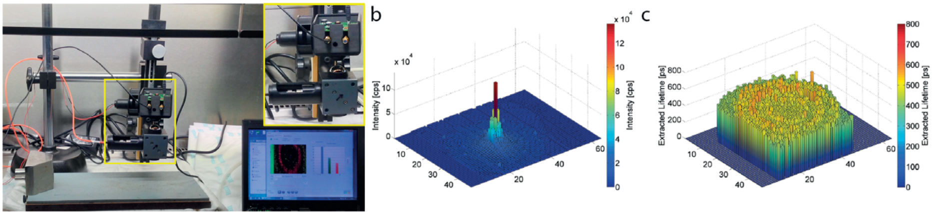

Figure 1. a) The FluoCam measurement setup, used for all experiments. The inset shows the single-photon sensitive sensor array. Just below that, are the optical components that guide the light to illuminate the sample and deliver its fluorescent signal to the sensor. The samples are placed underneath the optical components. The cooling system and laser are not shown. b) The fluorescence intensity of all pixels of a sample of unwashed cells of 50 µM cRGD-ICG. c) The corresponding fluorescence lifetime in picoseconds.

Fluorescence lifetime analysis

For a specific fluorophore and biochemical environment, the time between the absorption of a photon from a laser pulse and the emission of a photon from the fluorescent molecule approximates an exponential stochastic distribution. The rate at which the fluorescence intensity I decreases over time t is parameterized by the fluorescence lifetime τ as $I(t) = I_0e^{-t/\tau}$, with I_0 the peak intensity.[8]

In the time-domain acquisition with the FluoCam experimental setup, two counters (C0 and C2) count arriving photons in adjacent intervals that cover the exponential distribution. The proportion of C0 to the total number of arriving photons (C0+C2) depends on the lifetime τ and the user-defined delay d. By scanning d over time, a histogram that describes the integrated exponential distribution is obtained. From this histogram the lifetime τ is estimated. Measuring with two counters allows for normalization in the case of a non-constant fluorescence intensity over time, e.g. due to fluorescence photobleaching. Apart from this normalization corrections are performed to compensate for non-linearities in the delay lines. For more details the reader is referred to [32-34]. In this paper the processing of the raw signals is slightly changed compared with [32] as described below, to reduce the sensitivity to noise. The SPADs in the sensor were tested to have a photodetection probability of 2% at 835 nm.

In this work d is increased in steps of 24.6 ps, which is an optimization between accurate lifetimes and shorter measurement times. In pilot experiments we determined the corresponding acquisition range to be sufficient to cover the exponential distributions of the fluorescent probes used. This resulted in a total measurement time of almost 3 minutes. The initial delay is adapted on a pixel-to-pixel basis. At each delay, an exposure time of 1 second is used.

In the data analysis, the measurements from “hot” (very noisy) and “dead” pixels are discarded. Overall lifetime of the sample is determined from the lifetimes extracted in each individual pixel: an intensity-weighted Gaussian fit is applied to the corresponding distribution. To reduce the noise, the intensity threshold was set at 3 kcps. However, if a sample could not meet that condition, the 100 pixels with the highest photon count were taken.

Cell line

The U87MG glioblastoma cell line was used for the in vitro and in vivo experiments. This cell line was previously shown to express the highest number of $\alpha_v\beta_3$ integrins per cell.[19] The U87MG cell line was cultured in DMEM (Gibco, Carlsbad, CA, USA) supplemented with 10% fetal calf serum (FCS; Greiner Bio-One, Kremsmünster, Austria), 100U/ml penicillin and 100 U/ml streptomycin (Gibco) in a humidified incubator with 5% CO2 at 37 degrees Celsius.

In vitro cell based plate assay

U87MG cells were seeded in black 96-well plates (Greiner Bio-One) at a density of 9.4 x 10^4 cells/cm^2 and allowed to attach overnight. The following day the cells were incubated with a dose range of cRGD-ICG or cRGD-ZW800-1 in DMEM containing 5% bovine serum albumin (BSA) or with 50µM probe without BSA in duplicate. After 1 h half of the wells were washed with DMEM/5% BSA or DMEM alone (without BSA), while in the other half the probe solution remained present during the measurements to create washed and unwashed samples. The probe solutions and the incubated wells were measured 3 times using the FluoCam setup. Subsequently, the solutions and incubated wells were scanned using the Odyssey Infrared Imaging System at a resolution of 42 µm, medium quality and intensity of L1.0-L2.0 (solutions) or L1.0-1.0 (incubated wells). Each well was analyzed and the integrated intensity (counts/mm^2) was calculated using the Odyssey software.

In vivo measurements

Six to eight week-old a-thymic female mice (CD1-Foxn1nu, Charles River Laboratories, l'Arbresle, France) weighing 25 - 35 g, were housed in accordance with the guidelines of the Animal Welfare Committee of the Leiden University Medical Center. Autoclaved low fluorescence pellet food, normal pellet food and sterilized water were provided ad libitum. Throughout tumor inoculation and the measurement procedures, the animals were anesthetized with 4% isoflurane for induction and with 2% isoflurane for maintenance with a flow of 0.5 L/min and were placed on a heated animal bed with an integrated nose mask. All animal experiments were approved for animal health, ethics, and research by the Animal Welfare Committee of the Leiden University Medical Center. All animals received humane care and maintenance in compliance with the 'Code of Practice Use of Laboratory Animals in Cancer Research' (Inspectie W&V, July 1999).

To induce subcutaneous tumors, U87MG cells were injected at four sites on the back (1,500,000-3,000,000 cells per spot) and tumor growth was monitored using a digital caliper. When the tumors were approximately 36mm3, either 30 nM (50 µg) of cRGD-ICG (n=4 mice) or cRGD-ZW800-1 (n=4 mice) was injected intravenously. Fluorescence lifetime was measured directly (between 15-60 minutes) and at 24 hours. At both time-points two of the four tumors were measured. A control spot in the tail (to measure free floating agent) was created by a subcutaneous bolus injection of the fluorophore and measured at both time-points. After each time-point, mice were simultaneously imaged using a PEARL imaging system to evaluate fluorescence intensity. The two tumors that were measured directly were resected and quick frozen in isopentane to perform NIR fluorescence microscopy and to evaluate probe distribution. After the 24 hours measurement mice were sacrificed and the remaining tumors, were quickly frozen in isopentane for histological evaluation.

Histology

Tissues were sectioned at 10 µm, mounted with DAPI, and examined for NIR fluorescence signals using the Nikon eclipse E800 microscope (Nikon, Amsterdam, The Netherlands). Afterwards all histologic sections were stained with standard hematoxylin-eosin stain (HE) to evaluate presence of tumor cells and histology. As control, similar tumor tissue from a mouse without injection of a probe was also investigated using fluorescence microscopy and HE-staining.

Statistics

Statistical analysis was performed with SPSS software (IBM SPSS statistics version 22). Variance between groups was first assessed via one way analysis of variation (ANOVA); differences in means between two groups were assessed via the post-hoc Bonferroni test. $P<0.05$ was considered statistical significant. Data are expressed as mean ± standard deviation (SD).

RESULTS

In vitro fluorescence lifetimes

Lifetimes of cRGD-ICG dissolved with BSA either incubated at U87MG cells (washed and unwashed) or in solution remained stable and showed no significant differences between all three concentrations (10 µM, 20 µM and 50 µM), and SDs were low for the solutions and unwashed groups (4-8 ps) (Fig. 2a). In the washed group relatively large SDs (17-45 ps) were observed probably due to the low signal intensity as shown in Fig. 2c. When BSA is omitted, mean lifetimes dropped significantly for all groups ($p<0.001$). As expected, higher signal intensities are observed in the unwashed and solution groups with BSA (Fig. 2c). Fluorescence intensities when BSA is omitted are lower (means of 39.9 ± 8.3 A.U., 56.5 ± 3.9 A.U., and 6.2 ± 2.1 A.U. for washed, unwashed and solution, respectively) compared to those with BSA.

Lifetimes of cRGD-ZW800-1 dissolved with BSA either incubated at U87MG cells and unwashed or in solution did not remain stable between all three concentrations. The unwashed samples of 50 µM were significantly different from those of 10 and 20 µM ($p<0.001$ for both). The solution samples of 10 and 50 µM were also significantly different ($p<0.001$). The washed samples showed very low fluorescence intensities (Fig. 2d) and although similar lifetimes were measured as in the other samples, standard deviations of fluorescence lifetimes were much higher (between 46-129 ps compared to 3-16 ps) (Fig. 2b). Significant differences were seen between solution samples with BSA compared to without BSA ($p<0.001$) and unwashed samples with BSA compared to without BSA (p<0.001), but not for the washed samples. Fluorescence intensities when BSA is omitted were 1.3 ± 0.9 A.U., 180.4 ± 169.8 A.U., and 929.3 ± 274 A.U. for washed, unwashed and solution, respectively.

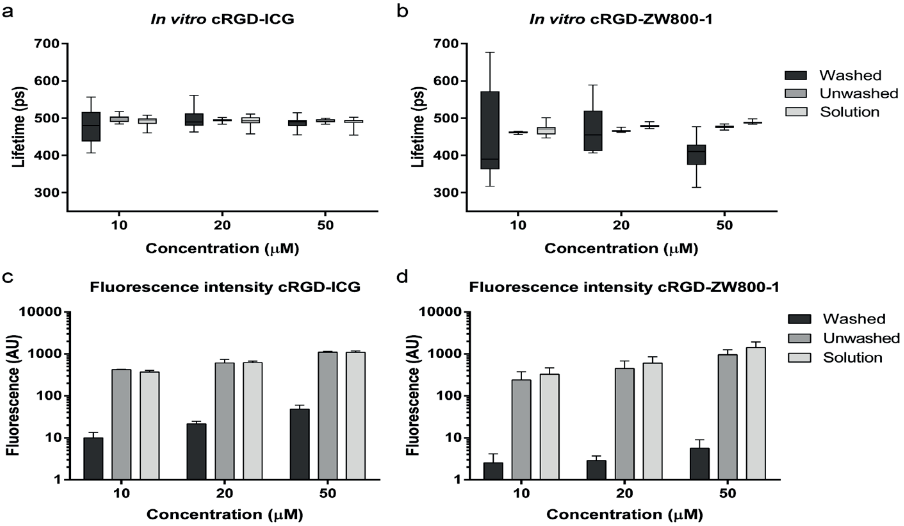

Figure 2. Lifetimes (ps) of cRGD-ICG or cRGD-ZW800-1 at U87MG cells or in solution. Boxplots show the median, first and third quartile, and minimum and maximum lifetimes (ps). a) Data from cRGD-ICG: For 10 μM mean lifetime values were 476±45, 502±8 and 494±8 for respectively washed U87MG cells, unwashed U87MG cells or tracer in solution; for 20 μM this was 497±29, 495±4 and 496±8; for 50 μM 490±17, 492±5 and 494±5; and for 50 μM without BSA 356±28, 335±33 and 200±51 (not shown in Figure). b) Mean fluorescent intensities of cRGD-ICG measured with the Odyssey for respectively washed U87MG cells, unwashed U87MG cells or tracer in solution. c) Data from cRGD-ZW800-1: For 10 μM mean lifetime values were 456±129, 461±3 and 469±16 for respectively washed U87MG cells, unwashed U87MG cells or tracer in solution; for 20 μM this was 464±61, 466±4 and 480±5; for 50 μM 407±49, 477±5 and 489±4; and for 50 μM without BSA 425±113, 424±8 and 445±3 (not shown in Figure). d) Mean fluorescent intensities for cRGD-ZW800-1.

Overall, grouping the different concentrations with BSA (10 μM, 20 μM and 50 μM) did not lead to significantly different lifetimes between these groups for cRGD-ICG. For cRGD-ZW800, the difference between washed and solutions samples was significant (p=0.023). Photobleaching was observed in the measurements, especially in the pixels with high initial intensity (Fig. 3a). However the extracted lifetimes of pixels with higher or lower intensity decreases did not differ, due to the applied correction (Fig. 3b). We did find that higher overall intensity of the sample, caused less variation in extracted lifetime. This explains the higher standard deviations and variations of the washed samples compared to those of the unwashed samples and solutions (Fig. 4).

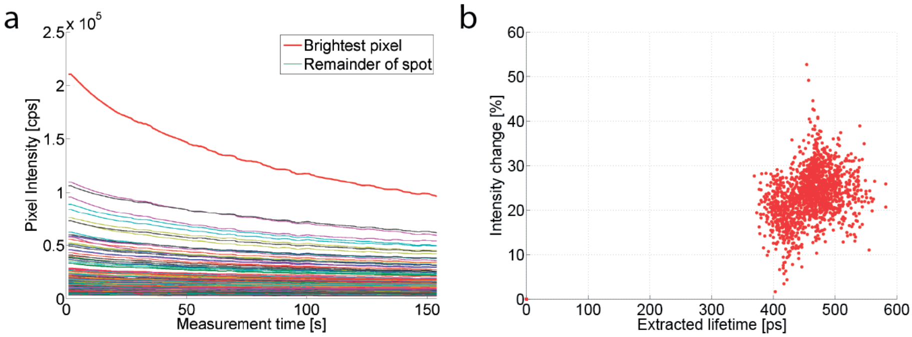

Figure 3.a) Example of the intensity change per pixel over the measurement time, measuring a sample of unwashed cells of 50 μM cRGD-ICG. b) The corresponding extracted lifetime per pixel. As the lifetime analysis corrects for photobleaching, extracted lifetimes are not influenced by the change in intensity over time.

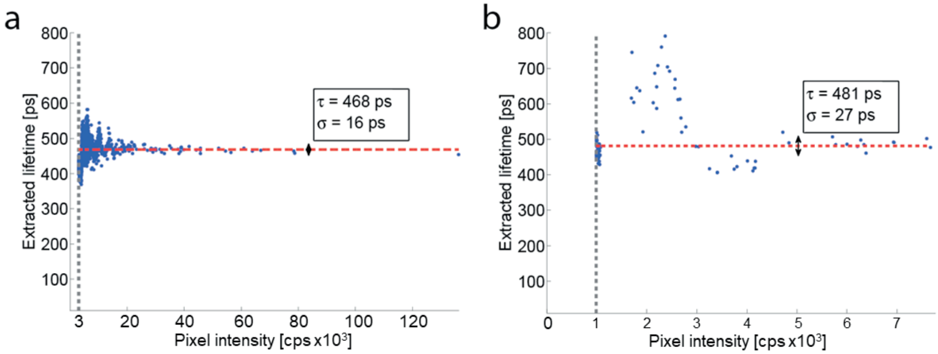

Figure 4. Two examples of the extracted lifetime versus the pixel intensity. a) Unwashed sample of 50 μM cRGD-ICG. b) Washed sample of 50 μM cRGD-ICG.

In vivo fluorescence lifetimes and intensities

After intravascular injections of 30 nM of either cRGD-ICG or cRGD-ZW800-1 fluorescence lifetimes were measured directly (1 h) and 24 h post injection in both the tumors and in the tail to measure respectively bound and unbound agent (Fig. 5). Lifetimes of cRGD-ICG at the tumor were statistically significantly higher than those at the tail at both 1 hour ($p<0.001$) and 24 hours ($p=0.022$) (Fig. 5a). Figure 5b shows representative images of optical fluorescence imaging with high signals in the liver and moderate to low signals in the tumor at 1 h (mean 1.5 ± 0.03 A.U.) and at 24 h (mean 1.6 ± 0.08 A.U.).

Interestingly, the opposite is true for lifetimes of cRGD-ZW800-1: lifetimes at the tail were statistically significantly higher than those at the tumor after both 1 hour ($p<0.001$) and 24 hours ($p=0.036$) (Fig. 5c). Using optical fluorescence imaging high signals were observed in the kidneys and tumors could be recognized with moderate mean TBRs (1.1 ± 0.06 A.U. at 1 h and 1.9 ± 0.27 A.U. at 24 h) (Fig. 5d).

Histology

Resected tumors and tails were investigated using fluorescence microscopy and HE-staining for presence and locations of the agents (Fig. 5). Both agents showed clear tumor specific signals, which were homogeneously distributed throughout the tumor and mainly located intracellularly in the cytoplasm. NIR fluorescence in the tail sections was mainly recognized in localized spots, located intercellularly and/or on endothelial cells. Generally, no homogeneous specific binding was observed in the tail sections, validating its use as control measurement point. The control tumor showed no specific signals at all.

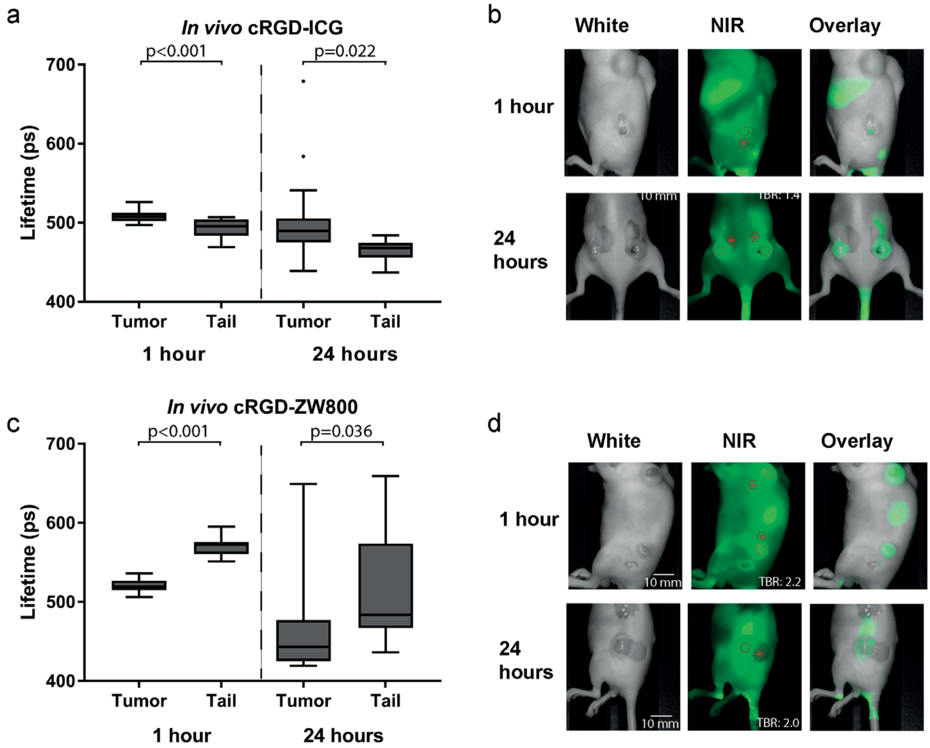

Figure 5. Lifetimes and fluorescence intensity images of mice injected with 30 nM of either cRGD-ICG or cRGD-ZW800-1. Boxplots show the median, first and third quartile, and minimum and maximum lifetimes (ps) a) Using cRGD-ICG mean lifetimes in the tumors were 508±7 and 490±31 at respectively 1 h and 24 h (both 24 measurements). In the tail those were 493±12 and 477±12 (both 12 measurements). b) Examples of fluorescence intensity images with cRGD-ICG captured at 1 h and 24 h. TBRs are from the showed image. The areas in the red circles represent the tumor and background (with asterisk) signal used to determine the TBR. c) Using cRGD-ZW800-1 mean lifetimes in the tumors were 520±8 and 457±37 at respectively 1 h and 24 h (both 24 measurements). In the tail those were 574±9 and 530±73 (both 12 measurements). d) Examples of fluorescence intensity with cRGD-ZW800-1 images captured at 1 h and 24 h.

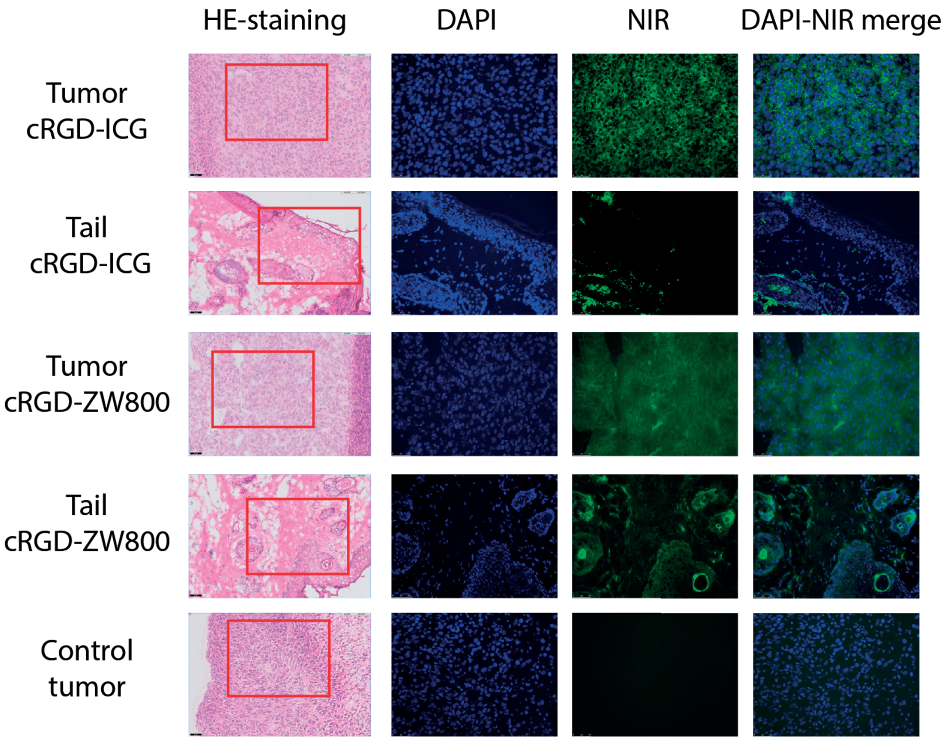

Figure 6. The left column shows HE-stained sections of either the tumors or tails. DAPI staining was used to visualize cell nuclei to find the corresponding spot at the HE slide. NIR fluorescence microscopy and the DAPI-NIR merge image shows the specific location of the fluorescent spots. Both cRGD-ICG and cRGD-ZW800 shows a homogeneous distribution throughout the tumor (bound agent), while the tail shows localized fluorescent spots mainly intercellular located (unbound agent) and sporadic at endothelial cells. No fluorescence signal is seen in the control tumor.

DISCUSSION

In this study we measured and analyzed the lifetimes of two RGD-based clinically relevant fluorophores – cRGD-ICG and cRGD-ZW800-1 – and evaluated and compared the ability to differentiate between their bound (tumor specific) and unbound (aspecific) state in vitro and in vivo. The most important result of this research was the finding that in vivo both fluorophores showed reproducible fluorescence lifetimes that were significantly different between the tumors and control regions.

Lifetimes were measured using the FluoCam time-domain SPAD-based system, which is a prototype recently developed and described by Homulle et al.[32–34] Using a SPAD array, enhanced with a gating scheme, and combined with a picosecond laser, the setup is able to both derive fluorescence intensity, as well as sub-nanosecond fluorescence lifetimes in vivo. Qualities of the system are the excellent single photon timing resolution, its compactness, low power and low voltage-operation. However, during in vitro plate assay experiments where a single cell layer of tumor cells are targeted, the system had difficulty with detecting the low signal intensities in the washed groups, resulting in large standard deviations. It is feasible to make the next generation system 50 times more sensitive (e.g. improving the fill-factor at the pixel level and increasing the photon detection probability in the NIR). This would allow a lower dose of fluorescent probe, decreased duration of measurements and lower standard deviations.

Interestingly both fluorophores reacted differently after binding: the lifetime of cRGD-ICG increased, while that of cRGD-ZW800-1 decreased; this phenomenon was significant in vivo, but not in vitro. We believe that the in vitro results for the washed samples are not representative. In the first place, our device was not sensitive enough to capture enough signal to extract reproducible lifetimes in the washed samples that suffered from low fluorescence intensities. This is supported by the more stable extracted lifetimes found at pixels with higher intensity (Fig. 4). Secondly, Ardeshipour et al.[35] already recognized the difficulty in measuring binding effects in vitro and argued that it is not only the binding causing the lifetime changes, but a combination of several processes, also involving the binding to serum albumin. For that reason we added BSA during our in vitro experiments resulting in reproducible results. Omitting BSA showed decreased fluorescence lifetimes for both fluorophores. However, the effect on cRGD-ICG was larger compared to cRGD-ZW800-1 (average difference of 156 ps vs 32 ps, respectively), which could be explained by the neutral net charge and high hydrophilicity of ZW800-1 and the net charge of -1 and hydrophobic character of ICG.[36–38] The influence of albumin on lifetime was also described in a paper by Mathejczyk et al., who attributed this effect to an increased rigidity of the fluorophore, and a reduced polarity of the fluorophore's local environment.[39] Thereby, binding to albumin prevents close contact between the fluorophore and water molecules.

In vivo results showed that mean fluorescence lifetimes for cRGD-ICG in the tumor were 508 ± 7 ps after 1 hour. This is slightly shorter (but in a comparable range) than the lifetime of ICG bound to albumin, which lies around 600 ps.[40,41] The effect that we observed – a higher lifetime in tumor compared to control tissue (mean fluorescence lifetime of 493 ± 12 ps) – was similar to that of Bloch et al., who investigated cypate – a structural analog of ICG – bound to cRGD.[15] Mean fluorescence lifetimes for cRGD-ZW800-1 were 520 ± 8 at 1 h, approximately 10% lower compared to the tail. Ardeshipour et al., also found a shorter lifetime in tumor compared to the control site.[14] They measured lifetime of AlexaFluor 750, which possesses good water solubility[42] just like ZW800-1, probably explaining the comparable mechanisms. Although both for cRGD-ICG and cRGD-ZW800-1 the differences in lifetime between tumor and control are not very large (4-10%), they are reproducible and significant.

For the in vivo measurements the glioblastoma U87MG xenograft mouse model was used as it expresses high levels of $\alpha_v\beta_{3.}$ As the RGD motive and integrins are evolutionary conserved[43], both cRGD-based agents recognized murine integrins in our U87MG xenograft mouse model, making it clinically relevant. The tail was used as a control spot for the unbound probe. Histology confirmed the difference in distribution and binding between tail and tumor for both fluorophores. It is to be expected that the differences in lifetime between tumors and closely surrounding tissue are smaller than tumors and the tail. It should be kept in mind that our goal in this study was to create the largest difference possible in binding of the fluorophore, to study whether it was feasible to find a lifetime difference at all. Future research, using a more sensitive system, could for example look at muscle tissue, where the α_v subunit is known to be absent, to get a more representative control spot.

Eventually we think that the clinical applicability of this technique will primarily be next to FGS as it can aid in differentiating between specific bound and unbound tracer. For example, when a fluorescent hotspot is shown during surgery and the treating physician is not sure whether the signal is specific, fluorescence lifetimes could be measured to evaluate if the agent is specifically bound or not. Furthermore, as fluorescence lifetime could be applied in significant shorter imaging windows than FGS, it could function as a stand-alone technique provided that sensitivity, resolution and imaging speed are significantly increased.

This study added evidence that tumor-bound fluorescent agents can be distinguished from non-tumor bound agents in vivo. In particular, we showed this for two fluorescent agents that approach clinical translation. We also showed that lifetimes measured in comparable settings and set-up can either decrease or increase when bound, depending on the fluorophore that is used. These results are an encouragement to optimize fluorescence lifetime acquisition for clinical implementation, especially by improving the overall system sensitivity.

Acknowledgements

Work at the LUMC was funded by the European Union Seventh Framework Program FP7-ICT-2011-8 under grant agreement number 318729 (CAReIOCA project). Work at EPFL was supported in part by CTI, the Swiss Federal Administration’s Commission for Technology and Innovation (Project 9801.1 PFLS-LS), by the Swiss National Foundation under Grant SNF 51NF40-144633, and by the National Centre of Competence in Research Mobile Information and Communication Systems (NCCR MICS).

Conflict of interest

The authors declare no conflict of interest. The authors have full control of all primary data and agree to allow the journal to review the data if requested.

REFERENCES

1. S. N. Histed et al., “Review of functional/anatomical imaging in oncology,” in Nuclear Medicine Communications **33**, pp. 349–361 (2012) [doi:10.1097/MNM.0b013e32834ec8a5].
2. J. V. Frangioni, “New technologies for human cancer imaging,” in Journal of Clinical Oncology **26**, pp. 4012–4021 (2008) [doi:10.1200/JCO.2007.14.3065].
3. R. Weissleder and M. J. Pittet, “Imaging in the era of molecular oncology.,” Nature **452**, 580–589 (2008) [doi:10.1038/nature06917].
4. L. Bu, B. Shen, and Z. Cheng, “Fluorescent imaging of cancerous tissues for targeted surgery.,” Adv. Drug Deliv. Rev. **76**, 21–38 (2014) [doi:10.1016/j.addr.2014.07.008].
5. B. W. Pogue et al., “Vision 20/20: Molecular-guided surgical oncology based upon tumor metabolism or immunologic phenotype: Technological pathways for point of care imaging and intervention,” Med. Phys. **43**(6), 3143–3156 (2016) [doi:10.1118/1.4951732].
6. M. C. Boonstra et al., “uPAR-targeted multimodal tracer for pre- and intraoperative imaging in cancer surgery,” Oncotarget **6**(16), 14260–14273 (2015) [doi:10.18632/oncotarget.3680].
7. Z. Cheng et al., “Near-Infrared Fluorescent RGD Peptides for Optical Imaging of Integrin $\alpha_v\beta_3$ Expression in Living Mice,” Bioconjug. Chem. **16**(6), 1433–1441 (2005) [doi:10.1021/bc0501698].
8. M. C. Boonstra et al., “Preclinical evaluation of a novel CEA-targeting near-infrared fluorescent tracer delineating colorectal and pancreatic tumors,” Int. J. Cancer **137**(8), 1910–1920 (2015) [doi:10.1002/ijc.29571].
9. M. Y. Berezin and S. Achilefu, “Fluorescence Lifetime Measurements and Biological Imaging,” Chem. Rev. **110**(5), 2641–2684 (2010) [doi:10.1021/cr900343z].
10. P. Sarder, D. Maji, and S. Achilefu, “Molecular Probes for Fluorescence Lifetime Imaging.,” Bioconjug. Chem. **26**(6), 963–974 (2015) [doi:10.1021/acs.bioconjchem.5b00167].
11. J. R. Lakowicz et al., “Fluorescence lifetime imaging,” Anal. Biochem. **202**(2), 316–330 (1992) [doi:10.1016/0003-2697(92)90112-K].
12. L. Marcu, “Fluorescence Lifetime Techniques in Medical Applications,” Ann. Biomed. Eng. **40**(2), 304–331 (2012) [doi:10.1007/s10439-011-0495-y].
13. S. Biffi et al., “In vivo biodistribution and lifetime analysis of cy5.5-conjugated rituximab in mice bearing lymphoid tumor xenograft using time-domain near-infrared optical imaging.,” Mol. Imaging **7**(6), 272–282 (2008) [doi:10.2310/7290.2008.00028].
14. Y. Ardeshirpour et al., “In Vivo Fluorescence Lifetime Imaging for Monitoring the Efficacy of the Cancer Treatment,” Clin. Cancer Res. **20**(13), 3531–3539 (2014) [doi:10.1158/1078-0432.CCR-13-1826].
15. S. Bloch et al., “Whole-body fluorescence lifetime imaging of a tumor-targeted near-infrared molecular probe in mice,” J. Biomed. Opt. **10**(5), 54003 (2005) [doi:10.1117/1.2070148].
16. T. Nakajima et al., “Fluorescence-lifetime molecular imaging can detect invisible peritoneal ovarian tumors in bloody ascites,” Cancer Sci. **105**(3), 308–314 (2014) [doi:10.1111/cas.12343].
17. S. L. Gibbs, “Near infrared fluorescence for image-guided surgery.,” Quant. Imaging Med. Surg. **2**(3), 177–187 (2012) [doi:10.3978/j.issn.2223-4292.2012.09.04].
18. H. Hyun et al., “cGMP-Compatible preparative scale synthesis of near-infrared fluorophores,” Contrast Media Mol. Imaging **7**(6), 516–524 (2012) [doi:10.1002/cmmi.1484].

19. H. S. Choi et al., “Targeted zwitterionic near-infrared fluorophores for improved optical imaging.,” Nat. Biotechnol. **31**(2), 148–153, Nature Publishing Group (2013) [doi:10.1038/nbt.2468].

20. R. Huang et al., “Integrin $\alpha_v\beta_3$-Targeted IRDye 800CW Near-Infrared Imaging of Glioblastoma,” Clin. Cancer Res. **18**(20), 5731–5740 (2012) [doi:10.1158/1078-0432.CCR-12-0374].

21. E. L. Rosenthal et al., “Safety and Tumor Specificity of Cetuximab-IRDye800 for Surgical Navigation in Head and Neck Cancer,” Clin. Cancer Res. **21**(16), 3658–3666 (2015) [doi:10.1158/1078-0432.CCR-14-3284].

22. H. J. M. Handgraaf et al., “Real-time near-infrared fluorescence imaging using cRGD-ZW800-1 for intraoperative visualization of multiple cancer types,” Oncotarget **8**(13), 21054–21066 (2017) [doi:10.18632/oncotarget.15486].

23. J. Schittenhelm et al., “Comparing the expression of integrins $\alpha_v\beta_3$, $\alpha_v\beta_5$, $\alpha_v\beta_6$, $\alpha_v\beta_8$, fibronectin and fibrinogen in human brain metastases and their corresponding primary tumors.,” Int. J. Clin. Exp. Pathol. **6**(12), 2719–2732 (2013).

24. P. C. Brooks et al., “Integrin $\alpha_v\beta_3$ antagonists promote tumor regression by inducing apoptosis of angiogenic blood vessels,” Cell **79**(7), 1157–1164 (1994) [doi:0092-8674(94)90007-8].

25. A. J. Beer et al., “Patterns of αvβ3 expression in primary and metastatic human breast cancer as shown by 18F-Galacto-RGD PET,” J. Nucl. Med. **49**(2), 255–259 (2008) [doi:10.2967/jnumed.107.045526].

26. M. C. Boonstra et al., “Stromal Targets for Fluorescent-Guided Oncologic Surgery,” Front. Oncol. **5** (2015) [doi:10.3389/fonc.2015.00254].

27. R. Stupp et al., “Cilengitide combined with standard treatment for patients with newly diagnosed glioblastoma with methylated MGMT promoter (CENTRIC EORTC 26071-22072 study): a multicentre, randomised, open-label, phase 3 trial,” Lancet Oncol. **15**(10), 1100–1108 (2014) [doi:10.1016/S1470-2045(14)70379-1].

28. A. J. Beer et al., “Positron emission tomography using [18F]Galacto-RGD identifies the level of integrin alpha(v)beta3 expression in man.,” Clin. cancer Res. **12**(13), 3942–3949 (2006) [doi:10.1158/1078-0432.CCR-06-0266].

29. E. Mena et al., “[18F]Fluciclatide in the in vivo evaluation of human melanoma and renal tumors expressing $\alpha_v\beta_3$ and $\alpha_v\beta_5$ integrins,” Eur. J. Nucl. Med. Mol. Imaging **41**(10), 1879–1888 (2014) [doi:10.1007/s00259-014-2791-x].

30. Z.-F. Su et al., “In Vitro and in Vivo Evaluation of a Technetium-99m-Labeled Cyclic RGD Peptide as a Specific Marker of $\alpha_V\beta_3$ Integrin for Tumor Imaging,” Bioconjug. Chem. **13**(3), 561–570 (2002) [doi:bc0155566].

31. M. A. Dechantsreiter et al., “N -Methylated Cyclic RGD Peptides as Highly Active and Selective αVβ3 Integrin Antagonists,” J. Med. Chem. **42**(16), 3033–3040 (1999) [doi:10.1021/jm970832g].

32. H. A. R. Homulle et al., “Compact solid-state CMOS single-photon detector array for in vivo NIR fluorescence lifetime oncology measurements,” Biomed. Opt. Express **7**(5), 1797–1814 (2016) [doi:10.1364/BOE.7.001797].

33. F. Powolny et al., “Compact imaging system with single-photon sensitivity and picosecond time resolution for fluorescence-guided surgery with lifetime imaging capability,” in Proc. SPIE Clinical and Biomedical Spectroscopy and Imaging III **8798**, V. Deckert and N. Ramanujam, Eds., p. 879806 (2013) [doi:10.1117/12.2032537].

34. F. Powolny et al., “Time-resolved imaging system for fluorescence-guided surgery with lifetime imaging capability,” in Proc. of SPIE Biophotonics: Photonic Solutions for Better Health Care IV **9129**, J. Popp et al., Eds., p. 912938 (2014) [doi:10.1117/12.2052411].

35. Y. Ardeshirpour et al., “In Vivo Fluorescence Lifetime Imaging Monitors Binding of Specific Probes to Cancer Biomarkers,” PLoS One **7**(2), I. V. Lebedeva, Ed., e31881 (2012) [doi:10.1371/journal.pone.0031881].

36. S. Ohnishi et al., “Organic alternatives to quantum dots for intraoperative near-infrared fluorescent sentinel lymph node mapping,” Mol. Imaging **4**(3), 172–181 (2005).

37. R. J. Williams et al., “Comparison of covalent and noncovalent labeling with near-infrared dyes for the high-performance liquid chromatographic determination of human serum albumin.,” Anal. Chem. **65**(5), 601–605 (1993).

38. H. S. Choi et al., “Synthesis and In Vivo Fate of Zwitterionic Near-Infrared Fluorophores,” Angew. Chemie Int. Ed. **50**(28), 6258–6263 (2011) [doi:10.1002/anie.201102459].

39. J. E. Mathejczyk et al., “Spectroscopically well-characterized RGD optical probe as a prerequisite for lifetime-gated tumor imaging,” Mol. Imaging **10**(6), 469–480 (2011) [doi:10.2310/7290.2011.00018].

40. M. Y. Berezin et al., “Ratiometric Analysis of Fluorescence Lifetime for Probing Binding Sites in Albumin with Near-Infrared Fluorescent Molecular Probes,” Photochem. Photobiol. **83**(6), 1371–1378 (2007) [doi:10.1111/j.1751-1097.2007.00173.x].

41. W. Becker and V. Shcheslavskiy, “Fluorescence lifetime imaging with near-infrared dyes,” in Proc. SPIE Multhiphoton Microscopy in the Biomedical Sciences XIII **8588**, A. Periasamy, K. König, and P. T. C. So, Eds., p. 85880R1-6 (2013) [doi:10.1117/12.2003608].

42. R. W. Sabnis, *Handbook of Fluorescent Dyes and Probes*, John Wiley & Sons, Inc, Hoboken, NJ, USA (2015) [doi:10.1002/9781119007104].

43. E. Ruoslahti, “RGD and other recognition sequences for integrins,” Annu. Rev. Cell Dev. Biol. **12**(1), 697–715 (1996) [doi:10.1146/annurev.cellbio.12.1.697].

7

Summary, discussion and future perspectives

In this thesis we studied the feasibility of three optical imaging techniques to differentiate tumor tissue from its surrounding tissue for various clinical purposes.

In **chapters 2, 3 and 4** we looked at **full field optical coherence tomography**. FF-OCT images with high-resolution (1 µm) provide *en face* images, depend on endogenous contrast and achieve an imaging depth up to 500 µm (depending on the imaged tissue). Although the resolution might be high, the contrast is based on backscattering differences without being highly tissue specific. Therefore, distinguishing intracellular structures or cytonuclear details is not possible. Also, currently FF-OCT images need to be assessed by a pathologist, which requires extensive training.

FF-OCT is a promising non-destructive technique to image and select cortical ovarian tissue strips, but requires more research to determine its potential contribution to improved pregnancy rates.

In **chapter 2** we imaged cortical ovarian tissue strips, which are used to preserve fertility in women that undergo chemotherapy and are at risk of premature ovarian failure. We found that FF-OCT did not harm the viability of the tissue and had sufficient resolution to detect both normal ovarian structures and metastases in human tissue samples. In addition, FF-OCT facilitates the selection of cortical ovarian tissue with the highest density of primordial follicles. For these reasons we believe that this application fits the FF-OCT technique very well, more so, because current techniques that are used to detect metastases in ovarian tissue are destructive, meaning that the tissue cannot be autotransplanted anymore.

Due to the small sample size we did not validate the sensitivity and specificity with which pathologists could distinguish normal from tumor tissue. Also we did not validate the minimal size of a micrometastases that could still be detected with FF-OCT. Future research should focus on these outstanding issues. Thereby, the most meaningful outcome in the field of fertility preservation is ultimately a successful pregnancy. So pregnancy rates following exposure to FF-OCT also need to be evaluated.

FF-OCT can be used for margin detection, but should be further improved with better contrast, more training and computer aided diagnosis

In **chapters 3 and 4** we studied FF-OCT in breast and pancreas aiming to eventually apply it for margin detection. The current overall accuracy we reached (79% in breast tissue and 73% in pancreatic tissue) is not yet sufficient. We believe that there are three important measures that have to be taken in order to improve diagnostic accuracy: (1) better contrast, (2) more extensive training and (3) computer aided diagnosis.

Contrast can be increased by dynamic cell imaging: a technique that enhances the cellular contrast by capturing the microscopic intracellular movements in freshly excised tissue [1]. This technique, that can capture metabolic states of cells is complementary to the existing FF-OCT technique. Thouvenin et al., were able to reveal subcellular details such as the nucleus position and size in retinal tissue [2]. Moreover, very recently, Yang et al. [3], used both FF-OCT and dynamic cell imaging to image breast and nodal tissue. Both specificity and sensitivity differentiating normal from benign tissue were higher with dynamic cell imaging compared to only FF-OCT.

More extensive training combined with computer aided diagnosis could help as well to improve reading accuracy of current images. For example, earlier studies on reading of prostate images showed a learning curve from 60% to 80% [4] within one study, which further improved to 93% in a second study [5]. Computer aided diagnosis can take advantage of the highly scattering collagen, making tumor stroma evidently visible in both breast and pancreatic tissue. This concept has been proven effectively by Bredfeldt et al., who used tumor associated collagen signatures of breast cancer tissue to automatically detect the tissue type, reaching an overall accuracy of 91.9% [6]. Focusing on collagen topography could even give additional information, as it is associated with a patients prognosis [7].

Single fiber reflectance spectroscopy has the potential to guide biopsies but requires larger sample size studies and real-time feedback

In **chapter 5** we applied single fiber reflectance spectroscopy in endoscopic ultrasound-guided fine needle aspirations (EUS-FNA) of pancreatic masses. The specifications of this technique such as a very small field of view and low penetration depth, might be very disadvantageous for most applications but fits the purpose of biopsy guidance perfectly. EUS-FNA suffers from sample errors and low-negative predictive values. However, as neoadjuvant therapy gains more interest, which requires a pathological diagnosis, it is highly important to reduce the sampling error and increase the negative predictive value of EUS-FNA procedures.

We found significant differences in blood volume, blood saturation and bilirubin levels between tumor and surrounding tissue. However, we only performed a feasibility study with a small sample size. Future studies should increase the number of patients included to validate the first results found and to increase the knowledge on the characteristics of different pancreatic tissues. Next to that, for a clinical embedding of the technique, it needs to deliver real-time feedback to the physician. Since our spectral fitting method is sufficiently fast (<1 s), this is feasible. Moreover, recently a new spectral fitting model was developed which predicts the measured reflectance substantially better than the model used in this study [8]. This can be used in the next study with larger sample size.

Fluorescence lifetime could potentially be used in parallel to fluorescence guided surgery, but needs large technical improvements

In **chapter 6** we looked at fluorescent lifetime measurements (FLM) and investigated the ability to differentiate between their bound, tumor-specific, and unbound, aspecific, state. Where in the first four chapters we looked at endogenous contrast – contrast of the tissue itself – this technique exploits exogenous contrast agents. It is also the technique that is the least developed for clinical applications out of the three techniques studied in this thesis.

Fluorescence lifetime measurements can be used in parallel to fluorescence guided surgery (FGS) and overcome some of the demerits of FGS such as the high wash-out time of unbound agents and a low overall tumor-to-background ratio. In our study, we found small differences between bound and unbound tracer (4-10%), but they were reproducible and significant. Due to the low sensitivity of the system, in-vitro measurements lacked clear signals which resulted in high standard deviations for the lower concentrations. The sensitivity of the system clearly needs work. We were only able to show small differences between tumor tissue and a spot in the tail (unbound), but it will be harder to show differences between tumor tissue and close by tissue that is normal. If sensitivity can be drastically improved and differences between tumor and surrounding tissue are found, further steps can be taken to think about ease of use, way of (real-time) feedback and integration into FGS.

Optical imaging techniques studied in this thesis could be of additional clinical value, but translation to clinical practice is far off

In this thesis we studied the feasibility of three optical imaging techniques to differentiate tumor tissue from its surrounding tissue for various clinical purposes. Our main research question hereby was:

Is it feasible to differentiate tumor tissue from surrounding tissue using optical imaging techniques; and which technique can be of added value for clinicians in which clinical situation?

We concluded that both full field optical coherence tomography and single fiber reflectance spectroscopy could either with help of pathologists or by signal analysis differentiate tumor tissue from its surrounding tissue. Although FF-OCT is especially useful in imaging ovarian tissue, endogenous contrast in breast and pancreatic tissue is not yet sufficient. Using fluorescence lifetime we were able to demonstrate differences between tracer bound to tumor cells and tracer not bound to tumor cells. However, this technique is still much more experimental and with the current technique, differentiating tumor tissue from its directly surrounding tissue is not yet possible.

Next to the techniques studied in this thesis, many other optical techniques are studied to image tissue physiology and pathology, such as Raman-spectroscopy, hyperspectral and short-wave infrared imaging. Although a lot of research is performed on all these techniques, only few will translate to the clinic: the gap from feasibility to standard of practice is massive. In this thesis we only studied the feasibility, but did not perform larger scale multi-center studies. Naturally this is an important requirement to bring research one step closer to clinical adoption. Furthermore, the added technique should match current clinical workflow as closely as possible.

For instance converting an FF-OCT image with dynamic cell imaging into a H&E staining image(e.g. by using a Generative Adversarial Network, deep learning technique), will be better recognized by pathologists. Just like a fiber incorporated into a biopsy needle to immediately measure the spectral properties of the pancreatic tissue, will be much easier to use for a gastroenterologist.

REFERENCES

1. Apelian C, Gastaud C, Boccara AC (2017) Extracting relevant information for cancer diagnosis from dynamic full field OCT through image processing and learning. In: Fujimoto JG, Izatt JA, Tuchin V V. (eds) Academic Radiology. p 100531H
2. Thouvenin O, Boccara C, Fink M, et al (2017) Cell motility as contrast agent in retinal explant imaging with full-field optical coherence tomography. Investig Ophthalmol Vis Sci. doi: 10.1167/iovs.17-22375
3. Yang H, Zhang S, Liu P, et al (2020) Use of high-resolution full-field optical coherence tomography and dynamic cell imaging for rapid intraoperative diagnosis during breast cancer surgery. Cancer 126:3847–3856 . doi: 10.1002/cncr.32838
4. Lopater J, Colin P, Beuvon F, et al (2016) Real-time cancer diagnosis during prostate biopsy: ex vivo evaluation of full-field optical coherence tomography (FFOCT) imaging on biopsy cores. World J Urol. doi: 10.1007/s00345-015-1620-6
5. Yang C, Ricco R, Sisk A, et al (2016) High efficiency for prostate biopsy qualification with full-field OCT after training. Photonic Ther. Diagnostics XII
6. Bredfeldt J, Liu Y, Conklin M, et al (2014) Automated quantification of aligned collagen for human breast carcinoma prognosis. J Pathol Inform. doi: 10.4103/2153-3539.139707
7. Dekker TJA, Charehbili A, Smit VTHBM, et al (2015) Disorganised stroma determined on pre-treatment breast cancer biopsies is associated with poor response to neoadjuvant chemotherapy: Results from the NEOZOTAC trial. Mol Oncol. doi: 10.1016/j.molonc.2015.02.001
8. Post AL, Sterenborg HJCM, Woltjer FG, et al (2020) Subdiffuse scattering model for single fiber reflectance spectroscopy. J Biomed Opt. doi: 10.1117/1.jbo.25.1.015001

SAMENVATTING

Beeldvorming speelt een cruciale rol in de oncologie. Het wordt gebruikt om de diagnose te stellen, biopten te begeleiden, het effect van behandeling te monitoren, chirurgische ingrepen te plannen en het verloop van de ziekte te voorspellen. CT, MRI, röntgenfoto´s en echografie zijn voorbeelden van beeldvormende technieken die veel gebruikt worden, voornamelijk voor anatomische informatie. De meer recent geïntroduceerde positronemissietomografie (PET) en *single photon emission computed tomography* (SPECT) scans, geven voornamelijk functionele informatie. Verbeteringen van deze technieken hebben geleid tot meer precieze, snellere en minder invasieve beeldvorming. Helaas komen al deze beeldvormende technieken met hun eigen beperkingen met betrekking tot resolutie, sensitiviteit en de mate van contrast, waardoor ze niet voor alle toepassingen geschikt zijn. Bovendien zijn ze, afgezien van Röntgen en echografie, relatief duur en is real time imaging beperkt. Daarom wordt er veel onderzoek gedaan naar optische beeldvormende technieken.

Optische beeldvorming bevat een brede range van technieken die licht gebruiken in het ultraviolette spectrum (315-400 nm), het zichtbare spectrum (400-700 nm), het nabije infrarode spectrum (700-1400 nm) of in het korte golf infrarode spectrum (1400-3000 nm) om moleculaire, morfologische en functionele informatie te geven over cellen of weefsels. Enkele voorbeelden van optische technieken zijn endoscopie, nabij-infrarode fluorescentie, optische coherentie tomografie, foto-akoestische beeldvorming, Raman spectroscopie en diffuse spectroscopie. De voordelen van deze technieken zijn sterk afhankelijk van welke techniek je gebruikt voor welke toepassing, maar algemene voordelen zijn het goede contrast in zacht weefsel, hoge resolutie, niet-invasieve aard en apparatuur die relatief goedkoop en makkelijk te hanteren is. Algemene nadelen zijn de beperkte penetratiediepte en het relatief kleine gezichtsveld.

In dit proefschrift bestuderen we de haalbaarheid van drie optische beeldvormende technieken om tumorweefsel van het omliggende weefsel te herkennen, voor verschillende klinische toepassingen.

In **hoofdstuk 2 tot en met 4** bestuderen we *full-field* optische coherentie tomografie (FF-OCT) in eierstok-, borst- en alvleesklierweefsel. Optische coherentie tomografie (OCT) is vergelijkbaar met echografie, maar detecteert terugkaatsend licht in plaats van terugkaatsend geluid. De resolutie van OCT is 10-50 keer beter dan die van echografie (1-20 µm in axiale en transverse richting) en is net als echografie niet invasief en niet destructief. In plaats van de dwarsdoorsneden die met OCT worden berekend, maakt FF-OCT *en face* beelden met hoge resolutie (1 µm). Het systeem dat in dit proefschrift gebruikt is, bestaat uit een staande microscoop en een referentiearm in een Linnik interferometrische opstelling. De lichtbron is een witte halogeenlamp van 150 watt, met een centrale golflengte van 700 nm en een spectrale breedte van 125 nm. Het contrast in de beelden komt door het terugkaatsende licht van het weefsel, maar is niet heel erg weefselspecifiek. Daardoor zijn, ondanks de hoge resolutie, intracellulaire structuren of details van de celkern niet te onderscheiden. De FF-OCT beelden moeten worden beoordeeld door een patholoog, wat uitgebreide training vergt.

Uit het onderzoek, beschreven in **hoofdstuk 2**, blijkt dat het contrast en de resolutie van FF-OCT voldoende waren om uitzaaiingen in eierstokweefsel én verschillende ontwikkelingsstadia in de eicellen zichtbaar te maken. Daarnaast bleek dat het afbeelden de vitaliteit van zowel het weefsel als de eicellen niet aantast. Dit zijn belangrijke bevindingen voor een vruchtbaarheidsbesparende behandeling bij vrouwen, waarbij eierstokweefsel wordt ingevroren en weer wordt teruggeplaatst. Wanneer een patiënt direct moet starten met chemotherapie of bestraling is dit de enige behandelingsmogelijkheid waarbij de eierstokfunctie kan worden hersteld. Dit brengt echter het risico mee dat je tumorcellen herintroduceert, in het geval dat deze al naar de eierstok was uitgezaaid. Met FF-OCT zou je niet alleen kunnen controleren of er uitzaaiingen in het terug te plaatsen weefsel zitten, maar ook het weefsel kunnen selecteren met de beste kans op herstel van de eierstokfunctie. Kanttekeningen bij dit onderzoek zijn het relatief kleine aantal weefselfragmenten dat we hebben afgebeeld waardoor we niet de sensitiviteit en specificiteit waarmee de patholoog tumorweefsel kon onderscheiden in kaart gebracht hebben. Ook heeft FF-OCT een beperkte penetratiediepte van maximaal 100 µm in dit type weefsel, waardoor je niet het hele weefselfragment af kunt beelden.

In **hoofdstuk 3 en 4** hebben we het gebruik van FF-OCT in borst- en alvleesklierkanker onderzocht, om daar uiteindelijk de tumormarges mee af te beelden tijdens de operatie. De nauwkeurigheid waarmee pathologen tumor- van normaal weefsel kunnen onderscheiden op basis van de FF-OCT beelden was 79% in borstweefsel en 73% in alvleesklierweefsel. Dat is uiteraard niet genoeg voor een klinische toepassing. We denken wel dat deze nauwkeurigheid verder verhoogd kan worden door een aantal maatregelen: beter contrast, betere training van pathologen en computerondersteunde diagnose.

In **hoofdstuk 5** concluderen we dat het toevoegen van *single fiber* reflectie spectroscopiemetingen mogelijk is bij het nemen van een endoscopische echogeleide punctie (EUS-FNA) in de alvleesklier. Een nadeel van de huidige EUS-FNA procedure is de lage negatief voorspellende waarde van het onderzoek: als er geen tumorcellen worden gevonden, betekent dat niet dat ze er niet zijn. Helemaal nu neoadjuvante therapie – waarvoor een pathologische diagnose nodig is – steeds meer belangstelling krijgt, is het belangrijk om op de goede plek een punctie te nemen. Specificaties van *single fiber* reflectie spectroscopie zijn onder andere een klein gezichtsveld en een beperkte penetratiediepte, wat voor het nemen van puncties zeer geschikt is. De metingen worden genomen door een enkele fiber, die door een punctienaald past.

Met spectroscopiemetingen toonden we significante verschillen aan in bloedvolume, bloedsaturatie en bilirubinegehalte tussen tumorweefsel en omliggend weefsel. Deze metingen kunnen de gastro-enteroloog helpen bij het vinden van een goede plaats om een punctie te nemen. In deze studie hebben we echter maar 16 patiënten geïncludeerd. Verder onderzoek, met meer patiënten is nodig om deze eerste resultaten te valideren. Daarnaast hebben we in deze studie de metingen achteraf geanalyseerd. Voor klinische toepasbaarheid heeft de arts real-time feedback nodig. Dit is gelukkig al wel mogelijk met de huidige fittingmethode, maar meer data is nodig om te herkennen wat tumorweefsel en wat omliggend weefsel is.

In **hoofdstuk 6** zagen we dat we met *fluorescence lifetime* metingen een onderscheid konden maken tussen gebonden – tumor-specifiek – en ongebonden fluorescent contrastmiddel. Waar we in de hoofdstukken hiervoor keken naar het endogene contrast van weefsel, gebruikt deze techniek exogeen contrastmiddel. Deze techniek kan gebruikt worden als aanvulling op fluorescentie-geleide chirurgie. In deze studie vonden we kleine verschillen (4-10%) in de fluorescente levensduur (een eigenschap van het contrastmiddel die afhangt van de omgeving) van contrastmiddel dat gebonden was aan de tumor en contrastmiddel dat ongebonden was. Hoewel de verschillen klein waren, waren ze wel significant en reproduceerbaar. Echter, door de lage sensitiviteit van het meetsysteem, was het signaal van de in-vitro-metingen zeer zwak wat resulteerde in grote variaties bij lage concentraties. Daarnaast zagen we alleen verschil bij in-vivo metingen tussen contrastmiddel in de staart (geheel ongebonden) en contrastmiddel in de tumor (geheel gebonden). De verschillen tussen tumorweefsel en omliggend weefsel, in een meer realistisch scenario, zullen moelijker zijn om aan te tonen. Daarvoor moet eerst de sensitiviteit van het systeem drastisch verhoogd worden.

Uit de voorgaande hoofdstukken blijkt dat FF-OCT en reflectie spectroscopie potentieel kunnen helpen om tijdens een operatie of endoscopische procedure tumorweefsel te onderscheiden van het omliggende weefsel. Met *fluorescence lifetime* metingen kan dat nog niet. Verdere technische verbeteringen in gebruik, analyse en presentatie van de metingen zijn nog nodig en daarnaast grootschaliger patiëntenstudies voordat ze kunnen worden opgenomen in de bestaande klinische praktijk.

DANKWOORD

Onderzoek doe je niet alleen. Ik maak dan ook graag van deze gelegenheid gebruik om iedereen die heeft bijgedragen aan dit proefschrift te bedanken.

Ten eerste ben ik dankbaar voor iedereen die als patiënt meewerkt aan medisch onderzoek. Ik vind het elke keer bijzonder hoe gemotiveerd patiënten zijn om bij te dragen aan het verbeteren van behandelingen waar ze (vaak) zelf geen baat bij hebben.

Jouke, Alexander, Boudewijn en Cock, bedankt voor de kans die jullie mij hebben gegeven en de prettige begeleiding tijdens mijn onderzoek. Collega's van het LKEB (speciale dank aan kamergenoten van de terminaalzaal) en de oncologische chirurgie: bedankt voor de voetbaltoernooien, bbq's, gezamenlijke congresbezoeken, borrels en prettige werkdiscussies. Ook veel dank aan alle andere collega's binnen het LUMC die hebben bijgedragen, met name vanuit de afdelingen pathologie en MDL.

Niet alleen collega's binnen het LUMC, maar ook collega-onderzoekers daarbuiten hebben bijgedragen aan dit proefschrift. Met name dank aan alle partners van het CAReIOCA-project, het Erasmus MC en de TU Delft.

Ontspanning is minstens zo belangrijk als werk en daar hebben ook veel mensen aan bijgedragen. Veel dank daarvoor aan vriendinnen, vrienden, teamgenoten en familie. Papa, bedankt voor het meedenken, meelezen en het relativeren. Evert, bedankt voor alles!

CURRICULUM VITAE

Paulien Loes Stegehuis werd geboren op 31 oktober 1987 te Best. Na het behalen van het vwo-diploma in 2005 aan het Heerbeeck college startte zij met de studie Technische Geneeskunde aan de Universiteit Twente. Haar 10-weekse masterstages deed zij bij het Medisch Centrum Leeuwarden op de afdeling neonatologie, het Antoni van Leeuwenhoekziekenhuis op de afdelingen chirurgie en nucleaire geneeskunde en het Jeroen Bosch Ziekenhuis op de afdeling radiologie. Met haar masterscriptie over diffuse reflectie spectroscopie bij borstkanker in het Antoni van Leeuwenhoekziekenhuis op de afdeling chirurgie, behaalde Paulien in 2012 haar masterdiploma ‘Technical Medicine’. In december 2012 begon ze met haar promotieonderzoek, in het Leids Universitair Medisch Centrum, op de afdelingen radiologie en heelkunde (promotor: Prof. Dr. Boudewijn P.F. Lelieveldt, co-promotoren: Jouke Dijstra en Alexander L. Vahrmeijer) waarvan de resultaten in dit proefschift zijn beschreven. In juni 2017 begon zij bij Gupta Strategists, een strategisch adviesbureau in de zorg, waar zij nu nog werkt.